Mathematical Problems From Cryobiology

A Dissertation

presented to

the Faculty of the Graduate School

University of Missouri

In Partial Fulfillment

of the Requirements for the Degree

Doctor of Philosophy

---

by

James Dale Benson

Professor Carmen Chicone and Professor John Critser, Dissertation Supervisors

DECEMBER 2009

The undersigned, appointed by the Dean of the Graduate School, have examined the dissertation entitled

Mathematical Problems from Cryobiology

presented by James Dale Benson,

a candidate for the degree of Doctor of Philosophy and hereby certify that in their opinion it is worthy of acceptance.

Professor Carmen Chicone

Professor John Critser

Professor Tanya Christiansen

Professor Yuri Latushkin

Professor Stephen Montgomery-Smith

To Jack and (.)

ACKNOWLEDGEMENTS

Writing this Ph. D. has given me an opportunity to learn about myself, about my friends and about my family. I've learned that there is a world of knowledge whose history spans centuries of careful thought and consideration, and that my own small contributions are only small a mark on the pages of academic pursuit. These last seven years my life have revolved around problems presented in this dissertation and elsewhere, and though I've been focused on one problem in general, the interactions with friends, family, and colleagues from all disciplines have inspired me to believe that there must be more to academics than a single discipline, more to a discipline than academy, and more to life than an academic pursuit, and for these reasons, I'm indebted and overwhelmingly grateful to the many people who made it possible:

To my parents, Dale and Barb, thank you for allowing me to follow my own path, explore the arts, humanities, and the sciences at my leisure (probably to your financial dismay). Your delicate balance of support and distance has been amazing, and now that I'm a father, I have become more proud to be your son. Thank you for being great role models, great friends, and great support. I love you both.

To my siblings Chris, Chuck, and Dave. Thank you, Chris for reminding me how important it is to have the vision in mind while trudging through the details and for reminding me that there's way more to life than science and scientists. Thank you, Chuck for continually inspiring me to love science, for teaching me how to be a scientist, for giving me my first real lab gig, and for challenging me at every step of the way. Thank you, Dave for exposing me to computers and programming, for philosophic conversations on everything, for a spectacular summer job, for continual

positive reinforcement, and for biannual visits that bookended my summers.

To my advisor John, thank you for giving me my first job, my first lab work, my first cryobiology conference, my first published paper, and for convincing me to come to Missouri to work in this truly fascinating and interdisciplinary field. Thank you for keeping me funded, keeping me published, and for introducing me to so many fantastic collaborators. Thank you for reminding me that there is a Philosophy of Science that all scientists should keep in touch with, and that I am earning a doctor of Philosophy.

To my advisor Carmen, thank you for tolerating a graduate student who has more applications than time and more breadth of knowledge than depth. Thank you for keeping me grounded, reminding me of what a mathematician does, and reminding me of why I wanted to become a mathematician. Your involvement in diverse projects has been an inspiration for my future research aspirations. Thank you for your interest in my research and my life beyond my research and for your limitless support and enthusiasm,

To my friends from the Mathematics and Veterinary Pathobiology departments: I am indebted for Tuesday night trivia and the "dirty deal," Thursday, Friday, and Saturday 7 hour "happy hours," banal conversations about hamsters in wet suits, golf, being the weakest player on an otherwise respectable (well, some years) basketball team, Scrabble, and pitchers of Boulevard Wheat at a row of tables 30 feet long at the Heidelburg. At Vet Path, thank you for making me the "math guy" who should know more about statistics, for daily lunch conversations, for letting me be the utility infielder on champion softball teams, for keeping me in touch with biology and the

life sciences, and for giving me a desk with too much room to pile papers on.

To my colleagues Yuksel Agca, Xu Han, Steve Mullen, Hongsheng Men, Gary Solbrekken, and Erik Woods, thank you for your patience, your love for science and for your inspiration. I am indebted to you for actually carrying out experiments, reminding a mathematician of the bounds of physics and biology, and giving me new problems to think about.

To my mentees Claire, Sarah, and Jason, thank you for reminding me why I wanted to go into academia in the first place. You guys were all great, and great sports. I learned as much if not more from you than you from me.

To Trina, Idelle, and DeShayda, thank you for being a second family for Jack. It has made life easier for me to know that Jack spends his days with people that truly care for and love him.

To my mother-in-law Anna, thank you for your support, for your willingness to spend weeks at a time making my and Corinna's lives easier. It would have been hard to make it through a few times without your love and support.

To my son, Jack, who has given me so much joy these last 30 months that I am inspired to be a better man, a deeper thinker, and a more considerate person. May your beautiful inquisitiveness and love for life never falter.

Finally, to my wife, Corinna, thank you for supporting me, inspiring me, prodding me, making me a better person, widening my thoughts and perspectives on a daily basis, bringing me down to reality, keeping me awake at nights, and making me laugh. I love you.

Table of Contents

List of Figures

List of Tables

Mathematical Problems from Cryobiology

James Dale Benson

Professor Carmen Chicone and Professor John Critser, Dissertation Supervisors

ABSTRACT

Cryobiology is the study of life and death at low temperatures and provides a fascinating setting for applied mathematics. The interdisciplinary nature of cryobiology mirrors the diversity of applications ranging from animal agriculture to laboratory cell and species preservation to critical human clinical applications for the preservation of life and for the killing of cells during cryosurgery. The work comprising this thesis develops approaches for optimization of cryobiological protocols, and defines a new model for common cryobiological procedures. The first step is to advance an understanding of the optimal control of a classical ODE system describing the mass transport that occurs during cryopreservation. This investigation leads to the description of exact solutions to this 70-year-old nonlinear system, a global stability result for the generalized system with n-solutes, controllability and existence of optimal controls in the n-solute case, and a complete synthesis of optimal controls in the 2-solute case. After defining optimal controls, the question arises whether the predicted continuous optimal control of the extracellular environment affects the hypotheses of the ODE model, namely, perfect stirring inside and outside of the cell/tissue-media boundary. We constructed a new model coupling the ODE mass transport at the cell/tissue boundary of changing radius with convection-diffusion and potential flow models and a numerical integration scheme to explore the effects of advection on the cell-media interface.

Chapter 1

Introduction

Although this is an ostensibly mathematics thesis, the application of mathematics in cryobiology is rooted in an understanding of the biology, chemistry, engineering, and physics of the process of freezing. Because of this I would like to spend the next few sections developing the basic fundamentals of cryobiology as a science so that the application of mathematics to this science in the following chapters will have a context.

1.1 History and Fundamentals of Cryobiology

[1] Before the discovery of cryoprotective agents and the successes that have been attributed to their discovery, cryobiology was an investigative science and cryobiologists were interested in the so called "death points" of cells—"the definite temperature at which an organism passes from the living to the dead state" [83]. These natural philosophers used cold as another means to test the boundaries between life and death and, as a model cell type, spermatozoa have been particularly useful subjects in this study, in large part due to their motility, which imports an easy way to determine

[1] Parts of this work appeared in a submitted review with co-authors Erik J. Woods, Eric M. Walters, and John K. Critser [15] and in a book chapter with co-authors Eric M. Walters, Erik J. Woods, and John K. Critser [125]

survival. References to investigations into sperm cryobiology date back to the 17th century [116], and there are reports of the well known 18th century Italian natural philosopher Lazzaro Spallanzani investigating the effects of cold on frog and human sperm [23]. According to Luyet and Gehenio [83] more experiments were conducted during the late 19th century, including cooling frog, turtle, rabbit, and dog sperm to between -4 and -7°C, with recovery of motility in the rabbit and dog. The 19th century brought the suggestions of human and non-human sperm banking by Mantegazza [116] who successfully cooled human sperm to -17°C, and who also recognized much of the utility in both agricultural and human sperm preservation. The first half of the 20th century produced similar work leading to moderate success and investigations into the duration [113] and temperature of storage [58], cooling and warming rates [117], and additives such as sucrose to aid in vitrification [81]. Shettles [117] noted the wide variability of survival among specimens or freezing temperatures without noting the effects of cooling rates. Parkes [101] compared survival after exposure to -20, -79, and -196°C in various sized freezing containers ranging from thin film loops to 1 mm diameter glass tubes and concluded (we now know incorrectly) that cooling rate was not an important factor.

Until 1949, research on the effects of low temperatures on spermatozoa was mostly empirical, involving a few (competing) hypotheses about the importance of ice avoidance. By the 1940s it was generally accepted that a rapid cooling, "vitrification" technique was the most promising approach [101]. In 1949, the chance discovery by Polge, Smith and Parkes [110] of glycerol, ethylene glycol and propylene glycol as permeating chemical protecting agents (CPAs) for freezing human and fowl spermatozoa

sparked a new era in research. The following decades of research remained mostly empirical, testing combinations of CPAs, cooling, and warming rates, but in 1956 Meryman investigated the mechanics of freezing from a physical chemistry perspective [89], and in 1963 Mazur [85] introduced the concept of using simple differential equations to describe the movement of water from cells as the surrounding media froze, and related this water loss to survivability at different cooling rates. This was followed by Mazur's landmark work with Liebo and Chu in 1972 [86] outlining the optimal "equilibrium" cooling rate that balanced the avoidance of damaging intracellular ice formation with the reduction of exposure to high concentrations of salts, shown to be deleterious by Lovelock [80] and Meryman [90].

The conclusions of these efforts and those of the next few decades were that there are at least two fundamentally different approaches to cryopreserving cells: one where cells are cooled rapidly in order to avoid all intracellular ice crystallization, typically called a vitrification approach, and one where cells are cooled slowly, allowing the cell to dehydrate at low temperatures to promote intracellular glass formation and avoid deleterious intracellular ice formation (IIF), typically called an equilibrium approach. Both approaches yielded success for various species, but until the 1980s and 1990s the osmotic damage due to the process of the addition and removal of CPAs was often overlooked [9, 8, 10, 107]. The following years produced work noting that all cells undergo volume fluctuations during the addition and removal of CPAs but that the limits to which cell volume can fluctuate without damage (called "osmotic tolerance limits" (OTL)) are cell and species specific, varying even within a given species (e.g. among strains) [8, 9, 10, 31, 34, 43, 50, 107]. This damage due to the addition and

removal of CPAs is especially relevant to sperm cryopreservation due to their narrow osmotic tolerance limits [48, 126]. Finally, several models describing the probability of ice formation were developed in the 1990s by Toner, Cravalho, Bischof and others [16, 59, 124] leading to a more detailed understanding of the mechanisms of cell death due to ice formation during equilibrium cooling protocols.

1.1.1 Fundamentals of Equilibrium Freezing

The discovery of cryoprotective agents yielded new insights into the physics of freezing living cells. Prior to this, successful cryopreservation protocols depended on suppressing extracellular ice formation and were aided by both the addition of chemical agents [81] and by cooling rapidly [83] to produce what was then called vitrification—the transition of a liquid to an ice crystal-free meta-stable glass. Luyet and others understood that intracellular water content was the source of potentially damaging ice formation, but Lovelock made the realization [79, 80] that permeating CPAs allow the reduction of water without deleterious intra and extracellular concentrations of salt ions, while enhancing the glass formation properties of the solution.

Specifically, the mechanism of protection by permeating CPAs is twofold. First, as freezing media is cooled below zero degrees C and ice is nucleated (e.g. a microscopic ice crystal has formed in the solution), pure water precipitates, or "freezes out," as ice, concentrating the remaining media and lowering its melting point. As temperatures are further decreased, this process continues along the liquidus curve of the solution defined by the phase diagram until the glass transition temperature or the eutectic is reached, at which point the solution either crystallizes or vitrifies. The freezing point depression of a solution is a multiple of its osmolality (1.86 °C/osm), and

because of this, if a less toxic reagent such as a CPA accounts for the majority of the osmolality at room temperature, as water precipitates as ice, the CPA to salt ratio will remain fixed. For example cells cooled in an initially isotonic NaCl-water solution to -10°C, by Raoult's law [95] will be exposed to a 5.6 Osm NaCl-water solution, which is approximately a 2.8 molal saline solution. On the other hand, if the initial ratio of CPA to NaCl was 8:1 (corresponding to an approximately 2.4 molal CPA in isotonic saline solution), the solution osmolality at -10°C will still be 5.6 Osm, but only 0.7 Osm will be from NaCl, (corresponding to an approximately 0.35 molal salt solution) and the other 4.9 Osm will be from the CPA (see Pegg and Diaper [106] for a more thorough treatment of this topic). The relationships between molality and melting point (alternatively, freezing point depression) are described by phase diagrams, and those with three components: salt, CPA and water, are known as ternary phase diagrams [29, 36, 65, 115]. The second protection mechanism is that the cryoprotective agents used most frequently (e.g. DMSO, glycerol, 1-2 propanediol (PG), and ethylene glycol (EG)) aid in the glass formation tendencies of solutions [135]. This increase in glass formation tendency corresponds to a decrease in the likelihood of ice nucleation, and a corresponding decrease in the likelihood of intracellular ice formation.

According to the generally accepted "two factor hypothesis" of Mazur [86], the likelihood of success at any particular freezing rate is dependent on two competing factors. The first factor is the interaction between cooling rate and intracellular ice formation. As mentioned above, the concentration of extracellular media increases as the temperature is decreased. If the cooling rate is slow, the osmotic imbalance

(the difference in the chemical potential of water inside and outside the cell) caused by this increase in solute concentration can be rectified by the exosmosis of water and the influx of CPA into the cell. This results in a net decrease in cell volume and an increase in the intracellular osmolality. In theory this process can be continued until the cell is sufficiently dehydrated that upon plunging into low temperature envirionment (e.g. a liquid nitrogen bath), the cytoplasm will vitrify, because the higher the concentration, the more likely a solution is to vitrify [19, 20, 21]. The other side of the two-factor hypothesis is that prolonged exposure to high concentrations of salts causes irreversible membrane damage, as described by Meryman [90]. Therefore, cooling at very slow rates allows cells enough time to maintain the chemical potential of water between the inter- and extra-cellular environments, concentrating solutes in their cytoplasm; but, alternatively exposes them to high salt concentrations for extended time periods. Therefore Mazur suggested that the optimal "equilibrium" cooling rate is that which is as fast as possible to avoid solution effects, but slow enough so that the cells can dehydrate sufficiently to avoid intracellular ice formation (Figure 1.1). These competing phenomena have a characteristic inverted "U" shaped temperature versus survival curve, and experiments have borne this out in a vast array of cell types (Figure 1.2). Mazur suggested that in order to reduce the likelihood of intracellular ice formation, the ambient temperature of the cells and media should be no more than 2°C colder than the melting point of the cytoplasm. This difference between melting point and ambient temperature is called supercooling, meaning that the solution is in an unstable state, at which if ice were to be nucleated, ice would grow throughout the media. In other words, Mazur suggests that cells be subjected

to no more than 2°C of supercooling.

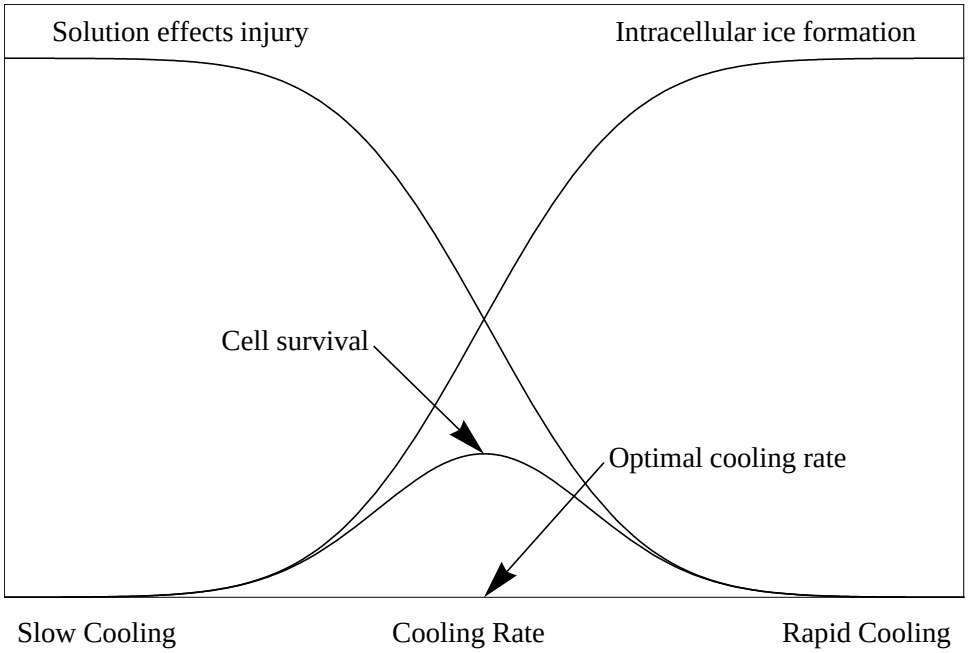

Figure 1.1: Plot of the interaction between cooling rate, "solution effects" injury, ice formation injury and cell survival. At low cooling rates "solution effects" are the dominant factor in cell damage, but as cooling rates increase and exposure time decreases these effects are minimized. On the other hand, at high cooling rates intracellular ice formation is the dominant factor in cell damage, and as cooling rates are decreased, the likelihood of intracellular ice formation decreases. The combination of these two effects imply that there will be an inverted "U" shaped survival curve and an optimal cooling rate that minimizes both the solution effects and intracellular ice formation. (Redrawn from [97]).

With these criteria in place, a model can be used to describe how water and solutes cross the cell membrane at any given temperature to predict the solute concentration inside the cell. If the concentration correlates to less than 2°C of supercooling, we can increase the cooling rate; if it is more, then we can decrease the cooling rate. Typically, cryobiologists have dealt with linear cooling rates, most likely because these are the easiest to repeat, calculate in a differential equation, and approximate with cooling apparatus, but the natural cooling rates of objects exposed to low temperatures are

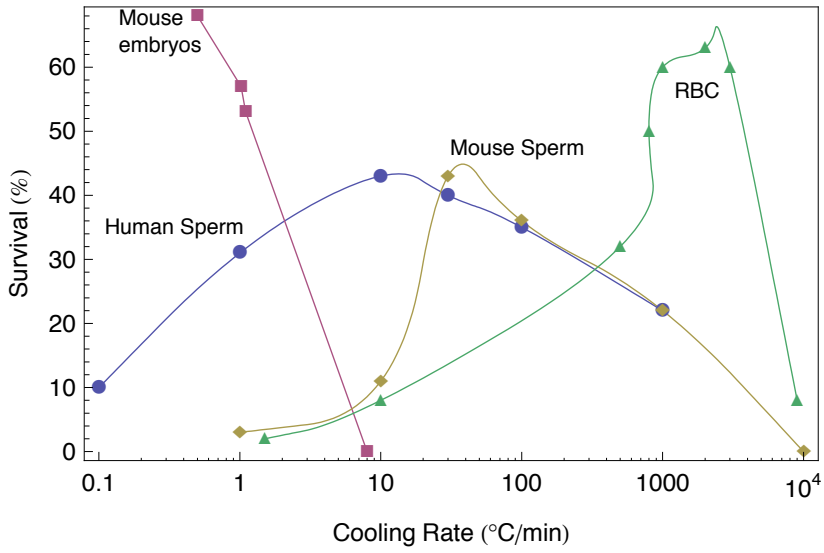

Figure 1.2: Survival rates for various cell types cooled at different rates. In most cases cell exhibit the classic "inverted U" shaped response, with relatively small ranges of rates yielding optimal survival (redrawn and modified from [87]).

exponential [82]. Although there have been several reports of success using non-linear cooling rates [96], there was no firm basis for the theory of optimizing non-linear cooling rates until very recently. In 2004, Woelders and Chaveiro [129] published a theoretical development of non-linear cooling rates developed by fixing the amount of supercooling at two degrees. This allowed them to calculate the cooling rates needed to achieve this fixed amount of supercooling. This, in theory, should be the fastest, "safe," slow cooling rate, but there are many caveats. For example, the permeability of the cell to water and solutes must be known at all subzero temperatures. This is not a trivial measurement; only recently was a method for subzero water permeability measurement published [33].

1.1.2 Rapid cooling approaches

Until now, I have mainly discussed the development of "slow" or "equilibrium" cooling protocols. Vitrification, on the other hand, has always been the goal of cryobiologists. Essentially, at high enough cooling rates ($>$ 1000 °C/min) the intra- and extracellular aqueous solution does not crystallize, and instead forms an amorphous glass, a process called vitrification. This vitrification of the solution is associated with little if any cell damage, it is the most appealing cryopreservation protocol because it is so fast (compare this with a standard 1-10°C/min protocol) and has the potential to require no expensive equipment (i.e. plunge the sample directly into liquid nitrogen). The downside to vitrification procedures is that although isotonic saline is theoretically vitrifiable, the cooling rates needed to achieve vitrification are on the order of 10^5 to 10^6 °C/min. Alternatively, much work has been done investigating the vitrification properties of many different solutions [38]. At higher concentrations, greater than four

or five molal, typical CPAs such as glycerol or propylene glycol become vitrifiable at cooling rates on the order of 10^3°C/min.

Unfortunately, as appealing as vitrification seems, there are several downsides. First, the cooling rates are difficult to achieve. In order to achieve ultra-rapid cooling rates, the surface area to volume ratio of the cell suspension (i.e. the container that holds the cells and their suspending solute) must be very high. This has been achieved using a "cryo-loop" [68]. The idea of the cryo-loop is to have a very thin film of solution that maximizes the surface exposed to liquid nitrogen. Alternatively, very thin straws also have a very high surface to volume ratio and have been used successfully to vitrify oocytes [112]. The second problem is achieving the high molar intracellular concentrations (4-5 molal) of permeating cryoprotectants. In the next section I discuss the details of this challenge, which is the primary focus of this dissertation.

1.1.3 CPA addition and removal

The beneficial effects of CPAs at subzero temperatures make them attractive for use in both equilibrium and rapid cooling approaches, but their high concentrations (typically greater than 1 molal) make them harmful to cells if added and removed carelessly. For example, suppose a cell has been equilibrated with 1 molal glycerol and prior to use, this glycerol must ultimately be removed. If the cell was abruptly returned to non-CPA containing media, a 1 molal solute concentration difference across the cell membrane would cause a rapid influx of water as the chemical potentials were equilibrated. Depending on the volume of this influx, the cell will swell, perhaps beyond its capacity causing lysis. An analog occurs during the addition of CPA, and

though the damaging action of minimal shrink volumes is unclear, the damage in sperm may be linked to membrane fusion. The extents to which a cell can shrink or swell without damage, called osmotic tolerance limits, have been described using many different endpoints in spermatozoa from a variety of species (Figure 1.3) [3, 17, 45, 93, 118, 120, 126, 128], and the actions of some chemicals to expand these limits have been tested on spermatozoa as well [4].

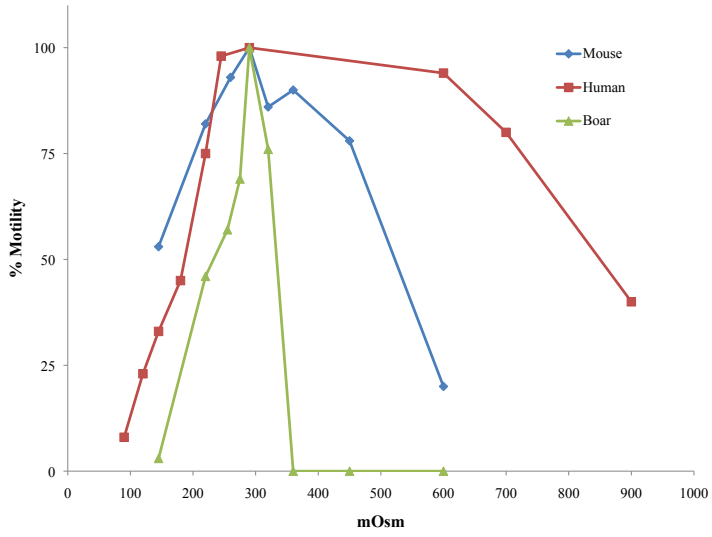

Figure 1.3: Osmotic Tolerance of Spermatozoa from Rat, Boar, and Mouse. Redrawn from Guthrie et al. (2002).

Damage due to these osmotic events can be avoided by adding CPA-containing media either stepwise (e.g. moving cells from 0.25 M to 0.5 M then to 1 M media) or dropwise (e.g. gradually dropping high concentration media into the cells while stirring to achieve a gradual addition protocol) [45, 107, 103, 104, 105]. Similar methods have been developed for CPA removal as well. Knowledge of these osmotic toler-

ance limits in conjunction with knowledge of membrane water and solute transport parameters has allowed the prediction of "more optimal" addition and removal protocols (Figure 1.4), which allow for reduction of exposure time to CPAs or osmotically induced volume flux [50, 72]. The remaining factor to consider is that high concentrations of these permeating CPAs have been shown to be cytotoxic; therefore specific testing of CPA toxicity can further aid the optimization of cryopreservation protocols [38, 42, 134].

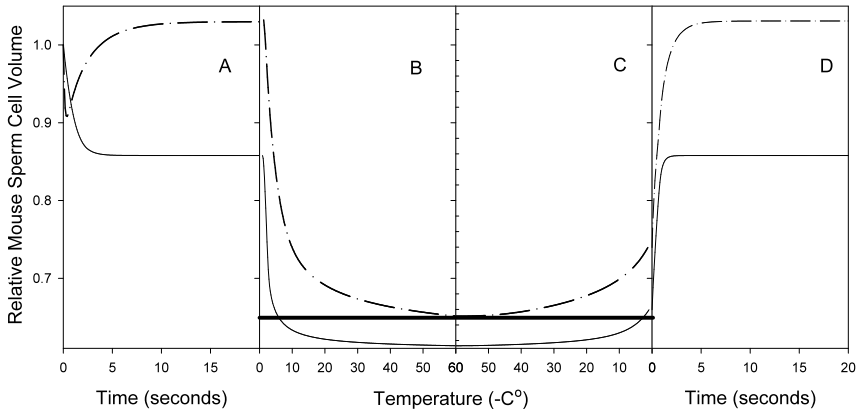

Figure 1.4: Mouse spermatozoa volume during cryopreservation. The four panels (A-D) represent: addition of CPA (A), cooling (B), warming to the melting point (C) and warming above 0°C (D). Two cases are shown for ICR mouse spermatozoa: use of a skim milk/sucrose medium (solid line) and a PBS medium containing 1 M glycerol (dot-dashed line). The solid line near the bottom of panel B and C represents the cell volume at which the sperm contain 10% of the initial intracellular water. If the cell volume remains above this line, intracellular ice formation is likely to occur. (Data from [109])

1.1.4 Archetypical experimental design for fundamental cryobiology

With all of this as background, I will conclude by outlining the typical fundamental cryobiological experiment in the following steps (examples of these experiments

can be found in [1, 24, 48, 50, 108, 77, 131]). First, cells are exposed to various anisosmotic salt solutions and their subsequent volume is measured. The reciprocal of solute concentration versus normalized cell volume is plotted. This is to establish that cell volume corresponds linearly with a change in osmotic pressure (i.e. they behave as linear or ideal osmometers, the Boyle-Van't Hoff relationship). The intercept of the regression (towards a theoretical infinite concentration) predicts the osmotically inactive fraction of the cell, which is the cell membrane, organelles, proteins, and bound water which will not cross the plasma membrane. This establishes the osmotically inactive portion of the cell (often referred to as V_b). In the case of mammalian sperm, for example, this value is usually between 60 and 70% of the isosmotic volume [48, 61, 51].

The next step is to establish the biophysical parameters of solute and water permeability, usually indicated as P_s and L_p, respectively, at several temperatures. A common tool for the determination of these parameters has been the use of the Coulter Counter [14], which records electric pulses proportional to cell volume. This allows the real-time measurement of thousands of cells exposed to various solutions. A second method is the use of a stopped flow apparatus which takes advantage of the relationship between average population volume and light refraction [75]. The advantage of the stopped flow apparatus is its temporal resolution. The disadvantage of the stopped flow apparatus is that the measurement of volume is indirect. Finally the method employed by Jacobs in the 1930s [57], and still in use [25], is the measurement of cell volume via light microscopy.

If the experiment were to stop here, I would have enough information to predict

both an optimal CPA addition and removal protocol and a probable optimal cooling rate. Alternatively, I can also establish the parameters of the intracellular ice formation model of Karlesson et al.,[59]. This is done by monitoring cells under a microscope while cooling and noting the percentage of cells that freeze intracellularly at a given temperature and degree of supercooling. After these parameters are established a theoretically optimized protocol can be developed that obeys the fundamental principles outlined in Mazur et al., [86]), the optimal freezing protocol cools the cell the fastest while avoiding a degree of supercooling associated with a high probability of ice formation.

1.1.5 Empirical versus mathematical approaches to cryobiological optimization

Although there is a large amount of work in establishing the values of cryobiological parameters, the work is significantly less than that which would be involved in developing a cryopreservation protocol entirely empirically, given the wide variation in cryopreservation protocols. Mathematical applications of fundamental cryobiology can give investigators a much narrower band of possibility for empirical experimentation, saving valuable time and resources.

As a brief exploration, suppose one approached cryobiology from a purely empirical perspective. Though the literature shows that optimal equilibrium cooling rates range over 5 orders of magnitude, let us be optimistic and suppose that a researcher would use comparable cell types to narrow down to one order of magnitude. I will suggest that there should be 5 steps tested within this order of magnitude. There are four typical CPAs used: DMSO, Glycerol, Ethylene Glycol, and Propylene Glycol.

Moreover there is a range of optimal CPA concentrations published in the literature from ≈ 0.5 M to ≈ 2 M. Let us choose 5 steps between 0.5 and 2 M. Optimal "plunge temperatures"—the temperature at which equilibrium cooling has effectively dehydrated the cells so that intracellular ice formation during the plunging directly into a liquid nitrogen bath is unlikely—range from -30°C to -80°C. Suppose we test at 10°C levels. Though there are other variables to check (for example CPA addition and removal protocols), let us stop here, but each treatment must be repeated to control for experimental error and cell population variability. Suppose we choose a typical experimental design and repeat each treatment on three days with three replicates per day. This experiment would require $5 \times 4 \times 6 \times 5 \times 3 \times 3 = 5400$ data points. But even with this many data points, the power to resolve specific differences between treatment groups would unlikely be enough. Moreover, the vast proportion of the results will simply be negative: the protocol was unsuccessful. This sort of experiment leaves the researcher with little to base a new hypothesis on.

We go into this detail only to justify the great deal of work and effort needed to define optimal cryopreservation protocols using mathematical modeling. Even if predicted responses do not match experimental results, hypotheses exist that can be tested, and valuable information is gained with each experiment.

1.2 This thesis and fundamental cryobiology

The aim of this thesis is to take a more mathematical approach to one aspect of the cryobiological problem, namely the CPA addition and removal process. I would argue that the biggest impact in mathematical optimization of cryobiology can be made in the addition and removal of CPA. If one could instantaneously add or remove a high

concentration of CPAs, the avoidance of ice formation would be practically guaranteed at most cooling rates. Of course this is not possible for the multitude of reasons listed above. On the other hand, significant improvements to cryobiological protocols can be achieved. In this thesis I first analyze the standard mass transfer equations alone (Chapter 2). Though the mathematical techniques presented in this chapter are not deep, they provide a setting and a preview of the remainder of this thesis. The critical technique used in all chapters is the use of appropriate transformations that allow the reframing of the model in a much simpler setting. This turns out to be a very powerful technique in applied mathematics. For example, the classic mass transport model is a nonlinear coupled ODE system, but, with the appropriate choice of rescaling, we can transform the system to a linear ODE system solvable with classical techniques.

In the next chapters this transform is generalized and is utilized in the context of optimal control theory. In Chapter 3, we show that the generalized cellular mass transfer system, extended to n solutes, is globally asymptotically stable, significantly extending a result in recent literature [55]. This global stability result has direct implications in the controllability of the system (i.e. the ability to control a parameter of the system so that the flow goes from an initial point in the state space to a final point), which we prove. Because the system is controllable, and by the transformation behaves identically to a linear system, there is in fact an optimal control. Finally, I synthesize an optimal control in the case $n = 2$ and prove its optimality using a classic theorem of Boltayanskii.

Next, in Chapter 4 I apply this optimization theory in the more realistic and cryobiologically relevant case where there are cell volume constraints. The theoretical

time improvements of the optimized protocols, though dependent on parameters, range from five to fourty-fold over a standard protocol. These theoretically optimized protocols are then applied to a clinically important cell type–human oocytes.

Finally, to implement the optimal control, continuous perfusion around cells must be achieved. This requirement raises questions about the validity of assumptions in the standard mass transport model used above. In Chapter 5 I thus investigate a more complete model incorporating several phenomena that might have an impact on the mass transport, namely convection due to the fluid velocity field around cells, and diffusion due to concentration gradients generated both by the convection and by the changing environments. I couple this convection-diffusion equation with the mass transport equations in the form of Robin boundary conditions at the cell membrane. Finally I allow the cell boundary to change radius as a function of the predicted cell volume changes. I have begun the approach of this problem numerically, creating a numerical integration scheme. Again using a transformation, I was able to analyze the equations in a much simpler setting, allowing an exact solution of the fluid velocity vector field, reducing the system's complexity and allowing numerics to be performed in a much simpler domain. The numerics confirmed the "rule-of-thumb" type predictions at the single-cell-size level, namely that at single cell levels, diffusion is the dominant term and essentially there is no concentration gradient. However, at larger cell radii and into small tissue sizes, there are significant effects of the advection and diffusion terms on predicted cell and tissue responses.

Chapter 2

Exact solutions of a two parameter flux model and cryobiological applications

2.1 Introduction

[1]Mass transport models are used extensively throughout the biological sciences with applications ranging from plant biology and cryobiology to circulatory and kidney physiology [69, 103, 122, 127]. The two parameter solute and solvent model developed by Jacobs [57], and the related Kedem and Katchalsky [64] model have been used for a half-century or more to model transmembrane flux in biological systems. A discussion of the similarities and differences in the two formalisms can be found in the excellent review by Kleinhans [66].

In particular, the Jacobs model has provided a simple and accurate description of solute and solvent flux using a system of ordinary differential equations[2]:

$$\begin{aligned} \dot{V}_w &= -L_p ART\big(M_s^e + M_n^e - \delta_1 \tfrac{n_s^i}{V_w} - \delta_2 \tfrac{n_n^i}{V_w}\big), \\ \dot{n}_s^i &= P_s A\left(M_s^e - \delta_1 \tfrac{n_s^i}{V_w}\right), \end{aligned} \tag{2.1}$$

where V_w and n_s^i denote the intracellular water volume and moles of an intracellular

[1]Part of this chapter was published with co-authors John Critser and Carmen Chicone [13]

[2]Note that we use the mathematical convention $\dot{x} = \frac{dx}{dt}$, and the convention for the dilute approximation of osmolality $\Pi^e := M_s^e + M_n^e$ and $\Pi^i := (\delta_1 n_s^i - \delta_2 n_n^i)/V_w$. See Appendix A-1 for more details

permeating solute, respectively, and the other parameters are defined in Table 2.1. We note that the extracellular solute concentrations are given in terms of osmolality, and the intracellular solute concentrations are given as molality times a constant temperature dependent conversion factor, δ_1 and δ_2, to yield osmolality.

Until very recently, the use of this system was almost exclusively limited to numerical simulations—algorithms that approximate the solution of the differential equations [66]. Because of this, standard calculus techniques could not be applied to find the maximum or minimum of water and cellular volume or the times at which they occur. Additionally, algorithms for finding cell plasma membrane permeability coefficients had to either be inaccurate or very complicated and difficult to implement [119]. Furthermore, large scale calculations where hundreds of thousands of volume calculations (as with finite element models of tissue transport) are needed become exponentially computationally inefficient as the scale or accuracy is increased [78].

Recently a method for obtaining the volume maxima or minima using (2.1) was developed using a technique that defines an implicit relation between volume and concentration [63, 136]. However the method presented in these papers loses critical time information and thus cannot be used to accurately predict when these cell volume maxima and/or minima occur. This time information is a key parameter used in the development of protocols for addition or removal of high concentrations of cryoprotective agents such as glycerol or dimethyl sulfoxide (Me_2SO) [132], in the prediction of macromolecular uptake by arteries [122], and in kidney transport [69].

These current problems are ameliorated with the existence of an exact solution of (2.1); one that expresses the water volume, V_w, and the moles of solute n_s^i, as

Table 2.1: Definitions of major symbols and their test values

Symbol	Test Value	Units	Description
i, e			Superscripts (i, intracellular; e, extracellular)
n, s			Subscripts (n, non-permeating; s, permeating)
V_b	0.4	unitless	Osmotically inactive fraction
V_{iso}	1000	μm^3	Isosmotic cell volume
V_w		μm^3	Intracellular Water Volume
n_s^i		fmol	Femtomoles intracellular permeating solute
n_n^i		fmol	Femtomoles intracellular non-permeating solute
δ_1	1	osmol L mol^{-1} kg^{-1}	Osmolality conversion factor for permeating solute
δ_2	1.95	osmol L mol^{-1} kg^{-1}	Osmolality conversion factor for non-permeating solute
L_p	0.1	μm min^{-1} atm^{-1}	Hydraulic Conductivity
P_s	10	μm min^{-1}	Solute permeability coefficient
A	483.6	μm^2	Cellular surface area (assumed fixed)
R	0.08206	L atm K^{-1} mol^{-1}	Gas constant
T	295.16	Kelvin	Temperature
t		min	Time
$\overline{V}$	.0730151	L mol^{-1}	Partial molar volume of typical CPA
M_s^e	1.0	osm kg^{-1}	Extracellular permeating solute osmolality
M_n^e	0.3	osm kg^{-1}	Extracellular non-permeating solute osmolality
M_s^i	0	osm kg^{-1}	Initial intracellular permeating solute osmolality
M_n^i	0.3	osm kg^{-1}	Initial intracellular non-permeating solute osmolality

functions of time and initial conditions. That is, given a set of initial conditions such as cell volume and surface area, intra- and extracellular concentration, etc., we would like to have a formula for water volume and moles of solute as a function of time. In this work, we present a method whereby the exact solution of (2.1) (and thus the exact volume and intracellular solute concentration) can be determined for all experimental time. We then apply this exact solution technique to classic cryobiological problems involving solute and solvent transport such as finding cell volume, cell water volume, and intracellular solute concentration maxima and minima, determining cell membrane permeability parameters, and improving large scale tissue transport models.

2.2 Methodology

2.2.1 A reparameterized solution to the Jacobs model

For most non-linear differential systems, it is impossible to express their solutions explicitly as a function of time and initial conditions [22]. The Jacobs model is a unique case. To our knowledge, it cannot be solved as a function of the temporal variable using traditional methods such as separation of variables or integration factors. This is likely the reason why no exact solution has emerged since its inception. Our analysis is based on a result from the theory of ordinary differential equations (ODEs): the qualitative behavior of a system of ordinary differential equations (e.g. its phase portrait, orbit structure, maxima and minima, etc.) is the same with rescaled time. In the same way that a logarithmic curve can be turned into a straight line using a logarithmic scale on one axis, we can stretch and squeeze the solution of a differential equation so that the solution appears to be linear.

For example, if a system can be written in the form

$$\dot{u}(t) = \lambda(u(t))F(u(t)), \tag{2.2}$$

where $\lambda : \mathbb{R}^n \to \mathbb{R}$ is a nonzero scalar valued function, the qualitative behavior is identical to that of the system

$$\dot{w}(\tau) = F(w(\tau)). \tag{2.3}$$

More precisely, if $u(t)$ is a solution of (2.2), then the function $q(\tau)$ given by

$$q(\tau) := \int_0^\tau \frac{1}{\lambda(u(s))} ds \tag{2.4}$$

is invertible and $w(\tau) := u(q(\tau))$. Similarly, if w is a solution of (2.3), then $u(t) := w(p(t))$ is a solution of (2.2), where $p := q^{-1}$. For a proof of this standard result, see Chicone [26].

It is convenient to rename constants as a, b, c, α, and β (see Table 2.2) so that (2.1) simplifies to

$$\begin{aligned} \dot{n}_s^i &= \beta + \alpha \tfrac{n_s^i}{V_w}, \\ \dot{V}_w &= b + a\tfrac{n_s^i}{V_w} + c\tfrac{1}{V_w}; \end{aligned}$$

or, equivalently,

$$\begin{aligned} \dot{n}_s^i &= \tfrac{1}{V_w}(\alpha n_s^i + \beta V_w), \\ \dot{V}_w &= \tfrac{1}{V_w}(a n_s^i + b V_w + c). \end{aligned} \tag{2.5}$$

Equation (2.5) is in the form of (2.2), where $\lambda(n_s^i(t), V_w(t)) = 1/V_w(t)$ and $F(u) = (\alpha n_s^i(t) + \beta V_w(t), a n_s^i(t) + b V_w(t) + c)$. Hence we can recover solutions of (2.5) from the system

$$\begin{aligned} \dot{n} &= \alpha n + \beta v, \\ \dot{v} &= a n + b v + c. \end{aligned} \tag{2.6}$$

Table 2.2: Definitions of constants and their test values

Constant	Test Value	Parameters
a	1171.32	$L_pART\delta_1$
b	-1522.72	$-L_pART\left(M_s^e+M_n^e\right)$
c	210837	$L_pART\delta_2 n_n^i$
n_n^i	180	$M_n^i(0)V_w(0)$
α	-4836	$-P_sA\delta_1$
β	4836	$P_sAM_s^e$
γ	-1.69935 $\times 10^6$	$-\delta_1 P_s L_p A^2 RTM_n^e$
ρ	-6358.72	$-\delta_1 P_s A + L_pART\left(M_s^e+M_n^e\right)$
$2r_1$	-12158.4	$\rho-\sqrt{\rho^2+4\gamma}$
$2r_2$	-559.072	$\rho+\sqrt{\rho^2+4\gamma}$
c_1	121.178	$(2bc\alpha - cr_2\alpha + \gamma(c+ax(0)+by(0)-r_2y(0)))/\gamma(r_1-r_2)$
c_2	-121.178	$-(2bc\alpha - cr_1\alpha + \gamma(c+ax(0)+by(0)-r_1y(0)))/\gamma(r_1-r_2)$
c_3	600	$\alpha c/\gamma$

The linear differential equation (2.6) can be solved explicitly using standard ODE techniques. In fact, the general solution is

$$n(\tau) = \frac{1}{a}\left(c_1\left(r_1-b\right)e^{r_1\tau} + c_2\left(r_2-b\right)e^{r_2\tau} + b\frac{c\alpha}{\gamma} - c\right), \tag{2.7}$$

$$v(\tau) = c_1e^{r_1\tau} + c_2e^{r_2\tau} + \frac{c\alpha}{\gamma}, \tag{2.8}$$

where $r_1 := 1/2\left(\rho-\sqrt{\rho^2+4\gamma}\right)$, $r_2 := 1/2\left(\rho+\sqrt{\rho^2+4\gamma}\right)$, $\rho := (\alpha+b)$, $\gamma := (a\beta-\alpha b)$, and c_1 and c_2 are arbitrary constants. If we specify $n_s^i(0)$ and $V_w(0)$, we have

$$c_1 = \frac{2bc\alpha - cr_2\alpha + \gamma(c+an_s^i(0)+bV_w(0)-r_2V_w(0))}{\gamma(r_1-r_2)},$$
$$c_2 = -\frac{2bc\alpha - cr_1\alpha + \gamma(c+an_s^i(0)+bV_w(0)-r_1V_w(0))}{\gamma(r_1-r_2)}.$$

Thus, the equation for total cell volume can be written as

$$\begin{aligned} V_{total}(\tau) &= V_w + n_s^i\overline{V} + V_bV_{iso} \\ &= c_1\left(\frac{\overline{V}}{a}(r_1-b)+1\right)e^{r_1\tau} + c_2\left(\frac{\overline{V}}{a}(r_2-b)+1\right)e^{r_2\tau} \\ &\quad + (\frac{\overline{V}}{a}b-1)\frac{c\alpha}{\gamma} - \frac{\overline{V}}{a}c + V_bV_{iso}. \end{aligned} \tag{2.9}$$

We can glean some information about the exponents r_1 and r_2. For example, since our linear system (2.6) always has an asymptotically stable rest point in physiologic conditions (see Chapter 3), we will assume that r_1 and r_2 are both negative (see Chicone [26]). We also note that

$$\frac{c\alpha}{\gamma} = \frac{M_n^i(0)}{M_n^e} V_w(0). \tag{2.10}$$

This is in agreement with the negative sign of r_1 and r_2, since, as time progresses, the first two terms of (2.8) go to zero, leaving $c\alpha/\gamma$ equal to the ratio of initial intracellular and extracellular concentrations. Hence,

$$\lim_{t\to\infty} v(0) - v(t) = c_1 + c_2. \tag{2.11}$$

Note that if the non-permeating solute concentration is constant—a common situation in cryobiology, then $\lim_{\tau\to\infty} v(\tau) = v(0)$ implies $c_1 = -c_2$.

Similarly, the exponential terms of the solution $n(\tau)$ go to zero with time. Hence, we have that

$$\lim_{\tau\to\infty} n(0) - n(\tau) = \frac{1}{a}(c_1(r_1 - b) + c_2(r_2 - b)). \tag{2.12}$$

For (2.5), we have $\lambda(n, v) = -1/v$, thus, using (2.4), if $q(0) = 0$, then we have

$$\begin{aligned} q(t) &= \int_0^t \left(c_1 e^{r_1 s} + c_2 e^{r_2 s} + \frac{\alpha c}{\gamma} \right) ds \\ &= \frac{c_1 \left(e^{r_1 t} - 1\right)}{r_1} + \frac{c_2 \left(e^{r_2 t} - 1\right)}{r_2} + \frac{\alpha c}{\gamma} t. \end{aligned} \tag{2.13}$$

See Fig. 2.1 for a plot of $q(t)$ for typical values of L_p and P_s, where v and n are defined in (2.7) and (2.8). Thus, the desired exact solution of (2.5) is given by

$$\begin{aligned} V_w(t) &= v(q^{-1}(t)), \\ n_s^i(t) &= n(q^{-1}(t)). \end{aligned} \tag{2.14}$$

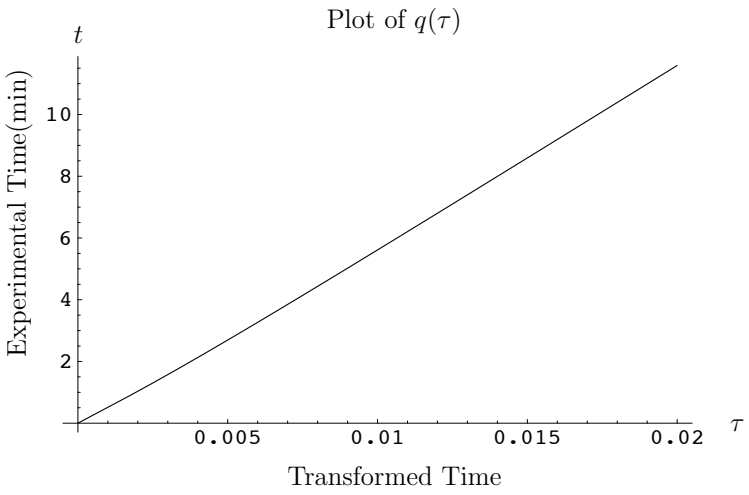

Figure 2.1: Plot of $q(\tau)$ using the test values from Table 2.2. Note that the high degree of linearity allows for an efficient transformation from the original time space to the τ-space.

2.2.2 The inverse of q

So far we have an exact solution for the Jacobs model and the function that transforms reparametrized time back to real time. We are now interested in finding the function that transforms real time to the transformed time so that we can use the exact solution methods to analyze experimental data.

We know that the time transform function q is invertible (see Chicone [26]), and we have an explicit equation for $V_w(t)$ and $n_s^i(t)$ (2.14)). The next challenge lies in finding $q^{-1}(t)$. Define $p(t) := q^{-1}(t)$.

To find a *formula* for $p(t)$ in terms of $q(t)$ and its derivatives only, we can use the Lagrange-Burman reversion formula [53] to obtain the power series representation

$$p(t) = \sum_{n=1}^{\infty} \frac{t^n}{n!} \left[\frac{d^{n-1}}{dt^{n-1}} \left(\frac{t}{q(t)} \right)^n_{t=0} \right]. \tag{2.15}$$

In other words, in the Taylor series

$$p(t) = \sum_{n=1}^{\infty} p^{(n)}(0)\frac{t^n}{n!}, \tag{2.16}$$

the derivatives are given by

$$p^{(n)}(0) = \frac{d^{n-1}}{dt^{n-1}}\left(\frac{t}{q(t)}\right)^n_{t=0}.$$

To illustrate this result we list the first four derivatives:

$$\begin{aligned}
p'(0) &= q'(0)^{-1}, \\
p''(0) &= -q''(0)p'(0)^3, \\
p'''(0) &= -q'''(0)p'(0)^4 - 3q''(0)p'(0)^3p''(0), \\
p^{(4)}(0) &= -q^{(4)}(0)p'(0)^5 - 7q'''(0)p'(t)^4p''(0) \\
&\qquad - 6q''(0)p'(0)^3p''(0)^2 - 3q''(0)p'(0)^4p'''(0).
\end{aligned}$$

In practice, it is easier to determine the Taylor coefficients by a recursion formula derived from the chain rule. Since $p(q(t)) = t$, taking the derivative gives $p'(q(t))q'(t) = 1$. Dividing by $q'(t)$ gives $p'(q(t)) = 1/q'(t)$. But since $q(0) = p(0) = 0$, we have that $p'(0) = 1/q'(0)$. The recursive formula

$$p^{(n)}(q(t)) = \frac{\left[p^{(n-1)}(q(t))\right]'}{q'(t)} \tag{2.17}$$

gives $p^{(n)}(t)$ for $n \geq 2$. Evaluating at $t = 0$, we see that the derivatives of $q(t)$ at zero are $q^{(m)}(0) = r_1^m c_1 + r_2^m c_2$ for $m > 1$. Thus, this calculation is straightforward, and can be done using an algebraic processor such as Mathematica® (Wolfram Research, Champaign, IL). In this case, the inverse of q is given by the Taylor series of Eq. (2.16) where $p^{(1)}(0) = q'(0)^{-1}$ and $p^{(n)}(0)$, for $n \geq 2$, is given recursively by (2.17). While the

power series representation of $p(t)$ has a nonzero radius of convergence, the difficult problem of determining this radius is beyond the scope of this work.

From a more practical standpoint, $p(t)$ can be evaluated very efficiently using numerical methods. Given t, we simply approximate the root τ of the function $q(\tau) = t$ numerically. Efficiency gains can be made by noting the high degree of linearity of the $q(\tau)$ function—especially as time increases—and using this information to optimize the algorithm. For example, with one line of code in Mathematica®, we can calculate the inverse of q for all data points.

2.3 Results and Discussion

2.3.1 Finding cell volume and intracellular solute concentration maxima and minima

The extrema of cell volume excursion, cell water volume, and intracellular solute concentration are of great interest in a number of fields. For example, cells may lyse if their volume exceeds physiological limits, and irreparable damage may occur if the cells shrink below physiological limits [56, 91]. This is especially relevant in the field of cryobiology, where cryoprotective agents such as glycerol cause the cell to shrink upon addition and swell upon removal.

Using $q(\tau)$ and its inverse $p(t)$ we have an invertible map between the original time space and our new time-transformed space (τ-space) (see Fig. 2.2). Because we have an exact solution, we can use standard calculus techniques to derive information from our equations. For example, a common use for the exact solution—the one addressed in [63, 136]—is the determination of the maxima and minima of cell volume excursion and/or chemical concentration. The advantage of our approach is that we can also

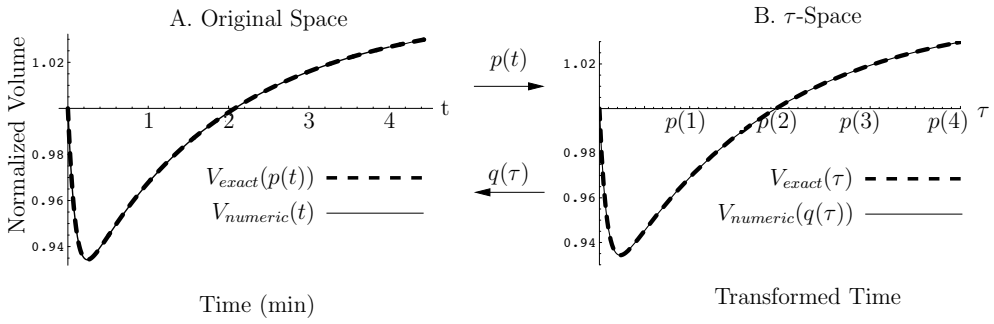

Figure 2.2: Diagram of time transform applications. To use the exact solution we apply a time transform, $p(t)$, to take data from the physical space on the left (panel A) to the new space (τ-space) on the right (panel B). Note that the volume excursions remain unchanged, and all analysis of the transformed system will apply to the original system. To return to the original time, we use the inverse transform $q(\tau)$. In this figure we show plots of both numerically integrated and exact solutions using the appropriate transform function, e.g. the plot on the left shows an overlay of $V_{\text{numeric}}(t)$ and $V_{\text{exact}}(p(t))$, and the plot on the right shows an overlay of $V_{\text{numeric}}(q(\tau))$ and $V_{\text{exact}}(\tau)$.

determine the time at which the maxima and minima of total cell volume, cell water volume, and moles of intracellular solute occur.

This can be done by setting the derivative of the solutions in τ-space equal to zero. For example, maxima and minima of the water volume are given by the solution of

$$v'(\tau) = c_1 r_1 e^{r_1 \tau} + c_2 r_2 e^{r_2 \tau} = 0. \tag{2.18}$$

To determine τ, we multiply both sides of (2.18) by $e^{-r_1 \tau}$ and rearrange the resulting equation to get

$$e^{(r_2 - r_1)\tau} = -\frac{c_1 r_1}{c_2 r_2}. \tag{2.19}$$

Because we have assumed that r_1 and r_2 are both negative, we know that $c_1 c_2 < 0$. Therefore, the term on the right-hand side of (2.19) is positive and we can take the

logarithm of both sides to obtain the solution

$$\tau_{\text{water}} = \frac{1}{r_2 - r_1} \ln\left(-\frac{c_1 r_1}{c_2 r_2}\right). \tag{2.20}$$

Thus, we have established an explicit solution for the time (τ_{water}) when the maximum or minimum of intracellular water volume occurs. The corresponding physical time is simply $t = q(\tau_{\text{water}})$, given by (2.13).

We can repeat this technique for total cell volume using (2.9), or for intracellular permeating solute content using (2.7) yielding the equations

$$\tau_{\text{total}} = \frac{1}{r_2 - r_1} \ln\left(-\frac{c_1 r_1 \left(r_1 - b + a/\overline{V}\right)}{c_2 r_2 \left(r_2 - b + a/\overline{V}\right)}\right), \tag{2.21}$$

$$\tau_{\text{solute}} = \frac{1}{r_2 - r_1} \ln\left(-\frac{c_1 r_1 (r_1 - b)}{c_2 r_2 (r_2 - b)}\right), \tag{2.22}$$

where τ_{total} and τ_{solute} are the τ-space times for the maximum or minimum of the total cell volume and the number of moles of intracellular permeating solute, respectively. These formulas are valid only if the argument of the logarithm is positive, which is the case for our test values. Again, we can calculate the original time using the q transform function. To illustrate the use of the exact solution in practice we choose typical values for our parameters (as in Table 2.1) and use (2.9) to get

$$V_{total}(\tau) = 86.76e^{-6079.18\tau} - 130.569e^{-279.536\tau} + 1043.81. \tag{2.23}$$

A plot of cell volume versus time for both a numerically integrated solution and the new, exact, solution with both time transport functions can be seen in Fig. 2.2. In fact, one of the immediate advantages of this exact solution technique is that a plot can be made quickly and easily—even with a graphing calculator—to see the dynamics of the curve without the necessity of complex software. Additionally, a calculator can

easily be programmed to give the cell volume maxima and minima and the times at which they occur—a significant advantage at the bench top.

A numerical calculation of the minima of both of these plots yields the minima found by calculating τ from(2.20): a minimal volume of 934.29 μm^3. Using the exact solution, we find that this volume occurs at $\tau = 0.000531$. We now use our $q(\tau)$ equation (2.13)) to convert back to real time. In this case, $q(0.000531) = 0.277935$ minutes, which agrees with the time obtained from the numerically integrated solution.

2.3.2 Curve fitting

The accuracy of the Jacobs model is dependent upon the accuracy of the parameters in the model. The hydraulic conductivity L_p and solute permeability P_s coefficients control the rate at which water and solute enter the cell. To determine these coefficients, cell volume is typically measured as a function of time while cells are exposed to media containing a permeating solute. The resulting volume versus time data are then fit using the model while varying the parameters L_p and P_s. Because the model has until now only yielded a numerical solution, developing a curve fitting algorithm has been quite difficult. Early investigators were able to fit data only by making simplifying assumptions [119]. In recent years, as computer software and processing power has improved, this range has been extended, but curve fitting has been relegated to complicated software such as MLAB® (Civilized Software, Inc., Bethesda, MD), Mathematica®, or other specialty software, and there is still a trade off between accuracy and speed.

A new curve fitting algorithm that does not involve numerical integration can be

implemented by transforming data to the linearized space using the time transformation $p(t, L_p, P_s)$, which depends on the time and the permeability parameters L_p and P_s. We wish to minimize the sum of squares estimate:

$$SS(L_p, P_s) = \sum_{i=1}^{n} (V_{\text{total}}(t_i, L_p, P_s) - V_i)^2. \tag{2.24}$$

Since $p(t_i, L_p, P_s) = \tau_i$ and $V_{\text{total}}(t_i)) = v_{\text{total}}(\tau_i)$, (2.24) can be written in the transformed time as

$$\begin{aligned} SS(L_p, P_s) &= \sum_{i=1}^{n} (v_{\text{total}}(p(t_i, L_p, P_s), L_p, P_s) - V_i)^2 \\ &= \sum_{i=1}^{n} (v_{\text{total}}(\tau_i, L_p, P_s) - V_i)^2. \end{aligned}$$

The minimization of this estimate can be made using the exact solution with common software packages such as SAS® (SAS Institute, Inc., Cary, NC) or Excel® (Microsoft Corporation, Redmond, WA). An advantage of this methodology is that it will give the most precise estimates of the sum of the squared error because there is no inherent error caused by numerical integration. In many cases, this technique is also faster. On the other hand the time transform must be applied for each data point in the (L_p, P_s)-parameter space. Using the numerical inverse techniques described above, however, this transformation takes a negligible amount of time.

For example, suppose our experimental data consist of ten points over a period of ten minutes. In order to analyze this with the exact solution we only need to calculate the transform function $p(t)$ ten times to yield data analyzable with our exact solution in the linearized space, and only make ten (exact) comparisons. On the other hand, even though there are only ten points, in order to accurately calculate the volume using the numerical solution of the differential equation we must discretize our ten minute experimental time interval into a mesh fine enough to provide accurate estimates. A reasonable time-step for this system (to retain accuracy) is approximately

one second. Thus, we must perform approximately 600 calculations to obtain the volume, together with ten (non-exact) comparisons to yield our sum of squares. With many data points, this computational advantage of speed is weakened due to the increasing number of time transform calculations necessary, but the accuracy advantage will remain.

2.3.3 Finite element models

When modeling mass transport in organs and tissues, necessary for simulating the effects of freezing during cryosurgery, a common simulation tool is finite element analysis. This processor intensive technique models solute and solvent flux through a tissue by defining a mesh of points and generating a concentration field corresponding to these points. This field is then used to estimate transmembrane flux for cells in a region around each mesh point. Increased numbers of mesh points improve accuracy but slow computations considerably. A solute solvent flux model must be used for each group of cells surrounding the mesh points. The result of these solute solvent equations generates a new field and the state of the tissue or organ is updated as time is incremented. Current techniques use from a few hundred to hundreds of thousands of mesh points with processing time increasing significantly as the number of mesh points increases. Thus the significance of a slight improvement in the efficiency of this modeling system is amplified with the complexity of the computation. We note here that these finite element computations can be performed in the τ-space exactly and efficiently, yielding significant improvements in both computational speed and accuracy in cell volume versus time simulations.

A numerical experiment was performed in which 100,000 calculations of volume

($V_{\text{total}}(.1)$) were made for both the numeric and the exact solution of the Jacobs system (2.1). A 1.2 GHz Intel Pentium 3 laptop carried out the numerical calculation in 7.771 seconds and the exact calculation more than three times faster at a time of 2.073 seconds. Thus for very large finite element grids where multiple time points are needed, the exact solution may be a significant improvement in efficiency. For example, to describe the volume flux of a relatively small tissue model containing 5000 cells (such as an islet of Langerhans) over the course of 25 minutes (the time to load islets of Langerhans with 1.5 M Me_2SO [133]) one needs at least 1500 time-steps. Thus 1500 time-steps at 5000 volume calculations each yields a total of 7.5 $\times 10^6$ calculations. On the above laptop, this calculation would take approximately ten minutes. On the other hand, using the exact solution techniques, the same calculation could be carried out with no error in 2.6 minutes. This sort of large-scale solution can be implemented to predict behavior of much more complicated systems.

2.4 Conclusions

We have presented an exact solution to a system of differential equations that has been in continuous use in biology for more than 70 years to model solute and solvent transmembrane flux in single cells, multicellular systems and tissues. Our method has distinct advantages over traditional numerical integration techniques in both calculation time and numerical accuracy, which allow for expanded applications in optimizing CPA addition and removal and in modeling solute and solvent flux in large multicellular systems. Finally, we have presented simple formulas for the calculation of the extrema of cellular water volume, intracellular solute concentration, total cell volume and the times at which they occur without requiring numerical integration.

Chapter 3

A general model for the dynamics of cell volume, global stability, and optimal control

3.1 Introduction

Recently, a general model of cell volume regulation was introduced that accounts for active and passive transport of water and a solute across the cell membrane [55, 54]. This model is

$$\begin{aligned} x' &= \alpha - \beta x/y, \\ y' &= -\gamma + \sigma x/y + \epsilon/y, \end{aligned} \tag{3.1}$$

where y is a (positive) non-dimensional water volume variable, x is a non-negative non-dimensional solute mass variable, α and γ are extracellular concentration variables, and β, σ and ϵ are cell dependent rate parameters. As discussed by Hernandez [55], this model is a general form for many existing in the literature, but is used, in particular in cryobiology (e.g. in Chapter 2 and [62, 63, 66]). It is simple to extend this model to multiple solute species by defining $w_1 = y$ to be the positive non-dimensional water volume of the cell, and w_i, $i = 2, \ldots, n$ to be the $n-1$ non-negative solute species, and x_{np} to be the non-negative non-permeating solute species analogous to ϵ [62]. In this case, we define $M_i(t) \geq 0$, $i = 2, \ldots, n$, to be

extracellular concentration variables analogous to α from system (3.1), and let the sum of the extracellular concentrations $\sum_{i=1}^{n} M_i$ be the analog of γ from system (3.1), where $M_1 > 0$ is the concentration of nonpermeating solute. Finally, define $b_i > 0$, $i = 2, \ldots, n$, to be the rate constants analogous to β and σ. We then have the general multispecies model,

$$\begin{aligned}
\dot{w}_1 &= \frac{x_{\mathrm{np}}}{w_1} + \sum_{j=2}^{k} \frac{x_j}{w_1} - \sum_{i=1}^{n} M_i, \\
\dot{w}_2 &= b_2 \left(M_2(t) - \frac{w_2}{x_1} \right), \\
&\vdots \\
\dot{w}_n &= b_n \left(M_n(t) - \frac{w_n}{x_1} \right),
\end{aligned} \tag{3.2}$$

defined in the positive orthant.

Applications of our multispecies model can be applied to cryobiology in particular [62] but since there are a large number of intracellular and extracellular chemical species that permeate across the cell boundary, it is natural to assume that if cells are placed in any non-physiologic environment, there will be transmembrane transport of water and more than one solute.

We will investigate the dynamics of these physiologically relevant models. Hernandez [55] showed that model (3.1) is locally stable at its rest point provided the rest point resides in the physically relevant region ($x > 0$ and $y > 0$). One would expect that this stability is in fact global asymptotic stability, and that a similar result is true for the model (3.2). We are able to prove both results.

Additionally, it is often desirable to determine optimal protocols for the control of intracellular concentrations of permeating reagents in cells governed by model (3.1) or (3.2). Examples can range from pharmicokinetics [70] to cryobiology [73]. We give

the conditions for a controllability result, show existence of an optimal control, and synthesize an optimal control in the case of one permeating and one non-permeating solute.

As in Chapter 2 our analysis hinges on the observation that we can factor out $1/w_1$ from the right-hand side of nonlinear system (3.2). We then again have a system of the form $\dot{w}(t) = \lambda(w(t))f(w(t))$, where $\lambda : \mathbb{R}^n \to \mathbb{R}$ is a positive scalar valued function. The qualitative behavior of the corresponding system

$$\dot{x}(\tau) = f(x(\tau))$$

is the same [26], and the invertible transformation

$$t = q(\tau) = \int_0^\tau \frac{1}{\lambda(w(s))} ds = \int_0^\tau w_1(s)\, ds \tag{3.3}$$

gives $w(\tau) := x(q(\tau))$. Thus, redefining $\dot{x} = \frac{dx}{d\tau}$, we will work with the linear system

$$\begin{aligned}
\dot{x}_1 &= x_{\text{np}} + \sum_{j=2}^{n} x_j - \sum_{i=1}^{n} M_i x_1, \\
\dot{x}_2 &= b_2 \left(M_2(t)x_1 - x_2\right), \\
&\vdots \\
\dot{x}_n &= b_n \left(M_n(t)x_1 - x_n\right).
\end{aligned}$$

or, in vector form,

$$\dot{x} = f(x, M) := A(M)x + x_{np}e_1, \tag{3.4}$$

where $M := (M_1, M_2, \ldots, M_n)$ and $A(M)$ is the matrix

$$A(M) = \begin{pmatrix}
-\sum_{i=1}^{n} M_i & 1 & 1 & \ldots & 1 \\
b_2 M_2(t) & -b_2 & 0 & \ldots & 0 \\
b_3 M_3(t) & 0 & -b_3 & \ldots & 0 \\
\vdots & \vdots & \vdots & \ddots & \vdots \\
b_n M_n(t) & 0 & 0 & \ldots & -b_n
\end{pmatrix}.$$

and e_1 is the first unit-basis vector. Note that system (3.4) is bilinear in x and M in the sense of Mohler [94]: $\dot{x} = (A + \sum_{k=1}^{m} u_k B_k)x + Cu$ where A, B_k and C are constant matrices, and u_k are scalar controls. In system (3.4), $f(\alpha(x_1 + x_2), y) = \alpha f(x_1, y) + \alpha f(x_2, y)$ and $f(x, \alpha(y_1 + y_2)) = \alpha f(x, y_1) + \alpha f(x, y_2)$. We take advantage of this fact by defining matrices

$$B_1 = \begin{pmatrix} 1 & 1 & 1 & 1 \\ 0 & b_2 & 0 & 0 \\ \vdots & 0 & \ddots & 0 \\ 0 & \dots & 0 & b_n \end{pmatrix}, \quad B_2 = \begin{pmatrix} 0 & 1 & 1 & 1 \\ 0 & -b_2 & 0 & 0 \\ \vdots & 0 & \ddots & 0 \\ 0 & \dots & 0 & -b_n \end{pmatrix}.$$

such that

$$\dot{x} = x_1 B_1 M + B_2 x + x_{np} e_1.$$

3.2 Dynamics for $M(t) \equiv M$

3.2.1 Stability

As mentioned in the introduction, the stability of our model in case $n = 2$ and function M_i is constant with $M_i(t) \equiv M_i$, was investigated by Henandez [55]. This stability analysis was performed for the nonlinear system (3.1) (i.e. $\dot{x} = x_1^{-1}(A(M)x + x_{np}e_1)$) by linearizing as usual at the steady state and showing that the spectrum of the resulting matrix is in the left-half of the complex plane, resulting in local stability. Because we have reparametrized to a linear system losing no information about the qualitative dynamics of the original system, once we show that the spectrum lies in the left half-plane, we have global asymptotic stability. In fact, we will show this result in the general case $n \geq 2$, and constant M_i.

The zeros of (3.4) must satisfy $x_1 = x_{\text{np}}/M_1$, and $x_j = M_j x_1$ for $j = 2, \dots, n$; or, in other words, the rest point is $x^* = (x_{\text{np}}/M_1)(1, M_2, \dots, M_n)^T$. We begin our

proof with some lemmas. Let $\sigma(X)$ denote the set of eigenvalues of the matrix X, let $\mathbb{R}^+ = [0, \infty)$, and $\mathbb{C}$ the complex numbers.

Lemma 1. *$\sigma(A(M)) \in \mathbb{C} \setminus \mathbb{R}^+$. Moreover, the characteristic equation of A may be written in two equivalent forms:*

$$\gamma_A = (M_1 + \lambda)\Pi_{i=2}^n (b_i + \lambda) + \lambda \sum_{j=2}^n M_j \Pi_{i=2, i\neq j}^n (b_i + \lambda) \tag{3.5}$$

and

$$\gamma_A(\lambda) = \left(\sum_{j=1}^n M_j + \lambda \right) \prod_{i=2}^n (b_i + \lambda) - \sum_{j=2}^n b_j M_j \prod_{i=2, i\neq j}^n (b_i + \lambda). \tag{3.6}$$

Proof. The characteristic equation $\gamma_A(\lambda)$ of A is given by

$$\begin{aligned} \gamma(\lambda) &= \det(A - \lambda I) \\ &= \det \begin{pmatrix} -\sum_{i=1}^n M_i - \lambda & 1 & 1 & \dots & 1 \\ b_2 M_2 & -b_2 - \lambda & 0 & \dots & 0 \\ b_3 M_3 & 0 & -b_3 - \lambda & \dots & 0 \\ \vdots & \vdots & \vdots & \ddots & \vdots \\ b_n M_n & 0 & 0 & \dots & -b_n - \lambda \end{pmatrix}. \end{aligned}$$

Expanding in minors along the first column, and examining them one by one, the first minor is

$$\begin{aligned} (-\sum_{i=1}^n M_i - \lambda) \det \begin{pmatrix} -b_2 - \lambda & 0 & \dots & 0 \\ 0 & -b_3 - \lambda & \dots & 0 \\ \vdots & \vdots & \ddots & \vdots \\ 0 & 0 & \dots & -b_n - \lambda \end{pmatrix} \\ = (-\sum_{i=1}^n M_i - \lambda) \prod_{i=2}^k (-b_j - \lambda) \\ = (-1)^k (M_1 + \lambda) \prod_{i=2}^k (b_j + \lambda). \end{aligned}$$

The subsequent minors are all similarly constructed. To find the j-th minor, we note it will be multiplied by $(-1)^{j-1}$. We reorder the columns: $(j, 2, 3, \ldots, j-1, j+1, \ldots, n)$, an operation with $j-2$ column switches producing an extra $(-1)^{j-2}$ factor, giving the product of $(-1)^{(j-2)+(j-1)} = -1$. We now have

$$\begin{aligned}
-b_j M_j \det &\begin{pmatrix} 1 & 1 & \ldots & 1 \\ 0 & -b_2-\lambda & \ldots & 0 \\ \vdots & \vdots & \ddots & \vdots \\ 0 & 0 & \ldots & -b_n-\lambda \end{pmatrix} \\
&= -b_j M_j \prod_{i=2, i\neq j}^{n} (-b_i - \lambda) \\
&= (-1)^{n-1} b_j M_j \prod_{i=2, i\neq j}^{n} (b_i + \lambda).
\end{aligned}$$

Adding all first column minors, we find that

$$\begin{aligned}
\gamma(\lambda) &= (-1)^n (\sum_{i=1}^{n} M_i + \lambda) \prod_{i=2}^{n} (b_i + \lambda) + \sum_{j=2}^{n} (-1)^{n-1} b_j M_j \prod_{i=2, i\neq j}^{n} (b_i + \lambda) \\
&= (-1)^n \left((\sum_{i=1}^{n} M_i + \lambda) \prod_{i=2}^{n} (b_i + \lambda) - \sum_{j=2}^{n} b_j M_j \prod_{i=2, i\neq j}^{n} (b_i + \lambda) \right). \qquad (3.7)
\end{aligned}$$

We have the characteristic equation (corresponding to (3.6))

$$\left(\sum_{j=1} M_j + \lambda \right) \prod_{i=2}^{n} (b_i + \lambda) - \sum_{j=2}^{n} b_j M_j \prod_{i=2, i\neq j}^{n} (b_i + \lambda) = 0.$$

Expanding the first term, we get

$$
\begin{aligned}
0 &= \underbrace{(M_1+\lambda)\prod_{i=2}^{n}(b_i+\lambda)}_{\mathbf{1}} + \sum_{j=2} M_j \prod_{i=2}^{n}(b_i+\lambda) - \sum_{j=2}^{n} b_j M_j \prod_{i=2, i\neq j}^{n}(b_i+\lambda) \\
&= \mathbf{1} + \sum_{j=2}^{n}\left(M_j(b_j+\lambda)\prod_{i=2,i\neq j}^{n}(b_i+\lambda) - b_j M_j \prod_{i=2,i\neq j}^{n}(b_i+\lambda)\right) \\
&= \mathbf{1} + \sum_{j=2}^{n} M_j(b_j+\lambda-b_j)\prod_{i=2,i\neq j}^{n}(b_i+\lambda) \\
&= \mathbf{1} + \sum_{j=2}^{n} \lambda M_j \prod_{i=2,i\neq j}^{n}(b_i+\lambda) \\
&= (M_1+\lambda)\prod_{i=2}^{n}(b_i+\lambda) + \sum_{j=2}^{n} \lambda M_j \prod_{i=2,i\neq j}^{n}(b_i+\lambda),
\end{aligned}
$$

which is Eq. (3.5), and thus (3.5)=(3.6). Because all M_j, and b_j for $j = 2, \ldots, n$, are strictly positive, this equality is only satisfied if $\lambda \notin \mathbb{R}^+$. □

Define the matrix

$$
B = \begin{pmatrix}
-\sum_{i=1}^{n} M_i & \sqrt{b_2 M_2} & \sqrt{b_3 M_3} & \ldots & \sqrt{b_n M_n} \\
\sqrt{b_2 M_2} & -b_2 & 0 & \ldots & 0 \\
\sqrt{b_3 M_3} & 0 & -b_3 & \ldots & 0 \\
\vdots & \vdots & \vdots & \ddots & \vdots \\
\sqrt{b_n M_n} & 0 & 0 & \ldots & -b_n
\end{pmatrix}.
$$

Lemma 2. $\sigma(B) = \sigma(A(M))$.

Proof. We will show that $\gamma_A(\lambda) = \gamma_B(\lambda)$. We simply perform the same minor decomposition as before on $\det(B - \lambda I)$. Examining the first term, we have as before

$$
(-M_1-\lambda)\prod_{i=2}^{n}(-b_i-\lambda) = (-1)^n (M_1+\lambda)\prod_{i=2}^{n}(b_i+\lambda).
$$

To find the j-th minor, we first note that it will be multiplied by $(-1)^{j-1}$. Now, we reorder the columns: $(j, 2, 3, \ldots, j-1, j+1, \ldots, n)$. This operation has $j-2$ column switches and thus produces an extra $(-1)^{j-2}$ factor, giving the product of

$(-1)^{(j-2)+(j-1)} = -1$. This yields the equality

$$
\begin{aligned}
-\sqrt{b_j M_j}\det &\begin{pmatrix} \sqrt{b_j M_j} & \sqrt{b_2 M_2} & \dots & \sqrt{b_n M_n} \\ 0 & -b_2-\lambda & \dots & 0 \\ \vdots & \vdots & \ddots & \vdots \\ 0 & 0 & \dots & -b_n-\lambda \end{pmatrix} \\
&= -b_j M_j \prod_{i=2, i\neq j}^{n} (-b_i - \lambda) \\
&= (-1)^{n-1} b_j M_j \prod_{i=2, i\neq j}^{n} (b_i + \lambda).
\end{aligned}
$$

Adding all minors, and noting the characteristic equation of A in the form (3.7) it follows that

$$
\gamma_B(\lambda) = (-1)^n \left((M_1+\lambda)\prod_{i=2}^{n}(b_i+\lambda) - \sum_{j=2}^{n} b_j M_j \prod_{i=2, i\neq j}^{n} (b_i+\lambda) \right) = \gamma_A(\lambda).
$$

□

Because of its symmetry, we immediately have that the matrix B has only real eigenvalues, and in combination with the first lemma, we have the following result.

Theorem 3. *If the function $M(t)$ is constant, then the rest point*

$$x^* = (x_{np}/M_1)(1, M_2, \dots, M_n)^T$$

of the system $\dot{x} = A(M)x + x_{np}e_1$ is globally asymptotically stable. Moreover, the rest point x_* of system (3.2) *is globally asymptotically stable.*

3.2.2 Rate of approach to the rest point

Proposition 4. *For M_1 near zero, $\lambda_1(M_1) = -(1 + \sum_{j=2}^{k} M_j/b_j)^{-1} M_1 + O(M_1^2)$.*

Proof. By inspection of the characteristic equation of A in the form (3.5), if $M_1 = 0$ there is a zero eigenvalue $\lambda_1 = \lambda_1(M_1)$. The remaining (negative) eigenvalues λ_j,

$(j = 2, \ldots, k)$ are roots of

$$\lambda \prod_{i=2}^{n}(b_i + \lambda) + \sum_{j=2}^{n} \lambda M_j \prod_{i=2, i\neq j}^{n} (b_i + \lambda) = 0.$$

Apply the Implicit Function Theorem to the function $\gamma_A(\lambda, M_1) = (M_1 + \lambda\Pi_{j=2}^{n}(b_j + \lambda) + \lambda \sum_{j=2}^{n} M_j \Pi_{i=2, i\neq j}^{n}(b_j + \lambda)$ at $(\lambda, M_1) = (0, 0)$, and then compute the derivative of the implicit function $\lambda = h(M_1)$. □

This makes intuitive sense because $\lim_{M_1 \to 0} x^* = (\infty, \ldots, \infty)$.

For the lower bound, we can employ a standard eigenvalue result (see [84])[1]

Theorem 5. *Let $A \in \mathbb{M}^{n\times n}$, then for any eigenvalue λ of A, we have $|\lambda| \leq \max_i \sum_j |a_{ij}|$.*

Thus the minimal eigenvalue, λ_n is bounded below by

$$-\max_{i=2,\ldots,k}\{\sum_{i=1}^{n} M_i + \sum_j \sqrt{M_j b_j}, \sqrt{M_i b_i} + b_i\}. \tag{3.8}$$

3.3 Optimal Control

3.3.1 Controllability

Consider a control process

$$\dot{x} = f(x, u), \quad x(0) = x_0, \tag{3.9}$$

[1]Note: Application of the Gershgorin Circle Theorem yields exactly the same result:

$$\begin{aligned}
\min \lambda &= \min \cup_{i=1}^{k} \left\{ z \in \mathbb{C} : |z - a_{ii}| \leq \sum_{j\neq i} |a_{ij}| \right\} \\
&= \min \left\{ z \in \mathbb{R}^- : \cup_{i=2}^{k} \left\{ z \in \mathbb{C} : |z + b_i| \leq \sqrt{b_i M_i} \right\} \cup \{ z \in \mathbb{C} : |z + M_1| \leq \sum_{i=2} \sqrt{b_i M_i} \right\} \\
&= -\max\{M_1 + \sum_j \sqrt{M_j b_j}, \sqrt{M_i b_i} + b_i\} \text{ for } i = 2, \ldots, k.
\end{aligned}$$

In fact, in general, if all diagonal entries are negative, these two results will always yield the same minimal eigenvalue (or maximal in the case where all entries are positive).

where $f \in C^1(\mathbb{R}^n \times \mathbb{R}^m, \mathbb{R}^n)$. We prescribe an m-tuple of numbers $\bar{M}_i > 0$ for $i = 1, 2, \ldots, m$, the admissible control parameter set

$$\text{CP} = \{M = (M_1, M_2, \ldots, M_m) \in \mathbb{R}^m : 0 \leq M_i \leq \bar{M}_i \text{ for } i = 1, 2, \ldots, m\}, \quad (3.10)$$

and the state space $S \subset (0, \infty) \times [0, \infty)^n$ (i.e. we do not allow $x_1 = 0$). In addition, we define $x(t) = x(t; x_0, u)$ to be the solution of the initial value problem (3.9) and

$$\mathcal{C}_y(t) = \{x_0 \in S : x(t) := x(t; x_0, u) = y\},$$

the set of initial conditions that can be steered to $y \in S$ at time t via a measurable, admissible control function $u : \mathbb{R} \to \text{CP}$. Furthermore we define $\mathcal{C}_y = \cup_{t \geq 0} \mathcal{C}_y(t)$, and say that our control system is *null controllable* if $\mathcal{C}_0 = \mathbb{R}^n$. Finally, we define the controllability matrix function $G : \mathbb{M}^{n \times n} \times \mathbb{M}^{n \times m} \to \mathbb{M}^{n \times mn}$ by

$$G(A, B) := [B|AB|A^2B| \ldots |A^{n-1}B].$$

The next theorem is a fundamental result in optimal control theory (see for example [71]).

Theorem 6. *For system* (3.9)*, suppose that* $\Omega \subset \mathbb{R}^m$*,* $0 \in \operatorname{int} \Omega$*, and* $f(0, 0) = 0$*. Also, define* $A_f = (\partial f/\partial x)(0, 0)$ *and* $B_f = (\partial f/\partial u)(0, 0)$*. If* $\operatorname{rank} G(A_f, B_f) = n$ *and* 0 *is an asymptotically stable rest point of the system* $\dot{x} = f(x, 0)$*, then* $\mathcal{C}_0 = \mathbb{R}^n$*.*

For this chapter we adapt the notion of a bilinear control system defined by Mohler: a system is bilinear in state x and control vector $u \in \mathbb{R}^m$ if

$$\begin{aligned} \dot{x} &= f(x, M) \\ &= Ax + \sum_j B_j u_j x + Cu \end{aligned} \quad (3.11)$$

for appropriately sized matrices A, B_j and C. We apply Theorem 6 to the case of a bilinear system with shifted coordinates.

Corollary 7. *Suppose that f is bilinear as defined in 3.11,* $\mathrm{CP} \subseteq \mathbb{R}^m$*, and $x^* \in \mathbb{R}^n$ and $u^* \in \operatorname{int}\Omega$ are such that $f(x^*, u^*) = 0$. Define $\bar{A}_f = (\partial f/\partial x)(x^*, u^*)$ and $\bar{B}_f = (\partial f/\partial u)(x^*, u^*)$. If $\operatorname{rank} G(\bar{A}_f, \bar{B}_f) = n$ and x^* is an asymptotically stable rest point of the system $\dot{x} = f(x, u^*)$, then $\mathcal{C}_{x^*} = \mathbb{R}^n$.*

Proof. Suppose $f(x^*, u^*) = 0$ and define $f_1(x, u) = f(x^* - x, u^* - u)$. We have that $f_1(0, 0) = 0$, and (by the bilinearity) $f_1(x, u) = f(x, u) - f(x, u^*) - f(x^*, u) + f(x^*, u^*)$. Using the bilinearity again, it follows that

$$(D_x f_1)(0, 0) = A_f(0, 0) - A_f(0, u^*) = A_f(0, -u^*) = -\bar{A}_f(x^*, u^*).$$

Similarly,

$$(D_u f_1)(0, 0) = B_f(0, 0) - B_f(x^*, 0) = -B_f(x^*, 0) = -\bar{B}_f(x^*, u^*).$$

We have

$$\begin{aligned} n &= \operatorname{rank}[\bar{B}_f | \bar{A}_f \bar{B}_f | \bar{A}_f^2 \bar{B}_f | \cdots | \bar{A}_f^{n-1} B_f] \\ &= \operatorname{rank}[-\bar{B}_f | \bar{A}_f \bar{B}_f | - \bar{A}_f^2 \bar{B}_f | \cdots | (-1)^{n-2} \bar{A}_f^{n-1} \bar{B}_f] \\ &= \operatorname{rank}[B_f | A_f B_f | A_f^2 B_f | \cdots | A_f^{n-1} B_f]. \end{aligned}$$

and because x^* is asymptotically stable for $\dot{x} = f(x, u^*)$, the state 0 is asymptotically stable for $\dot{x} = f_1(x, 0)$. □

We apply this corollary to the bilinear system (3.4) by noting that $A_f(x^*, u^*) = A(M^*)$ and $B_f(x^*, u^*) = x_1^* B_1$. Since $x_1^* B_1$ is an $n \times n$ upper triangular matrix with

non-zero diagonal entries, the first n columns are linearly independent and thus the rank of $G(A(M^*), x_1^* B_1) = n$.

Finally, we combine Theorem 3 with Corollary 7 to obtain the following result.

Theorem 8. *For system (3.4),* $\mathcal{C}_{x^*} = \mathbb{R}^n$.

3.3.2 Existence of an optimal control

The existence of an optimal control for systems of the form (3.11) with bounded controls is a standard result, see Lee and Markus, Corollary 2, p. 262 [71].

3.3.3 A control problem

We will investigate the time-optimal control problem (for the special case of system (3.9) given by system (3.2)) of steering an initial state x^i to a final state x^f in minimal time using controls in the admissible set $\mathbb{A}$ which is the set of measurable functions $M : \mathbb{R} \to \text{CP}$, and CP is defined in display (3.10). This control problem has wide applications in biology because it is often desirable to implement the control of an extracellular environment in such a way as to minimize exposure time.

Problem 9. *Given an initial state* x^i *in the state space* S *and final state* $x^f \in S$*, the set of admissible controls* $\mathbb{A}$ *and defining* $t^* \in \mathbb{R}$ *to be the first time that* $x(t^*) = x_f$ *for the solution of the previously defined initial value problem*

$$\dot{x} = A(M)x + x_{np}e_1, \quad x(0) = x^i \tag{3.12}$$

with state constraint $g(x) \leq 0$*, determine a control that maximizes the functional*

$$P(M) := -\int_0^{t^*} x_1(t)\, dt$$

over $\mathbb{A}$.

Our basic tool for attacking this time-optimal control problem is the Pontryagin Maximum Principle (see Lee and Markus for example [71]), which is stated in the form that we will use in Appendix A-2 for the convenience of the reader.

For our model system (3.12), we wish to minimize the payoff functional

$$P[M(\cdot)] = -\int_0^{t^*} x_1(s)ds, \tag{3.13}$$

which is negative "real" time from our conversion formula (3.3).

For our control system (3.2), which we also view in the compact form $\dot{x} = f(x, M)$ with $x \in \mathbb{R}^n$, we define the (control theory) Hamiltonian

$$H(x, p, M) = f(x, M) \cdot p - x_1.$$

The state of the system satisfies the differential equation $\dot{x} = \nabla_p H(x, p, M) = f(x, M)$ and the costate satisfies $\dot{p} = -\nabla_x H(x, p, M)$. In our case, the state equation has the explicit form $\dot{x} = A(M)x + x_{np}e_1$ and the costate equation is given by $\dot{p} = -A(M)^T p + e_1$.

For Problem 9 (even in the $n > 2$ dimensional case), we can immediately deduce the nature of the optimal controls by applying the maximum principal: we have the Hamiltonian

$$H(x, p, M) = (A(M)x + x_{np}e_1) \cdot p - x_1 = (x_1 B_1 M + B_2 x + x_{np}e_1) \cdot p - x_1, \tag{3.14}$$

and we must find $M \in \mathbb{A}$ such that $H(x,p,M)$ is maximized. Thus we maximize

$$\begin{aligned} H(x,p,M) &= (A(M)x + x_{np}e_1)\cdot p - x_1 \\ &= \left(-\sum_{i=1}^{n} M_i x_1 + \sum_{i=2}^{n} x_i + x_{np}\right) p_1 + \sum_{i=2}^{n}(M_i b_i x_1 - b_i x_2)p_i - x_1 \\ &= -\sum_{i=1}^{n} M_i x_1 p_1 + \ldots + \sum_{i=2}^{n}(M_i b_i x_1 - b_i x_i)p_i + \ldots \\ &= -M_1 x_1 p_1 + x_1 \sum_{i=2}^{n} M_i(b_i p_i - p_1) + \ldots, \end{aligned}$$

where the ellipses represent terms that we may ignore because they are not affected by the controls M_i. This expression is maximized when

$$M_1(t) = \begin{cases} 0, & p_1 > 0 \\ \bar{M}_1, & p_1 \leq 0 \end{cases} \quad \text{and} \quad M_i(t) = \begin{cases} 0, & b_i p_i - p_1 < 0 \\ \bar{M}_i, & b_i p_i - p_1 \geq 0 \end{cases}. \tag{3.15}$$

3.3.4 Synthesis of the optimal control in the case $n = 2$.

To synthesize the optimal control for $n > 2$ becomes a technical challenge due to the number of state and costate cases one must consider. Therefore, we will construct the optimal control in the commonly encountered and biologically important case where there is one permeating and one non-permeating solute and $n = 2$.

In the unconstrained case, the maximum principle limits the synthesis to four possible control schemes, $M^I, \ldots, M^{IV}$ associated with four regions $(\Pi^I, \ldots, \Pi^{IV})$ in costate space:

$$\Pi_I := \{p \in \mathbb{R}^2 : p_1 < 0, b_2 p_2 - p_1 > 0\},$$

$$\Pi_{II} := \{p \in \mathbb{R}^2 : p_1 > 0, b_2 p_2 - p_1 > 0\},$$

$$\Pi_{III} := \{p \in \mathbb{R}^2 : p_1 > 0, b_2 p_2 - p_1 < 0\},$$

$$\Pi_{IV} := \{p \in \mathbb{R}^2 : p_1 < 0, b_2 p_2 - p_1 < 0\},$$

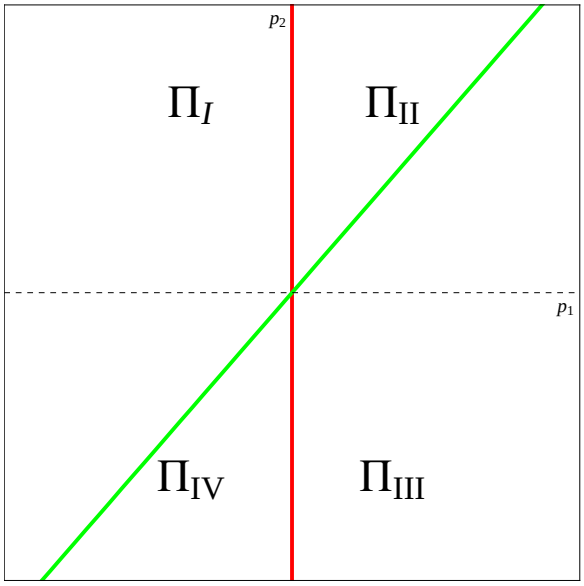

Figure 3.1: Plot of the costate regions $\Pi_I, \Pi_{II}, \Pi_{III}, \Pi_{IV}$, defined by the maximum principle.

(see Fig. 3.1), and the control schemes for initial points in each region (Table 3.1).

Define $S^* := \{x \in S : x_1 > x_{np}/\bar{M}_1, 0 \leq x_2 < \bar{M}_2 x_1\}$ to be the region in the state space where x^i and x^f may reside, and define sets $P^0 = \{x^f\}$, $P^1 = \cup_{i=1}^4 \sigma^i$, and $P^2 = S$, where

$$\sigma^i := \{x \in S : \phi_t^\lambda(x_f) = x \text{ for some } t < 0\},$$

and $\phi_t^\lambda(x_f)$ is the solution of $\dot{x} = f(x, \lambda)$ from initial point x^f under control scheme $\lambda = M^I, M^{II}, M^{III}$, or M^{IV} (see Fig. 3.2). We define regions A, B, C and D as follows. Let $\mathcal{A} \subset S$ be the region bounded by $\partial S \cup \sigma^I \cup \sigma^{II} \cup \{x^f\}$ that does not contain $\sigma^{III} \cup \sigma^{IV}$. Let $\mathcal{B} \subset S$ be the region bounded by $\partial S \cup \sigma^{II} \cup \sigma^{III} \cup \{x^f\}$ that does not contain $\sigma^{IV} \cup \sigma^I$. Let $\mathcal{C} \subset S$ be the region bounded by $\partial S \cup \sigma^{III} \cup \sigma^{IV} \cup \{x^f\}$ that does not contain $\sigma^I \cup \sigma^{II}$. Let $\mathcal{D} \subset S$ be the region bounded by $\partial S \cup \sigma^{IV} \cup \sigma^I \cup \{x^f\}$ that does not contain $\sigma^{II} \cup \sigma^{III}$.

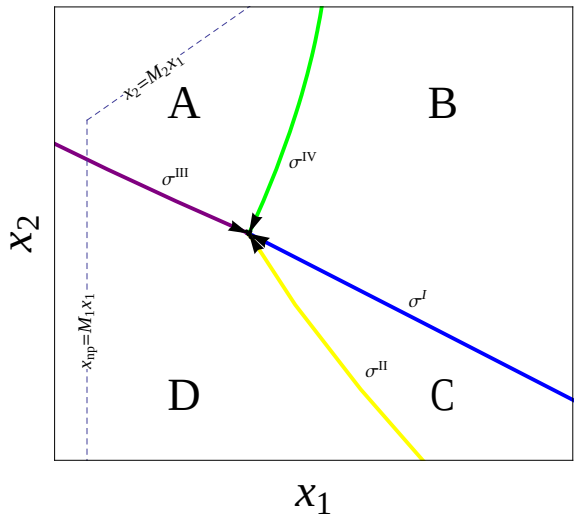

Figure 3.2: Typical plot of the state regions. The geometry of the regions changes as a function of x^f, the "source" of the σ^i, though the regions remain bounded by the same σ^i. Also, S^* is bounded on the left and above by the dashed lines $x_1 = M_1 x_{np}$ and $x_2 = M_2 x_1$.

Using the notation just developed, we define $v : S \to U$:

$$v(x) = \begin{cases} M^I & x \in \sigma^I \\ M^{II} & x \in \mathcal{C} \cup \mathcal{D} \cup \sigma^{II} \\ M^{III} & x \in \sigma^{III} \\ M^{IV} & x \in \mathcal{A} \cup \mathcal{B} \cup \sigma^{IV} \end{cases}, \tag{3.16}$$

which defines control schemes (see Table 3.1) for initial points $x^i \in \operatorname{int} S^*$ in the subregions (see Table 3.2).

Theorem 10. *The trajectory defined by $\dot{x} = f(x, v(x))$ where v is defined by* (3.16) *is optimal.*

To prove this theorem below, we will use the classic result of Boltayanski, which states that any "regular" and "distinguished" control is optimal [18]. The conditions for regular and distinguished controls are listed in Section A-3.

Next we introduce what seem like two unexpected results. For initial points in regions $\mathcal{A}$ and $\mathcal{D}$ there are simple formulas that describe the total transit time t^* that

Table 3.1: The Pontryagin Maximum Principle along with the Hamiltonian for the $n = 2$ system define the possible optimal control schemes M^I, M^{II}, M^{III}, and M^{IV}.

Control Scheme	M_1	M_2
M^I	$\bar{M}_1$	$\bar{M}_2$
M^{II}	0	$\bar{M}_2$
M^{III}	0	0
M^{IV}	$\bar{M}_1$	0

Table 3.2: Control schemes in the subregions of S. Our synthesis will be constructed for initial and final points x^i and x^f in S divided into four regions $\mathcal{A}, \mathcal{B}, \mathcal{C}$ and $\mathcal{D}$. For each region the First Control is used until a defined switching time τ after which the Second Control is used. In the unconstrained case, the control $M(t)$ is piecewise constant.

Region	First Control	Second Control
$\mathcal{A}$	M^{IV}	M^{III}
$\mathcal{B}$	M^{IV}	M^I
$\mathcal{C}$	M^{II}	M^I
$\mathcal{D}$	M^{II}	M^{III}

are not dependent on the maximal concentration; i.e. as long as the starting point lies in either $\mathcal{A}$ or $\mathcal{D}$ the total transit time is solely determined by x^i, x^f, x_{np}, and b_2!

Theorem 11. *For $x^i \in \mathcal{D}$, the total optimal transit time under the associated control scheme is $t^* = \frac{x_1^f - x_1^i}{x_{np}} + \frac{x_2^f - x_2^i}{b_2 x_{np}}$. For $x^i \in \mathcal{A}$, the total optimal transit time under the associated control scheme is $t^* = \frac{1}{b_2} \ln(x_2^i / x_2^f)$.*

The proof of this theorem relies on Lemma 14 necessary to prove Theorem 10. There may be similar formulae for other regions, but the equations become much more complicated in these cases.

This first lemma shows that there are no rest points of the controlled systems in the interior of S.

Lemma 12. *For $x^f \in S^*$, there are no rest points of system $\dot{x} = f(x, v(x))$ in* $\operatorname{int} S \setminus \sigma^I$.

Proof. In regions $\mathcal{C} \cup \mathcal{D} \cup \sigma^{II} \cup \sigma^{III}$, $M_1 = 0$, and there is no rest point. In regions $\mathcal{A} \cup \mathcal{B} \cup \sigma^{IV}$, $M_2 = 0$, and the rest point is at $(x_{\text{np}}/M_1)(1,0)^T$. Region $\mathcal{A}$ is bounded by σ^{III} and σ^{IV}, for which $M_2 = 0$, because of this, in negative time, $\dot{x}_2 > 0$, and thus for all $x^f \in S^*$, $\mathcal{A}$ is bounded away from the x_1-axis. For region $\mathcal{B}$, because σ^{IV} is bounded away from the x_1-axis, it remains to show that if σ^I intersects the x_1-axis, it does so for $x_1 > x_{\text{np}}/\bar{M}_1$ (e.g. $\mathcal{B}$ is bounded away from the associated rest point). But, for $x^f \in S^*$, $x_1 > x_{np}/\bar{M}_1$ and $x_2 < \bar{M}_2 x_1$. In this case, in negative time $\dot{x}_1 = (M_1 + M_2)x_1 - x_2 - x_{np} > x_{np} + M_2 x_1 - M_2 x_1 - x_{np} = 0$, thus σ^I intersects the x_1-axis at $x_1 > x_{np}/\bar{M}_1$. □

The next lemma states that at every point in the interior of S the vector fields defined by the four controls are not parallel.

Lemma 13. *If $x \in \sigma^{III} \cap \operatorname{int} S$, then $f(x, M^{IV})$ and $f(x, M^{III})$ are not parallel.*

If $x \in \sigma^{I} \cap \operatorname{int} S$, then $f(x, M^{IV})$ and $f(x, M^{I})$ are not parallel.

If $x \in \sigma^{III} \cap \operatorname{int} S$, then $f(x, M^{II})$ and $f(x, M^{III})$ are not parallel.

If $x \in \sigma^{I} \cap \operatorname{int} S$, then $f(x, M^{II})$ and $f(x, M^{I})$ are not parallel.

Proof. Let $\eta \in \mathbb{R}$. If $x \in \partial S^*$ and $x_1 = M_1 x_{np}$, then $-f(x, M^I) \cdot (1, 0) > 0$. Also if $x \in \partial S^*$ and $x_2 = M_2 x_1$, then $-f(x, M^I) \cdot (0, 1) < 0$. Thus, for all $x^f \notin \partial S^*$, $\sigma^I \cap (\partial S^* \setminus \mathbb{R} \times \{0\}) = \emptyset$. Now suppose $x \in \mathbb{R} \times \{0\}$. Then $-f(x, M^{III}) \cdot (0, 1) > 0$, therefore for all $x^f \notin \mathbb{R} \times \{0\}$, $\sigma^{III} \cap \mathbb{R} \times \{0\} = \emptyset$. The solution of $f(x, M^{IV}) = \eta f(x, M^{III})$ is $x_1 = (x_{np}/M_1)(1-\eta)$, $x_2 = 0$. The solution of $f(x, M^{IV}) = \eta f(x, I)$ is $x_1 = x_{np}/M_1$, $x_2 = (M_2 x_{np}\eta)/(M_1(\eta-1))$. This solution is not in $\operatorname{int} S$ for all η. There is no solution of $f(x, M^{II}) = \eta f(x, M^{III})$. The solution of $f(x, M^{II}) = \eta f(x, M^I)$ is $x_1 = (x_{np}/\eta M_1)(1-\eta)$, $x_2 = (M_2 x_{np}/M_1\eta)(\eta - 1)$. Factoring out $(x_{np}/\eta M_1)(1-\eta)$, we get $(x_{np}/\eta M_1)(1-\eta)(1, M_2)$. This parametrizes the boundary $x_2 = x_1 M_2$ of S^f, and thus is not in $\operatorname{int} S$ for all η. □

This next lemma states that given initial points in each region $\mathcal{A}, \mathcal{B}, \mathcal{C}, \mathcal{D}$, the flow along the solution given by the associated control intersects the expected boundary curve σ^i in finite time.

Lemma 14. *(1) Given an initial point $x \in \mathcal{A}$, there exists a time $\tau_1 > 0$ such that $\phi^{IV}_{\tau_1}(x)$ intersects σ^{III}. (2) Given an initial point $x \in \mathcal{B}$, there exists a time $\tau_1 > 0$ such that $\phi^{IV}_{\tau_1}(x)$ intersects σ^{I}. (3) Given an initial point $x \in \mathcal{C}$, there exists a time $\tau_1 > 0$ such that $\phi^{II}_{\tau_1}(x)$ intersects σ^{I}. (4) Given an initial point $x \in \mathcal{D}$, there exists a time $\tau_1 > 0$ such that $\phi^{II}_{\tau_1}(x)$ intersects σ^{III}.*

Proof. By Lemma 12 there are no rest points within any of the regions under the control v. We claim that S is invariant for all controls. In fact, on the x_1-axis, all controls have $\dot{x}_2 \geq 0$, and on the x_2-axis, all controls have $\dot{x}_1 \geq 0$. From Lemma 12 and Theorem 3, regions $\mathcal{A}$ and $\mathcal{B}$ are bounded away from the asymptotically stable rest point associated with their control, and thus from any initial point in $\mathcal{A}$ or $\mathcal{B}$, the flow must cross $\partial\mathcal{A}$ or $\partial\mathcal{B}$ respectively. Because the control in both regions is M^{IV}, by the uniqueness of solutions of ODEs the flow will not cross σ^{IV}, and thus (1) and (2) are proved. Now note that for $x \in S^*$, $f(x, M^I)$ and $f(x, M^{II})$ have a positive second component, thus σ^I and σ^{II} (which flow in negative time) will always intersect the x_1-axis, and region $\mathcal{C}$ will be bounded away from $x_2 > x_2^f$. Moreover, for $x \in S$, the first component of $f(x, M^{III})$ is positive, σ^{III} must intersect the x_2 axis, and thus region $\mathcal{D}$ is bounded. Finally, for $x \in S^*$, $f(x, M^{II})$ has a positive second component. Thus for $x^i \in \mathcal{C} \cup \mathcal{D}$, $\phi_t^{M^{II}}(x^i)$, must intersect $\partial\mathcal{C} \cup \partial\mathcal{D}$, and as above, because the control in both regions is M^{II}, by the uniqueness of solutions of ODEs the flow will not cross σ^{II}, and thus (3) and (4) are proved. □

Lemma 15. *The transit time $\tau(x^i)$ from x^i to x^f is a continuous function of the initial point x^i.*

Proof. Let $y \in \sigma^i$, define $\tau_2(y)$ to be the time to reach x^f while flowing along σ^i, and define $F(t, x, y) := \phi(t, x, \lambda) - y$. By Lemma 14, for each $x^i \in G$ there exists a τ_1 such that $\phi(\tau_1, x, v(x)) \in \sigma^i$. Thus, we have $F(\tau_1, x, y) = 0$. Because there exist no rest points, $\frac{d}{dt}F(t, x, y)|_{t=\tau_1} \neq 0$ and we may apply the implicit function theorem yielding $\tau^1(x)$ is C^1 in a neighborhood of x, thus the transit time $\tau(x) = \tau_1(x) + \tau_2(\phi(\tau^1(x), x, II))$ is continuous. □

Next we examine whether there exists a costate that will satisfy the Pontryagin Maximum Principle.

Lemma 16. *The lines ℓ_{II} defined by the solution of $H(x(0), p(0), M^{II}) = 0$ and ℓ_{IV} defined by the solution of $H(x(0), p(0), M^{IV}) = 0$ are not parallel to the line $b_2 p_2 = p_1$.*

Proof. Setting the initial Hamiltonian for control M^{II} equal to zero, we get

$$\begin{aligned} H(x(0), p(0), M^{II}) &= \begin{pmatrix} -M_2 x_1^i + x_2^i + x_{np} \\ M_2 b_2 x_1^i - b_2 x_2^i \end{pmatrix} \cdot \begin{pmatrix} p_1 \\ p_2 \end{pmatrix} + x_1^i, \\ &= (-M_2 x_1^i + x_2^i + x_{np}) p_1 + (M_2 b_2 x_1^i - b_2 x_2^i) p_2 + x_1^i, \\ &= 0. \end{aligned}$$

We solve this for

$$b_2 p_2 = \frac{M_2 x_1^i - x_2^i - x_{np}}{M_2 x_1^i - x_2^i} p_1 - \frac{x_1^i}{M_2 x_1^i - x_2^i}.$$

Note that $\frac{M_2 x_1^i - x_2^i - x_{np}}{M_2 x_1^i - x_2^i} = 1$ if and only if $M_2 x_1^i - x_2^i - x_{np} = M_2 x_1^i - x_2^i$. But, reducing this equation we get $x_{np} = 0$ in contradiction since $x_{np} > 0$. Next, for control M^{IV}, we have

$$\begin{aligned} H(x(0), p(0), M^{IV}) & \begin{pmatrix} -M_1 x_1^i + x_2^i + x_{np} \\ -b_2 x_2^i \end{pmatrix} \cdot \begin{pmatrix} p_1 \\ p_2 \end{pmatrix} + x_1^i \\ &= (-M_1 x_1^i + x_2^i + x_{np}) p_1 - b_2 x_2^i p_2 + x_1^i \\ &= 0. \end{aligned}$$

We solve this for $b_2 p_2 = (-M_1 x_1^i + x_2^i + x_{np})/x_2^i + x_1^i/x_2^i$. Now $(-M_1 x_1^i + x_2^i + x_{np})/x_2^i = (x_{np} - M_1 x_1^i)/x_2^i + 1 < 1$, since $x_{np} < M_1 x_1^i$. □

Proposition 17. *Given Problem 9 with an initial point $x^i \in S^* \setminus \cup_{i=I}^{IV} \sigma^i$, with its associated optimal control scheme λ, switching time τ^1, and the control scheme's*

associated initial and final costate regions (Π^i and Π^f, respectively), there exists a costate p such that for all $t > 0$, the Hamiltonian $H(x, p, \lambda) := f(x, \lambda) \cdot p + x_1 = 0$, and $p(t)$ solves $\dot{p} = -\nabla_x H(x, p, \lambda)$ such that $p(t) \in \Pi^i$ for $t < \tau^1$, $p(\tau^1) \in \partial\Pi^i$ and $p(t) \in \Pi^f$ for $t > \tau_1$.

Proof. We must show that for each control scheme and time $\tau^1 > 0$, there exists an initial costate such that $p(t) \in \Pi^i$ for $t < \tau^1$, $p(\tau^1) \in \partial\Pi^i$ and $p(t) \in \Pi^f$ for $t > \tau^1$. We need only consider $\Pi^i = \Pi_{II}$ and the $\Pi^i = \Pi_{IV}$ cases . In both cases $H(x(0), p(0), \lambda) = 0$ defines a line ℓ in the costate space with non-infinite slope that, by Lemma 16, also does not equal $1/b_2$. In the Π_{II} case, the costate dynamics are governed by

$$\begin{pmatrix} \dot{p}_1 \\ \dot{p}_2 \end{pmatrix} = \begin{pmatrix} M_2 p_1 - M_2 b_2 p_2 + 1 \\ -p_1 + b_2 p_2 \end{pmatrix}. \tag{3.17}$$

It is easy to check that this system has an invariant line defined by $p_2 = p_1/b_2 + 1/(b_2^2 + \bar{M}_2 b_2)$ that by Lemma 16 will intersect ℓ. We claim that for $p \in \Pi_{II}$ such that $p_2 > p_1/b_2 + 1/(b_2^2 + \bar{M}_2 b_2)$, there exists a $t < \infty$ such that the solution of (3.17) intersects the p_2-axis at time τ^1.

We first let $p_2 > p_1/b_2 + 1/M_2 b_2$. In this case $\dot{p}_1 < 0$ and $\dot{p}_2 > 0$, so we must flow toward the p_2-axis, and since $\lim_{p_2 \to \infty} \dot{p}_2/\dot{p}_1 = -1/M_2$, the flow will never "blow up" to $p_2 = \infty$ before crossing the p_2-axis. Now for $p_1/b_2 + 1/M_2 b_2 > p_2 > p_1/b_2 + 1/(M_2 b_2 + b_2^2)$, $\dot{p}_2 > 0$. Thus for such p, p_2 will increase until $p_2 > p_1/b_2 + 1/M_2 b_2$ and we are done. Next let $p_2 < p_1/b_2 + 1/(M_2 b_2 + b_2^2)$. Taking $\lim_{p_1 \to \infty} \dot{p}_2/\dot{p}_2 = -1/M_2$, and $\lim_{p_1 \to \infty} \dot{p}_2 = -\infty$, therefore as p_1 gets large, the direction of the flow is downward and will cross the line $p_2 = p_1/b_2$.

For the Π_{IV} case, the costate dynamics are governed by

$$\begin{pmatrix} \dot{p}_1 \\ \dot{p}_2 \end{pmatrix} = \begin{pmatrix} M_1 p_1 + 1 \\ -p_1 + b_2 p_2 \end{pmatrix}.$$

We can check that this system has an invariant line at $p_1 = -1/\bar{M}_1$. For p such that $p_1 > -1/\bar{M}_1$, $\dot{p}_1 > 0$, and for p such that $p_1 < -1/\bar{M}_1$, $\dot{p}_1 < 0$ and $\lim_{p_1 \to -\infty} \dot{p}_2 = +\infty$ with $\lim_{p_1 \to -\infty} \dot{p}_2/\dot{p}_1 = -1/M$, therefore as $-p_1$ gets large, the direction of the flow is upward and will cross the p_1-axis.

Thus, in both cases we can find an initial point along ℓ such that, following the respective dynamics, p reaches $\partial\Pi^i$ at $t = 0$ and at $t = \infty$. By continuity there exists an initial point such that p reaches $\partial\Pi^i$ at $t = \tau^1$.

We must show that once in Π^f, we remain there for all time. For $\Pi^f = \Pi_{III}$, we claim Π_{III} is invariant because under control M^{III}, along $p_2 = p_1/b_2$, $\dot{p}_2 = 0$, and $\dot{p}_1 = 1$, and along the $p_2 = 0$ axis, $\dot{p}_1 = M_2 p_1 + 1 > 0$. Therefore for $\Pi^f = \Pi_{III}$, once the costate flow enters Π^f, it never leaves. For $\Pi^f = \Pi_I$, the flow may approach Π_I from either Π_{II} or Π_{IV}.

In the case $\Pi^i = \Pi_{II}$, the system is governed by

$$\begin{pmatrix} \dot{p}_1 \\ \dot{p}_2 \end{pmatrix} = \begin{pmatrix} (M_1 + M_2)p_1 - M_2 b_2 p_2 + 1 \\ -p_1 + b_2 p_2 \end{pmatrix}. \tag{3.18}$$

From the above analysis we have shown that $p_2 > 1/M_2 b_2$ when the boundary is traversed. For such p, $\dot{p}_1 < (M_1 + M_2)p_1 < 0$. Moreover, along the line $p_2 = 1/M_2 b_2$, $\dot{p}_2 = -p_1 + 1/M_2 > 0$ for $p_1 < 0$. Therefore, if we enter Π_I from Π_{II}, we remain in it for all time. Finally, if we enter Π_I from Π_{IV}, from the above analysis, $p_1 < -1/M_1$, and $p_2 > p_1/b_2$. In this case $\dot{p}_1 = (M_1 + M_2)p_1 - M_2 b_2 p_2 + 1 < M_1 p_1 + M_2 p_2 - M_2 p_1 + 1 < -1 + 1 = 0$. □

We are now ready to prove that the control is optimal.

Proof of Theorem 10. We must show that the controlled trajectory satisfies all conditions outlined in Section A-3.

For conditions (1) and (2): define $P^0 = \{x^f\}$ to be the lone zero-dimensional cell, and it will be of the second kind. Likewise $P^2 = \operatorname{int} S$ will be made up of cells A, B, C, and D of the first kind. Note that $P^2 - (P^{i-1} \cup N) = \mathcal{A} \cup \mathcal{B} \cup \mathcal{C} \cup \mathcal{D}$. Finally, let $P^1 = \{\sigma^i\}_{i=I}^{IV}$ where the σ^i are 1-dimensional cells of the second kind. Since v is constant in each cell $\mathcal{A}, \mathcal{B}, \mathcal{C}, \mathcal{D}$, and each σ^i, it is continuous and continuously differentiable and can be extended as a continuously differentiable function into a neighborhood of each cell.

For condition (3):

(a) We begin by showing that each point of the 2-dimensional cells $\mathcal{A}, \mathcal{B}, \mathcal{C}$, and $\mathcal{D}$ has a unique trajectory passing through it. Since $v(x)$ is constant in each cell, uniqueness is given; and by Lemma 12, for each cell, there are no rest points of the system.

(b) By Lemma 13 we show that the initial trajectories from regions $\mathcal{A}, \mathcal{B}, \mathcal{C}$, and $\mathcal{D}$ "pierce" their corresponding σ^i, and by Lemma 14, the trajectory leaves the cell ($\mathcal{A}, \mathcal{B}, \mathcal{C}$, or $\mathcal{D}$) in finite time.

(c) By definition the trajectories in σ^i approach the zero dimensional cell, and by Lemma 12 there is no rest point along any of the σ^i.

(d) We do not have any of these cases.

For condition (4): We have defined a unique distinguished trajectory such that only two cells are traversed before reaching x^f.

For condition (5): This is shown in Proposition 17.

For condition (6): This is shown in Lemma 15. □

Now that we know that the control is optimal, we can prove the total transit time result.

Proof of Theorem 11. First, we address points in region $\mathcal{D}$. By Theorem 10, the control M^{II} for $0 \le t \le \tau$ and M^{IV} for $\tau < t \le t^*$ exists and is optimal. If we can find s and t such that $\phi_t^{M^{II}}(x^i) = \phi_s^{M^{IV}}(x^f)$. Then the total transit time is $t^* = t - s$.

For $M = M^{II}$ we have the system

$$\begin{aligned} \frac{dx_1}{dt} &= -M_2 x_1 + x_2 + x_{np}, \quad & x_1(0) &= x_1^i, \\ \frac{dx_2}{dt} &= M_2 b_2 x_1 - b_2 x_2, & x_2(0) &= x_2^i. \end{aligned} \tag{3.19}$$

We solve $\dot{x} = \mathbf{A}x + (x_{np}, 0)^T$ by variation of parameters:

$$x(t) = e^{t\mathbf{A}} x^i + e^{t\mathbf{A}} \int_0^t e^{-\tau \mathbf{A}} \begin{pmatrix} x_{np} \\ 0 \end{pmatrix} d\tau.$$

where, letting $a = (b_2 + M_2)$ the fundamental matrix solution is

$$e^{t\mathbf{A}} = \frac{1}{a} \begin{pmatrix} b + e^{-at} M & 1 - e^{-at} \\ bM - be^{-at} M & be^{-at} + M \end{pmatrix}. \tag{3.20}$$

We have

$$e^{t\mathbf{A}} \int_0^t e^{-\tau \mathbf{A}} \begin{pmatrix} x_{np} \\ 0 \end{pmatrix} d\tau = a^{-2} \begin{pmatrix} \left(M - e^{-at} M + abt\right) x_{np} \\ be^{-at} M \left(1 + e^{at}(at - 1)\right) x_{np} \end{pmatrix}$$

Therefore, the complete solution, after simplification is

$$\begin{aligned} x_1(t) &= a^{-2}\big(M x_{np} + a(x_2^i + b_2(x_1^i + t x_{np})) + (aM x_1^i - a x_2^i - M x_{np}) e^{-at}\big), \\ x_2(t) &= a^{-2}\big(M(-b_2 x_{np} + a(x_2^i + b_2(x_1^i + t x_{np}))) + b_2(a(-M x_1^i + x_2^i) + M x_{np}) e^{-at}\big). \end{aligned} \tag{3.21}$$

Next, for $M = M^{IV}$, which is the solution along σ^{IV}, we have (noting that we may solve backwards from x^f).

$$\begin{aligned} \frac{dy_1}{ds} &= y_2 + x_{np}, \quad & y_1(0) &= x_1^f, \\ \frac{dy_2}{ds} &= -b_2 y_2, & y_2(0) &= x_2^f. \end{aligned} \tag{3.22}$$

By direct integration, the solution is

$$y_1(s) = x_{np}s + \frac{x_2^f}{b_2}(1 - e^{-b_2 s}) + x_1^f$$

$$y_2(s) = x_2^f e^{-b_2 s}.$$

Now, we solve $x_1(t) = y_1(s)$ and $x_2(t) = y_2(s)$ for s and t:

$$\begin{aligned} a^{-2}\big(Mx_{np} + a(x_2^i + b_2(x_1^i + tx_{np})) + (aMx_1^i - ax_2^i - Mx_{np})e^{-at}\big) \\ = x_{np}s + \frac{x_2^f}{b_2}(1 - e^{-b_2 s}) + x_1^f, \end{aligned} \tag{3.23}$$

$$\begin{aligned} a^{-2}\big(M(-b_2 x_{np} + a(x_2^i + b_2(x_1^i + tx_{np}))) + b_2(a(-Mx_1^i + x_2^i) + Mx_{np})e^{-at}\big) \\ = x_2^f e^{-b_2 s}. \end{aligned} \tag{3.24}$$

Solving for $e^{-b_2 s}$ in equation (3.24) as a function of t we get

$$e^{-b_2 s} = (x_2^f a^2)^{-1}\big(M(-b_2 x_{np} + a(x_2^i + b_2(x_1^i + tx_{np}))) + b_2(a(-Mx_1^i + x_2^i) + Mx_{np})e^{-at}\big), \tag{3.25}$$

which we can substitute into equation (3.23) and upon simplification we get

$$t^* = t - s = \frac{x_1^f - x_1^i}{x_{np}} + \frac{x_2^f - x_2^i}{b_2 x_{np}}. \tag{3.26}$$

Therefore, if a solution of $x_1(t) = y_1(s)$ and $x_2(t) = y_2(s)$ exists, equation (3.26) is valid. By Lemma 14, this solution exists for all initial points $x^i \in \mathcal{D}$.

Now we address the case where $x^i \in \mathcal{A}$. By Theorem 10, the control M^{IV} for $0 \le t \le \tau$ and M^{IV} for $\tau < t \le t^*$ exists and is optimal. If we can find s and t such that $\phi_t^{M^{IV}}(x^i) = \phi_s^{M^{III}}(x^f)$. Then the total transit time is $t^* = t - s$.

For $M = M^{IV}$ we have the system

$$\begin{aligned} \frac{dx_1}{dt} &= -M_1 x_1 + x_2 + x_{np}, \quad & x_1(0) &= x_1^i, \\ \frac{dx_2}{dt} &= -b_2 x_2, & x_2(0) &= x_2^i. \end{aligned} \tag{3.27}$$

Again, we solve $\dot{x} = \mathbf{A}x + (x_{np}, 0)^T$ by variation of parameters. This time the fundamental matrix solution is

$$e^{tA} = \begin{pmatrix} e^{-Mt} & \frac{e^{-bt} - e^{-Mt}}{-b+M} \\ 0 & e^{-bt} \end{pmatrix}$$

and then

$$e^{t\mathbf{A}} \int_0^t e^{-\tau \mathbf{A}} \begin{pmatrix} x_{np} \\ 0 \end{pmatrix} d\tau = \left(\frac{e^{-Mt}\left(-1 + e^{Mt}\right) z}{M}, 0 \right)$$

Therefore the complete solution after simplification is

$$\begin{aligned} x_1(t) &= \frac{e^{-bt} x_2^i}{-b+M} + \frac{x_{np}}{M} + e^{-Mt}\left(x_1^i + \frac{x_2^i}{b-M} - \frac{x_{np}}{M} \right), \\ x_2(t) &= e^{-bt} x_2^i. \end{aligned} \tag{3.28}$$

Using the solution for y from above, as before we must solve $x_1(t) = y_1(s)$ and $x_2(t) = y_2(s)$ for s and t. But $x_2(t) = y_2(t)$ implies

$$e^{-bt} x_2^i = e^{-bs} x_2^f$$

which, upon simplification, gives

$$t - s = \ln(x_2^i / x_2^f).$$

By Lemma 14, this solution exists for all initial points $x^i \in \mathcal{A}$. □

3.4 Conclusions

We have presented an analysis of a multi-solute extension of a previously published general model of cell volume and concentration regulation and we have extended the

local stability result in the case $n = 2$ presented in a previous work to global asymptotic stability in the case $n \geq 2$. Moreover we have given an application of this result in control theory, and provided a complete synthesis of an optimal control in a commonly encountered two solute biological system. Finally, we have demonstrated that for initial points in two special cases, there are explicit and simple formulas that define the total transit time. Although the implementation of an optimal control scheme such as this in the biological setting is dependent on the sensitivity to parameters, as long as it can be verified that the initial point is in one of the defined regions above, this optimal control formulation gives an estimate of the minimal transport time that can be achieved. Because of this, one can determine how much engineering, biophysics, or biology is worth undertaking to achieve more optimal protocols.

Chapter 4

An optimal method for the addition and removal of cryoprotective agents

4.1 Introduction

The economic, scientific and even cultural impact of cryobiology is immense: billions of dollars are invested each year in frozen cells and tissues for use in cell culture transport [12], facilitation of agricultural and human reproduction [130], improvements in human and animal transplantation and transfusion medicine [83], and bioengineering [60]. Arguably more important than cooling and warming rates, the addition and removal of cryoprotective agents (CPAs) to and from cells [45, 72, 73] is a critical and limiting factor in cryopreservation success—current cryopreservation protocols are limited by the inability to safely equilibrate cells with sufficient concentrations of permeating CPAs to cause an intracellular glass to form while cooling. The transport of CPAs across cell membranes is well described by a system of coupled ordinary differential equations and is often limited by the existence of cell-specific volume or concentration constraints [72, 73]. Currently, only heuristic optimizations of CPA addition and removal protocols have been published [45, 72, 73]. Here we show that optimal control theory can be applied to the introduction and subsequent removal of

cryoprotective agents with far reaching implications to the field, and extend the general optimization theory outlined in Chapter 3 by including the natural cell volume and concentration constraints that are encountered in the process of cryoprotective agent addition and removal [12]. Moreover we show that for a large set of parameters, five- to fourty-fold time reductions can be made over classical techniques. We then provide a specific application to human oocytes, reducing the time to equilibrate oocytes with multimolar propylene glycol (PG) by a factor of ten. Because oocytes are sensitive to the exposure time of CPAs [38, 98],this new protocol may facilitate the cryopreservation of this clinically important cell type.

There are two conflicting factors in the development of a CPA addition or removal protocol—the exposure time to multimolal concentrations of CPAs and damaging cell volume excursions (Fig. 4.1)—that point to the existence of an optimal protocol and necessitate an algorithm that provides the optimized CPA addition and removal procedure when the membrane permeability characteristics and the osmotic or volumetric tolerance limits of a specific cell type are known. Often CPAs are added and removed in gradual steps, whose times and concentrations are empirically based [44]. Heuristic arguments for the optimization of CPA addition and removal have also been presented in the literature; for example, one may decrease osmotic stress by varying the CPA concentration continuously [72, 73], producing improved but not optimal protocols.

4.2 Problem

We wish to control the extracellular concentrations of permeating and non-permeating solutes (M_2 and M_1, respectively) such that cells are equilibrated at a goal concentra-

tion in the shortest time while remaining within predefined state-constraints. We will use the solute-solvent transmembrane flux model used in previous chapters and commmonly used in cryobiology [66]. In fact, this model recently was noted to encompass a vary large array of membrane transport phenomena [55]. After simplifying the osmotic pressure and non-dimensionalizing to get an equation $x'(\tau) = x_1(\tau)^{-1} f(x(\tau), M(\tau))$, we time-transform with $\tau = \int_0^t x_1(s)ds$, resulting in a system that is linear in the concentration and the state variables (see Appendix A-1 for a derivation, and Table 4.1 for parameter definitions)[1]:

$$\begin{aligned} \dot{x}_1 &= (M_1 + M_2)x_1 - x_2 + x_{np}, \\ \dot{x}_2 &= b_2(M_2 x_1 - x_2). \end{aligned} \tag{4.1}$$

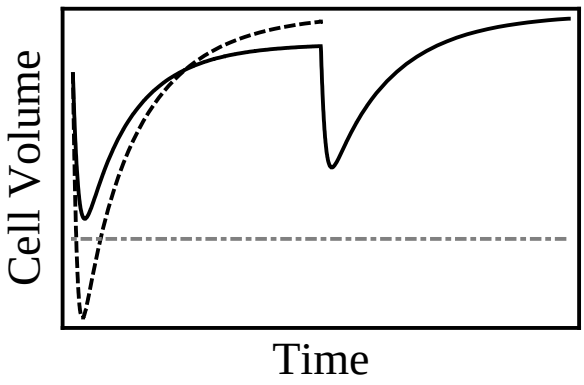

Figure 4.1: Plot of the effects of two different CPA addition protocols. A hypothetical cell is equilibrated with a goal concentration C of a permeating CPA. This cell has a lower limit to which it can contract without damage. If the cell is exposed abruptly to C, the efflux of water causes it to shrink below this limit, causing cell death. Alternatively, if the cell is exposed to $C/2$ and then C, the cell does not exceed the limit, but is exposed to the chemicals for a longer period of time. We wish to find an optimal balance between these two competing effects.

[1] We use the convention $\dot{x} := dx/dt$.

Table 4.1: Definition of parameters

Variable	Characteristic value	Dimensional parameter discription
V_w		Cell water volume
V_w^{iso}		Isosmotic cell water volume
V_b		Osmotically inactive cell volume
s		Intracellular moles of permeating solute
n		Intracellular osmoles of non-permeating solute
m_{iso}	0.3	Isosmotic molality
P_s		Permeating solute permeability
L_p		Water hydraulic conductivity
$\hat{A}$		Cell membrane surface area (assumed constant)
R	0.08205	Gas constant
T		Temperature in Kelvin
$\bar{V}_s$		Partial molar volume of the permeating solute
v^* or v_*		Cell upper and lower volume bounds, respectively
Variable	**Formula**	**Non-dimensional parameter description**
x_1	V_w/V_w^{iso}	Cell water volume
x_2	$s/m_{iso}V_w^{iso}$	Cell permeating solute moles
x_{np}	$n/m_{iso}V_w^{iso}$	Cell non-permeating solute osmoles
x^i or x^f	(x_1, x_2)	Initial or final state values, respectively
M_1	m_n^e/m_{iso}	Extracellular non-permeating solute concentration
M_2	m_s^e/m_{iso}	Extracellular permeating solute concentration
$\bar{M}_i$	$\bar{m}_i^e/m_{iso}$	Maximal solute concentration
b	P_s/L_pRTm^{iso}	Lumped cell permeability parameter
γ	$\bar{V}_s * m_{iso}$	Partial molar volume of the permeating solute
k^*	$v^* - V_b/V_w^i$	Upper or lower cell volume limit, respectively
k_*	$v_* - V_b/V_w^i$	Upper or lower cell volume limit, respectively
t	$\frac{L_p\hat{A}RTm_{iso}}{V_w^{iso}}\bar{t}$	Nondimensional time as a function of real time $\bar{t}$
Variable		**Other parameters**
p_i		Costate variables
$\mathbb{A}$		Admissible control set
τ and s_i		Unitless switching times
ℓ_* and ℓ^*		Lines defined by state constraints
$\phi_t^\lambda(y)$		Solution of equation (4.1) from initial point y at time t. under control $(M_1, M_2) = \lambda$

4.3 Theory

We utilize the unconstrained time-optimal control approach to equation (4.1) outlined in general in Chapter 3, but allow state constraints of the form $\Gamma \cdot \mathbf{x} + k \leq 0$, which may represent water volume, total cell volume, or concentration constraints. The approach can be generalized numerically to nonlinear and multiple state constraints and, due to the high concentrations of permeating and non-permeating solutes required for this theory, generalized to a more appropriate model (see Section A-1 and [36]) using classical numerical optimal control techniques [94]. Here we analytically construct the optimal control with the simple model (4.1) in the most commonly encountered case where there are total cell volume constraints of the form $k_* \leq x_1 + \gamma x_2 \leq k^*$ corresponding to upper and lower osmotic tolerance limits, where the initial and final water volumes are equal, i.e. $x_1^f = x_1^i = x_1^*$, and either $x_2^i = 0$ and $x_2^f = x_2^*$, or $x_2^i = x_2^*$ and $x_2^f = \epsilon$ for ϵ small (e.g. $\epsilon = 0.1$, which corresponds to a $0.1 \times m_{iso} = 0.02$ molal concentration). Finally we let $\gamma = \bar{V}_s m_{iso}$ be the nondimensional molar volume of permeating solute. These two cases correspond to the addition or the removal of CPA, respectively. In the second case, theoretically, one must set $x^f = (x_1^*, \epsilon)$ because the dynamics of the system only allow an asymptotic approach to the x_1-axis. Furthermore, we bound $0 \leq M_1(t) \leq \bar{M}_1$ and $0 \leq M_2(t) \leq M_2$, where $\bar{M}_i$ are maximal physical or practical concentration limits[2], and restrict x^i and x^f so that $x_2^y \leq x_1^y \bar{M}_2$ and $x_{np} \geq x_1^y \bar{M}_1$ (where $y = i$ or f).

Define $\mathbb{A} := [0, \bar{M}_1] \times [0, \bar{M}_2]$ and ϕ_t^λ to be the solution of (4.1) at time t with $\phi_0^\lambda(x) = x$, with control $\lambda = M^j$ defined in Table 4.2. As in Chapter 3, we define

[2]For example, $\bar{M}_1$ may be limited by the salt or sucrose saturation point and $\bar{M}_2$ may be limited by a maximum practical viscosity.

Table 4.2: Definition of controls

Control	$M_1(t)$	$M_2(t)$
M^{II}	0	$\bar{M}_2$
M^{III}	0	0
M^{IV}	$\bar{M}_1$	0

the curves $\sigma^j := \{x \in (\mathbb{R}^+)^2 : x \in \phi_t^{M^j}(x^f), t < 0\}$, for $j = II, III, and IV$, define the time $\tau > 0$ to be the first time that $\phi_\tau \in \sigma^j$, and define the time $t^* > 0$ to be the total time to reach x^f. Recall that the curves σ^j define regions $\mathcal{A}$ and $\mathcal{D}$ in the state space $S = (\mathbb{R}^+)^2$. In this application, $x^i \in \mathcal{D}$ for CPA addition protocols, and $x^i \in \mathcal{A}$ for CPA removal protocols. These conditions must be checked in general, though when $\bar{M}_1$ and $\bar{M}_2$ are large enough, the x^i considered in this chapter are all well within the appropriate regions. In Chapter 3 we synthesized optimal controls based on the Pontryagin Maximum Principle (see Section A-2 and [111]) and proved optimality using a theorem of Boltayanski (see Section A-3 and [18]) but did not show how to handle constraints. For the unconstrained case we can define the optimal CPA addition and removal controls, respectively:

$$M_A(t) = \begin{cases} M^{II} & t \leq \tau \\ M^{III} & \tau < t < t^* \end{cases}, \quad \text{and} \quad M_R(t) = \begin{cases} M^{IV} & t \leq \tau \\ M^{III} & \tau < t < t^* \end{cases}.$$

These controls are optimal, but come at the cost of possibly excessive volume excursions. We wish now to optimize in the presence of constraints, which define lines in the state space $\ell_* := \{(x_1, x_2) \in (\mathbb{R}^+)^2 : \gamma x_2 = -x_1 + k_*\}$ and $\ell^* := \{(x_1, x_2) \in (\mathbb{R}^+)^2 : \gamma x_2 = -x_1 + k^*\}$, corresponding to the lower and uppser volume constraints, respectively. It turns out that in practice, if $\bar{M}_1$ and $\bar{M}_2$ are large enough, it is sufficient to only use constraints of the form $k_* \leq x_1 + \gamma x_2$ for both CPA addition

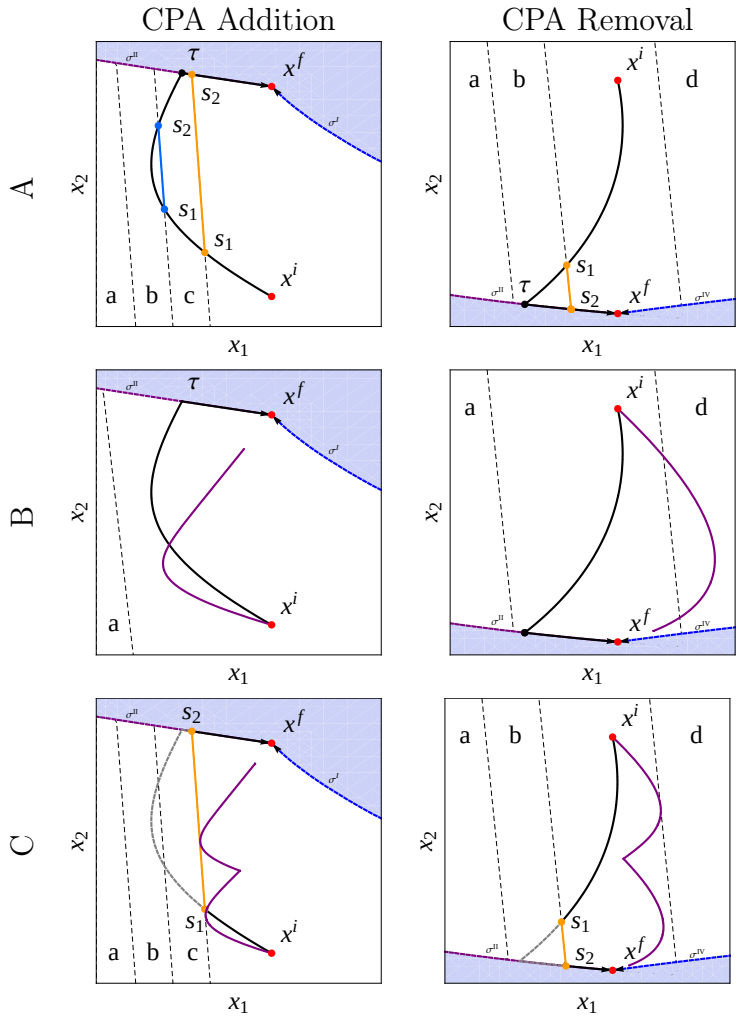

Figure 4.2: State trajectories for optimal and non-optimal controls at several levels of constraints for CPA addition and removal. Black, orange, and purple lines indicate unconstrained optimal, constrained optimal, and standard controls, respectively. Regions a,b, c, and d indicate four levels of state constraints. In row A, we show the possible configurations for the optimal controls. Switching times are given by s_1, s_2, and τ. The blue line indicates the optimal control with a different constraint. In row B we show both the optimal and standard unconstrained controls. In row C we show both the optimal and standard constrained controls. Note that in the CPA Removal case, the standard control uses the constraint bounding region d, and the optimal control uses the constraint bounding region b. Comparisons of equilibration times can be found in Table 4.5

and removal protocols[3]. In both cases we will define at most three times $s_1 < s_2$ and τ corresponding to the switching times for control schemes. There are three possibilities for the dynamics of the optimal control problem: (1) the state constraint is inactive and the "bang-bang" optimal control outlined above is optimal; (2) the state constraint is active but $\phi_t^\lambda(x^f) \notin \ell_*$ for all $t \leq \tau - t^*$; (3) the state constraint is active and $\phi_t^\lambda(x^f) \in \ell_*$ for some $t \leq \tau - t^*$. These cases are shown in Fig. (4.2). Because of the above argument, we can see that in cases (2) and (3) there are times s_1 and s_2 where the unconstrained optimal path intersects the constraint line. The constrained Pontryagin Maximum Principal states that the optimal control for $t \in (s_1, s_2)$ is given by the maximizer, $M(t) \in \mathbb{A}$, of

$$\max_{M \in \mathbb{A}} \{H(x^*, p^*, m) : c(x, m) = 0\},$$

where

$$\begin{aligned} c(x, m) &= ((1, \gamma)) \cdot (A(M)x + x_{np}e_1) \\ &= -(M_1 + M_2)x_1 + x_2 + x_{np} + \gamma(M_2 b_2 x_1 + b_2 x_2) \\ &= x_1(-(M_1 + M_2) + M_2 b_2 \gamma) + x_2(b_2\gamma + 1) + x_{np}. \end{aligned}$$

We also have the costate equation for $t \in (s_1, s_2)$:

$$\dot{p}(t) = -\nabla_x H(x, p, M) + \lambda \nabla_x c(x, M).$$

Moreover, from the theorem we must have the jump conditions

$$\lim_{t \to s_1^+} p(t) = \lim_{t \to s_1^-} p(t)$$

[3]In the CPA addition case, we only require $\bar{M}_2 > \frac{x_{np}}{x_1^i}$. In the CPA removal case, if $\bar{M}_1 > \frac{x_{np} + x_2^f}{x_1^f}$, $\dot{x}_1 < 0$ for all t until $x_1 = x_{np}/M_1$, and thus for all $t > 0$, $\phi_t^{M^{III}}(x^i) \cap \ell^* = \emptyset$. If $\bar{M}_1 < \frac{x_{np} + x_2^f}{x_1^f}$, it is more of a challenge to determine in what cases $\phi_t^{M^{III}}(x^i) \cap \ell^* \neq \emptyset$. Interestingly, for ϵ small and $\bar{M}_1 > x_{np}/x_1^i$, it is easy to show that there is a $t > 0$ such that $\phi_t^{M^{III}}(x^i) \cap \ell_* \neq \emptyset$.

and

$$\lim_{t\to s_2^+} p(t) = \lim_{t\to s_2^-} p(t) + \lambda^*(t)\nabla_x c(x^*(t), M(t)).$$

Because of these jump conditions, we are able to deduce the optimal controls. For $t \notin (s_1, s_2)$ the controls are the same as for the unconstrained system. For $t \in (s_1, s_2)$, we must maximize $H(x, p, M)$ with $\gamma x_2 = -x_1 + k_*$, which is equivalent to maximizing

$$\max_{M_1, M_2} \{-M_1 p_1(k_* - \gamma x_2) + M_2(b_2 p_2 - p_1)(k_* - \gamma x_2)\}. \tag{4.2}$$

We now proceed first in the CPA addition and then the CPA removal cases.

Defining the CPA addition control while on the constraint

In the CPA addition case, from Chapter 3, $p_1(s_1) > 0$ and $p_2(s_1) > p_1(s_1)/b_2$, so $p_1, p_2 > 0$. Thus, since $k_* - \gamma x_2 > 0$, in order to maximize (4.2) we must choose M_1 as small as possible and M_2 as large as possible to keep the path along $x_1 + \gamma x_2 = k_*$. Thus, if $\bar{M}_2$ is large enough, we may set $M_1 \equiv 0$. Because of this, we can explicitly solve system (4.1) with $\Gamma \cdot x = v_*$ for $M_2(t)$. Since $\Gamma \cdot \dot{x} = 0$, we have $\dot{x}_1 = -\gamma \dot{x}_2$, or

$$-M_2 x_1 + x_2 + x_{np} = -\gamma(M_2 b_2 x_1 - b_2 x_2),$$

which we solve for

$$M_2 = \frac{(1 - \gamma b_2)x_2 + x_{np}}{(1 - b_2\gamma)x_1}, \tag{4.3}$$

and substitute this back into the system (4.1) with $M_1 = 0$ to get the system

$$\begin{aligned} \dot{x}_1 &= \gamma b_2 x_{np}/(b_2\gamma - 1), \\ \dot{x}_2 &= b_2 x_{np}/(1 - b_2\gamma), \end{aligned} \tag{4.4}$$

which has obvious solutions

$$x_1(t) = \gamma(t - s_1) b_2 x_{np}/(b_2\gamma - 1) + x_1(s_1)$$

$$x_2(t) = b_2 x_{np}(t - s_1)/(1 - b_2\gamma) + x_2(s_1).$$

utting these solutions into (4.3) and simplifying, we define the constrained optimal CPA addition control:

$$M_2^A(t) = \frac{(1-b_2\gamma)x_2(s_1) + (1+b_2t)x_{np}}{(1-b2\gamma)x_1(s_1) - b_2\gamma x_{np}t}. \tag{4.5}$$

Thus for case (1) we have one switch, τ, for case (2) we have switches $s_1 < s_2 < \tau$, and for case (3) we have switches $s_1 < s_2$. With these switching times we can define the optimal controls in each scheme. For all three cases $M_1(t) \equiv 0$, and in Cases (1–3), we have

$$\begin{array}{ccc} \text{Case (1)} & \text{Case (2)} & \text{Case (3)} \\ M_2(t) = \begin{cases} \bar{M}_2 & t \le \tau \\ 0 & \tau < t < t^* \end{cases}, & \begin{cases} \bar{M}_2, & t \le s_1 \\ M_2^A(t), & s_1 < t < s_2 \\ \bar{M}_2, & s_2 < t < \tau \\ 0, & \tau < t < t^* \end{cases}, & \begin{cases} \bar{M}_2, & t \le s_1 \\ M_2^A(t), & s_1 < t < s_2 \\ 0, & s_2 < t < t^* \end{cases}. \end{array} \tag{4.6}$$

Defining the CPA removal control while on the constraint

In the CPA removal case, from Chapter 3, $p_1(s_1) < 0$ and $p_2(s_1) < p_1(s_1)/b_2$, and in order to maximize Eq. (4.2), we must maximize $M_1(t)$ and minimize $M_2(t)$. Now, if M_1 is large enough, we may set $M_2 \equiv 0$. Because of this we can explicitly solve system (4.1) for $M_1(t)$ as above to get

$$M_1(t) = \frac{x_2(1-\gamma b_2) + x_{np}}{x_1}, \tag{4.7}$$

and upon substituting into the equations (4.1) we get the system

$$\begin{aligned} \dot{x}_1 &= b_2 x_2 \gamma, \\ \dot{x}_2 &= -b_2 x_2, \end{aligned} \tag{4.8}$$

which has obvious solutions $x_1(t) = -\gamma x_2(s_1)e^{-b_2t} + x_1(s_1) + \gamma x_2(s_1)$ and $x_2(t) = x_2(s_1)e^{-b_2t}$. Putting these solutions into (4.3) and simplifying, we define the con-

strained optimal CPA removal control

$$M_1^R(t) = \frac{e^{bt}x_{np} + x_2(s_1) - bx_2(s_1)\gamma}{-x_2(s_1)\gamma + e^{bt}(x_1(s_1) + x_2(s_1)\gamma)}. \tag{4.9}$$

For case (1) we have one switch, τ. For case (2) we have switches $s_1 < s_2 < \tau$, and for case (3) we have switches $s_1 < s_2$. With these switching times we can define the optimal controls in each scheme. For all t hree cases $M_2(t) \equiv 0$, and in Cases (1–3), we have

$$M_1(t) = \begin{array}{c} \text{Case (1)} \\ \left\{ \begin{array}{ll} \bar{M}_1 & t \le \tau \\ 0 & t > \tau \end{array} \right. \end{array}, \quad \begin{array}{c} \text{Case (2)} \\ \left\{ \begin{array}{ll} \bar{M}_1 & t \le s_1 \\ M_1^R(t) & s_1 < t < s_2 \\ \bar{M}_1 & s_2 < t < \tau \\ 0 & t > \tau \end{array} \right. \end{array}, \quad \begin{array}{c} \text{Case (3)} \\ \left\{ \begin{array}{ll} \bar{M}_1 & t \le s_1 \\ M_1^R(t) & s_1 < t < s_2 \\ 0 & t > s_2 \end{array} \right. \end{array}. \tag{4.10}$$

4.4 Discussion

There is nothing new about using the non-permeating solute concentration to facilitate CPA addition and removal ([98]). The novelty of the approach outlined in this chapter comes from the prescription of the optimal extracellular concentration functions. The time improvements gained are dependent on the parameters (see Table 4.5), but because the system (4.1), and in particular parameter b, does not depend on the cell surface area to volume ratio (i.e. $\hat{A}/(V_w + \bar{V}_s s + V_b)$), comparisons may be made across a very diverse range of cell types and temperatures. Examples of b values from the literature for a wide range of cell types are shown in Table 4.3. Because of this, even though the osmotic behavior of cells varies dramatically, we may reduce the parametric analysis to an order of magnitude in b, and instead focus on other parameters such as k^* and k_*.

Table 4.3: Values of dimensionless parameter b for several cell types. All values are published in the appendices of converted parameters in [27] unless noted, and $m_{iso} = 0.3$.

Cell type	CPA	Temperature (°C)	L_p (μm/min/atm)	P_s (μm/min)	b
Mouse Metaphase II oocyte	DMSO	20	0.385	1.228	0.45
Human oocyte	Propylene Glycol	24	0.544	1.624	0.41
Mouse oocyte	DMSO	-3	0.037	0.036	0.15
Human spermatozoa	Glycerol	22	0.79	2.082	0.37
Boar spermatozoa	DMSO	22	0.121	0.974	1.12
Golden hamster pancratic islet	DMSO	22	0.228	1.472	0.90
Endothelial cells	DMSO	22	0.571	2.612	0.63
Keratocytes	DMSO	22	0.495	1.364	0.38
HFL CD34+/ CD38-	DMSO	22	0.24	0.314	0.18
B6 Mouse Embryonic Stem Cells	DMSO	22	0.41	4.59	1.55 [a]
Human red blood cells	Glycerol	22	3.5	5.6	0.22 [b]
Dog red blood cells	DMSO	22	3.2	40.15	1.73 [c]

[a] From [12]

[b] Values converted to 2-parameter form as in [27] from [100]

[c] Values converted to 2-parameter form as in [27] from [75]

"Standard" or "equilibration" CPA addition or removal protocols, as mentioned above, are heuristically and sometimes empirically determined. The basic idea has been that cells are exposed to gradually increasing or decreasing steps, for CPA addition or removal respectively, of CPA concentration M_2^* while M_1 is held fixed. The value of M_1 is out of convenience often set to be the isosmotic concentration $M_1^{iso} = 1$, but some have taken advantage of the osmotic pressures generated by setting $M_1 < 1$ for CPA addition protocols (e.g.[98]), or by setting $M_1 > 1$ for CPA removal protocols (e.g. [73]). These strategies are similar to those employed here, except that the values of M_1 to our knowledge have not been as low as 0 nor as high as $\bar{M}_1$. An interesting decision that must be made for these piecewise constant M_2 protocols is the calculation of optimal concentration steps M_2^* and the duration of each step. Optimal concentration steps have been traditionally calculated using methods similar to those developed in Chapter 2, Section 2.3.1 or in [49].

Because of the nature of system (4.1) (see 3), each step asymptotically approaches its rest point at each step. Therefore, the choice of duration of each step has a dramatic effect on the total time the protocol will take. For CPA addition protocols, it can be seen from Fig. 4.3 that increasing the number of steps will decrease the total time, but also as the number of steps is increased, the stepwise protocol approximates the optimal one. An objective rubric for ending one step and beginning a new one can be obtained by using some function of the state variables and the step's equilibrium point. The rubric that we have adapted is letting the equilibrium time be the first t such that $x_1(t) = \chi \lim_{s\to\infty} x_1(s)$, where $\chi \in (k_*, k^*)$. In Table 4.7, three rubrics—$\chi = 0.9, 0.95, 0.99$—are given for each concentration. As the value of χ is reduced, the

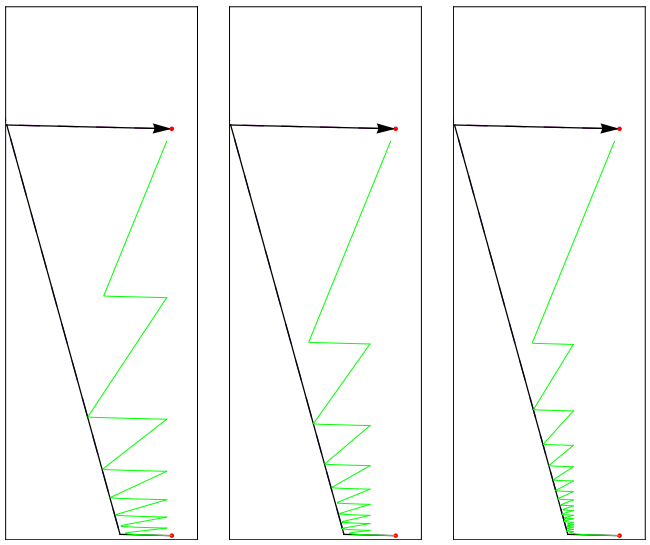

χ	0.97	.0.85	0.73
Steps	7	9	18
Total time	1690	1130	1110

Figure 4.3: Comparison of equilibration state plots for three values of χ. As χ approaches the lower constraint value, the number of steps increases and the total time decreases.

number of steps increases, but the total time is decreased. In fact, as χ approaches k_* the number of steps will dramatically increase and the piecewise constant protocol will begin to approach the optimal control approach. Interestingly, the converse does not occur in the CPA removal protocol. This is because the optimal control drives $x(t)$ to ℓ_*, and the rubric given drives $x(t)$ to ℓ^*.

In Table 4.5 comparisons between optimal and standard protocols are made for representative values of b, k_* and k^*, for a CPA addition and removal protocol. We examined cases at two unitless CPA concentrations: 1 and 10. The correspondence of these concentrations with real-world concentrations is dependent on the value of m_{iso}, but at the characteristic value $m_{iso} = 0.3$ defined in Table 4.1, the unitless concentrations correspond to 0.3 and 3 molal CPA concentrations. Nominal x^i and

Table 4.4: Relative time improvement as a function of m_{iso}. For all cases $x_2^i = 0$, $x_2^f = 10$, $b = 0.1$, and $k_* = 0.7$. The corresponding CPA molality and the total equilibration steps needed are also presented.

m_{iso}	Corresponding CPA molality	t^T	t^*	t^T/t^*	Steps
0.3	3	492	59.0	8.34	6
0.45	4.5	786	80.2	9.8	7
0.6	6	963	95.8	10.1	7
0.9	9	1289	110	11.7	7

x^f were therefore set at $(1, 0)$ and $(1, 1)$ or $(1, 10)$ for CPA addition, and $(1, 1)$ or $(1, 10)$ and $(1, 0.1)$ for CPA removal. To convert these values to "real" concentrations, recall $m_2^e = m_{iso}x_2/x_1$. We are unable to draw direct conclusions about scaling concentration with m_{iso} because $\gamma = m_{iso}\bar{V}_s$ and thus the slope of ℓ^* and ℓ_* will be affected. In Table 4.4 we fix $x_2^i = 0$, $x_2^f = 10$, $b = 0.1$, and $k_* = 0.7$, and look at changing values of m_{iso}. These values of m_{iso} then translate into higher CPA concentrations. We can see that the non-optimal times scale nearly linearly, and thus, the relative time improvements are nearly the same, with a slight increase as m_{iso} is increased.

It is interesting to note that for CPA removal protocols, the location of both volume constraints is important, as opposed to just the upper constraint in standard cryobiological protocols. In fact, for certain combinations of parameters, the upper constraint is not used at all. Because the upper constraint often has a definite physical description—it is the limit to which the cell can swell without lysing—it is theoretically more desirable to avoid this limit than the lower one.

The optimality of the protocols depends on the magnitude of $\bar{M}_1$ and $\bar{M}_2$. In

Table 4.5: Relative time improvement of the optimized protocols (with total time t^*) over standard protocols (with total time t^T) for a range of unitless parameters and both CPA addition and removal schemes. The number of required equilibrium (standard) steps is also given. In the $x_2^f = 1$ and $x_2^i = 1$ cases characteristic maximal concentrations were chosen to be 10 and 10 and in the $x_2^f = 10$ and $x_2^i = 10$ cases characteristic maximal concentrations were chosen to be 20 and 20, both for $\bar{M}_1$ and $\bar{M}_2$, respectively. CPA addition equilibrium steps were determined by calculating the smallest CPA concentration M_2^* such that $x_1 + \gamma x_2 = k_*$, and then following the solution until $x_1 = 0.95x_1^i$, at which point a new M_2^* was calculated. CPA removal equilibrium steps were determined by calculating the largest CPA concentration M_2^* such that $x_1 + \gamma x_2 = k^*$, and then following the solution until $x_1 = 1.03x_1^i$, at which point a new M_2^* was calculated, except for the last step, when the solution was followed until $x_1 = 1.01x_1^i$. Note that for CPA removal, the optimal transit time does not depend on k^*. Plots of the state space for these cases are shown in Figures 4.4 and 4.5.

Addition of CPA, $x_2^f = 1$						Removal of CPAs, $x_2^i = 1$						
b	k_*	t^T	t^*	t^T/t^*	Steps	b	k_*	k^*	t^T	t^*	t^T/t^*	Steps
0.1	0.9	105.9	8.9	11.9	8	0.1	0.7	1.1	147.5	15.97	9.2	12
0.1	0.7	56.4	6.9	8.2	2	0.1	0.7	1.3	88.9	15.97	5.6	3
0.1	0.5	38.2	5.0	7.7	1	0.1	0.7	1.5	75.1	15.97	4.7	2
1	0.9	10.1	0.89	11.4	4	1	0.7	1.1	14.9	1.64	9.1	5
1	0.7	4.9	0.71	6.8	1	1	0.7	1.3	9.1	1.64	5.5	2
1	0.5	4.9	0.56	8.6	1	1	0.7	1.5	6.2	1.64	3.8	1
Addition of CPA, $x_2^f = 10$						Removal of CPAs, $x_2^i = 10$						
b	k_*	t^T	t^*	t^T/t^*	Steps	b	k_*	k^*	t^T	t^*	t^T/t^*	Steps
0.1	0.9	859	79.0	10.9	21	0.1	0.7	1.3	1100	30.0	36.7	17
0.1	0.7	492	59.0	8.33	6	0.1	0.7	1.5	713	30.0	23.7	8
0.1	0.5	399	39.0	10.24	4	0.1	0.7	1.7	569	30.0	18.9	5
1	0.9	84.5	7.86	10.8	14	1	0.7	1.3	107.	3.07	34.9	13
1	0.7	46.5	5.83	7.98	4	1	0.7	1.5	69.9	3.07	22.8	6
1	0.5	40.9	3.80	10.8	3	1	0.7	1.7	55.5	3.07	18.1	4

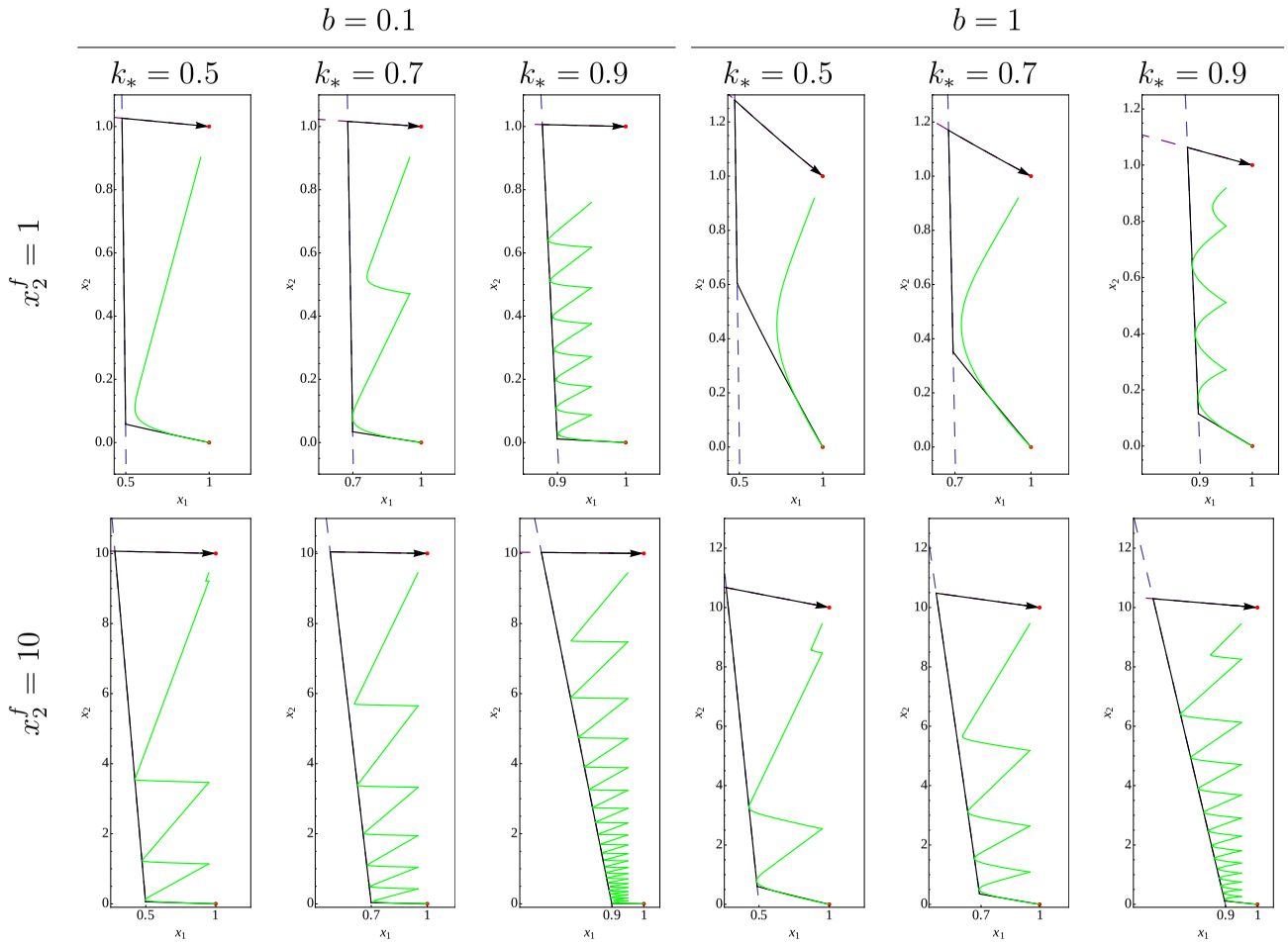

Figure 4.4: CPA addition state plots for several parameter values and two end points. Times, switching rubrics, and relative improvements are given in Table 4.5, and b values for a variety of cell types are given in Table 4.3. As the state constraints are increased from 0.5 to 0.9, the number of steps required for a traditional approach increases, making implementation difficult. At the higher b value, the relative permeability to M_2 is increased, and therefore fewer steps are needed.

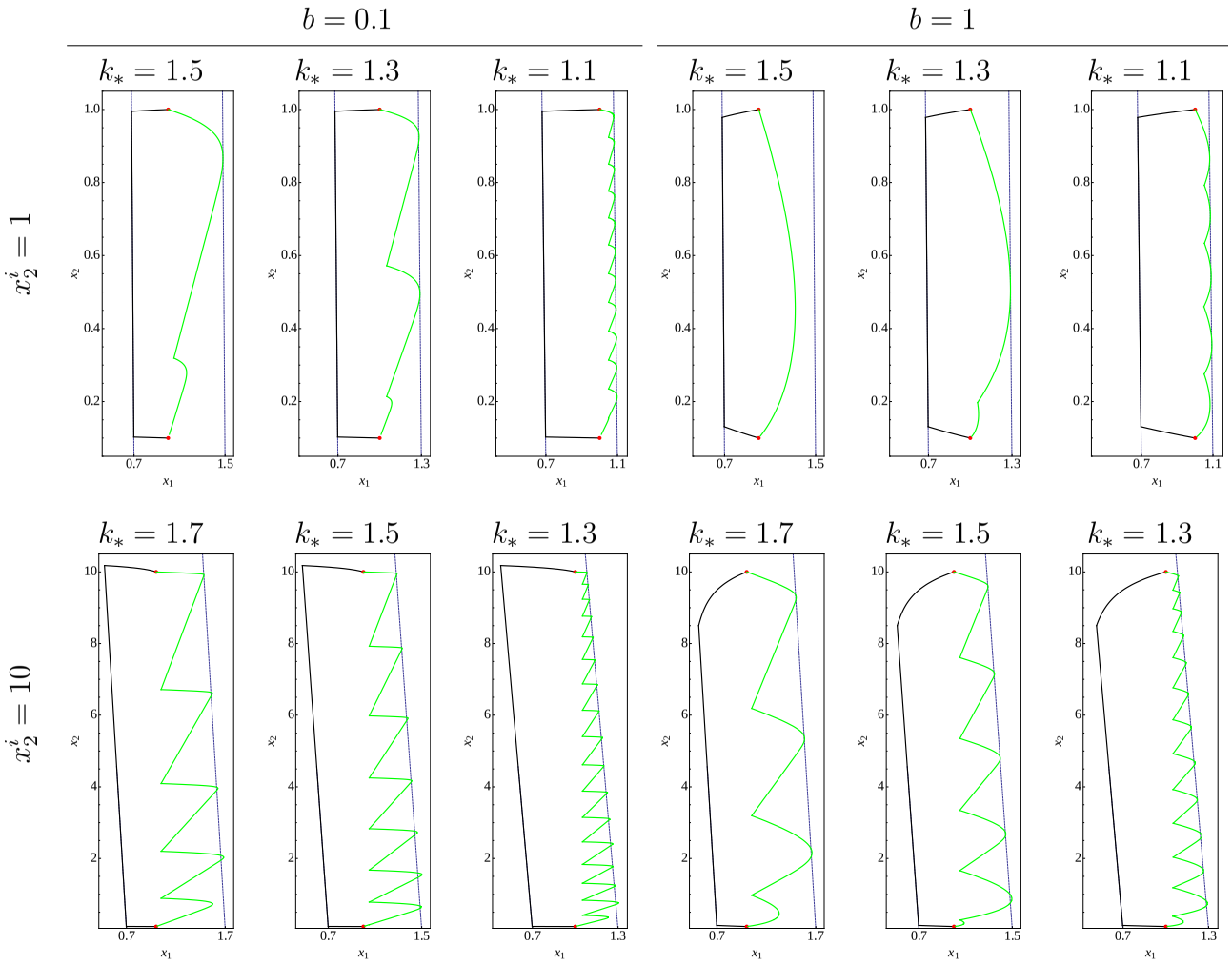

Figure 4.5: CPA removal state plots for several parameter values and two end points. Times, switching rubrics, and relative improvements are given in Table 4.5, and b values for a variety of cell types are given in Table 4.3. The k_* constraint was fixed at 0.7. A k^* value of 1.1 is unusable for the starting point $x_2^i = 10$ because the point x^i is outside of the constraint. As k^* decreased, the total required steps for a traditional approach increased. At the higher b value, the relative permeability to M_2 is increased, and therefore fewer steps are needed.

the M_1 case, $\bar{M}_1$ represents the maximal non-permeating solute molality. This maximum is determined by the makeup of the solution. If the solution only contains salts, then the maximum is most likely limited by a cell's tolerance to very high salt concentrations (< 1.5 molal [92, 90]). On the other hand, if the solution contains salts and, say, sucrose, then the maximum is most likely limited by the viscosity of the sugar solution—because continuous control of concentration is needed, a solution that is amenable to fluid flow is necessary. As in the sucrose example, $\bar{M}_2$ is likely only limited by the viscosity of the solution. This discussion, however, only serves to emphasize the benefit of outlining the complete optimization theory, as it allows these decisions to be made objectively.

4.5 Application of optimal control to human oocyte CPA addition.

There are significant advantages to oocyte cryopreservation. Oocyte cryopreservation allows women who do not have a reproductive partner to preserve their unfertilized gametes. This becomes especially relevant to children or women who may undergo potentially sterilizing iatrogenic proceedures such as chemotherapy [40]. Nearly 17% of couples experience fertility problems, and the use of cryopreserved embryos significantly reduces the costs associated with treatment [46]. The ethical and legal status of cryopreserved embryos, however, is a significant complication. Successful cryopreservation of oocytes would alieviate these problems and would also provide time for infectious disease screening that is not currently possible.

In the United States, the cost of all *in vitro* fertilization (IVF) and intracytoplasmic sperm injection (ICSI) procedures is nearly $500 million per year, but the indirect

costs of the multiple live births associated with multiple embryo transfers is well over $600 million per year [30]. The social and psychological challenges of multiple gestations is also of major concern [41]. One reason multiple embryos are transfered per treatment is that ovarian stimulation and oocyte collection is an invasive and expensive procedure [40]. If oocytes can be sucessfully cryopreserved, multiple oocytes can be harvested and stored until needed. This would allow for the transfer of single embryos, avoiding the ethical problems of cryopreserving embryos and the patient problems of an invasive and expensive procedure. Transferring single embryos would reduce the overall cost of fertility treatments by half in the United States.

To date, no practical and clinically acceptable cryopreservation protocol exists for human oocytes despite these considerable advantages. Much of the failure is attributed to the sensitivity of the meiotic spindle during CPA addition and removal and while cooling from room temperature to subzero temperatures. Partly to avoid this chilling sensitivity, Kuleshova and Lopata [67] have argued that vitrification of embryos and oocytes is often favorable to equilibrium (slow) cooling techniques. O'Neil et al. [99] have demonstrated that some human oocytes can be successfully vitrified, but the concentrations of CPA required exposes cells to extreme osmotic stresses and potential chemical toxicity due to a lengthy addition and removal procedure. Specifically, to load human oocytes with 6 molar propylene glycol required for vitrification, 4 steps are needed using a standard protocol taking at least 122 minutes. On the other hand, the osmotic stress can be managed and the effects of chemical toxicity minimized by using the continuous addition protocols developed in this chapter.

Using published parameter values for human oocytes shown in Table 4.6, we com-

pared optimal controls to classic controls for the addition of multimolar (6, 4.16, and 2.46 molar) propylene glycol, with results shown in Table 4.7. Calculations were made with the assumption that the maximal external CPA concentration was 6.5 molar, corresponding to $M_2 = 41$, and a final concentration difference at the highest x_2^f of only 0.5 molar. This value was chosen because at much higher concentrations the viscosity of the solution may be such that precisely controlling the extracellular CPA concentration may be impossible. The impact of this concentration constraint can be seen by the relative improvements at each goal concentration level. At the highest goal concentration the improvement ratio values range from 4.7 to 11.1, whereas at the lower concentrations the lowest time improvement is 6.5 and the greatest is 19. Nevertheless, even when $\bar{M}_2 - x_2^f/x_1^f$ is small, the time improvements are at least five-fold.

4.6 Problems with application of this model

One potential problem with the optimal protocol outlined here is its dependence on parameters. In theory, the concentrations must switch instantaneously at time τ. This is impossible physically and therefore actually achieving the optimal control may be impossible. However, with continued advances in microfluidic and other related engineering approaches, it is anticipated that it will become practical to utilize these optimal controls in the near future. Moreover, due to natural biological variation, knowledge of cell parameters at the individual cell level may be too imprecise for predicted optimal controls to work. Perhaps the best choice is to use population mean values for parameters, and expect the bulk of the population to achieve an approximation of the goal state. At best some cells may not fully equilibrate at

Table 4.6: Definition of parameters for oocyte propylene glycol addition

Published and Defined Parameters[a]	
Parameter	Value (at $22°C$)
L_p [b]	0.53 μm min^{-1} atm^{-1}
P_s	16.68 μm min^{-1}
V^i	2,650,000 μm^3
V_b	503,500 μm^3
V_w^i	2,146,500 μm^3
A	92,539 μm^2
v_*	0.7 $\times V^i$
T	295.15 K

Calculated (Unitless) Parameters		
Parameter	Equation	Calculated Value
b	P_{s_j}/L_pRTm^{iso}	4.48
x_1^i	V_w^i/V_w^i	1
x_2^i	$x_1^iC_s^i/m^{iso}$	0
x_1^f	V_w^f/V_w^i	1
x_2^f	$x_1^fC_s^f/m^{iso}$	10.34
k_*	$v_* - V_b/V_w^i$	0.51

[a] All values from [102] unless noted.

[b] Water and solute permeability values published in the literature were determined using a different flux model. To account for this, the conversion was made in a similar manner to that described by Chuenkhum and Cui [28].

[c] This is about a 44% (w/w) solution

.

Table 4.7: Comparison of multimolal CPA addition equilibration times for human oocytes. Several standard protocols with total unitless time t^T, are compared with the optimal constrained protocol. Real times are calculated by multiplying unitless times by $L_pARTm^{iso}/V_w^iso = A/V_w^{iso}P_sb_2 = 0.234$. The maximal permeating solute concentration was chosen to be 41, corresponding a 6.5 molar concentration of PG. CPA addition equilibrium steps were determined by calculating the smallest CPA concentration M_2^* such that $x_1 + \gamma x_2 = k_*$, and then following the solution until the switch time equation was satisfied, at which point a new M_2^* was calculated.

x_2^f	Switch time equation	t^T	t^T/t^*	Actual equilibration time (min)	Equilibration steps
36	$x_1(t) = 0.99x_1^i$	522.6	11.12	122.	4
	$x_1(t) = 0.95x_1^i$	281.2	5.98	65.8	4
	$x_1(t) = 0.90x_1^i$	220.2	4.69	51.5	5
20	$x_1(t) = 0.99x_1^i$	374.9	19.4	87.7	4
	$x_1(t) = 0.95x_1^i$	197.3	10.2	46.2	4
	$x_1(t) = 0.90x_1^i$	128.8	6.7	30.1	4
10	$x_1(t) = 0.99x_1^i$	174.9	18.08	40.9	3
	$x_1(t) = 0.95x_1^i$	94.5	9.76	22.1	3
	$x_1(t) = 0.90x_1^i$	62.5	6.45	14.6	3

the goal concentration. At worst, significant portions of the cell population may exceed the constraints, causing damage or death. This latter problem however can be overcome in at least two ways. First, one can build into the model a constraint "buffer" by narrowing the volume constraint limits and in effect allowing for small perturbations from the optimal trajectory to exist without damaging a large portion of the cell population. Second, one can implement a sub-optimal control, where optimal control paths are followed only when theory predicts that the population will remain within the constraints for a broad range of parameters. An example of this is presented in Fig. 4.6. With knowledge of the optimal control, construction of "safer" sub-optimal controls is considerably simplified.

System (4.1) is based on several assumptions (see Appendix A-1). As presented recently by Elmoazzen et al [37], there is no doubt that the linear approximation of osmolality is inappropriate at the high concentrations used in the applications described here. The contention of this chapter is that the theory developed here should serve as a foundation for a numerical analysis using, for example, a more precise relationship between concentration and osmolality. In this case, the governing equation would be

$$\dot{x}_1 = f(x_1, x_2),$$

$$\dot{x}_2 = g(x_1, x_2),$$

where f is either a quadratic or cubic function of n/x_1 and x_2/x_1, and g is either a quadratic or cubic function of x_2/x_1. The complexity of this extension is only significant analytically, and the analysis presented in this chapter will serve as an "exact solution" of a future numerical optimization scheme involving f and g.

Finally, System (4.1) is based on the assumption of perfect stirring inside and

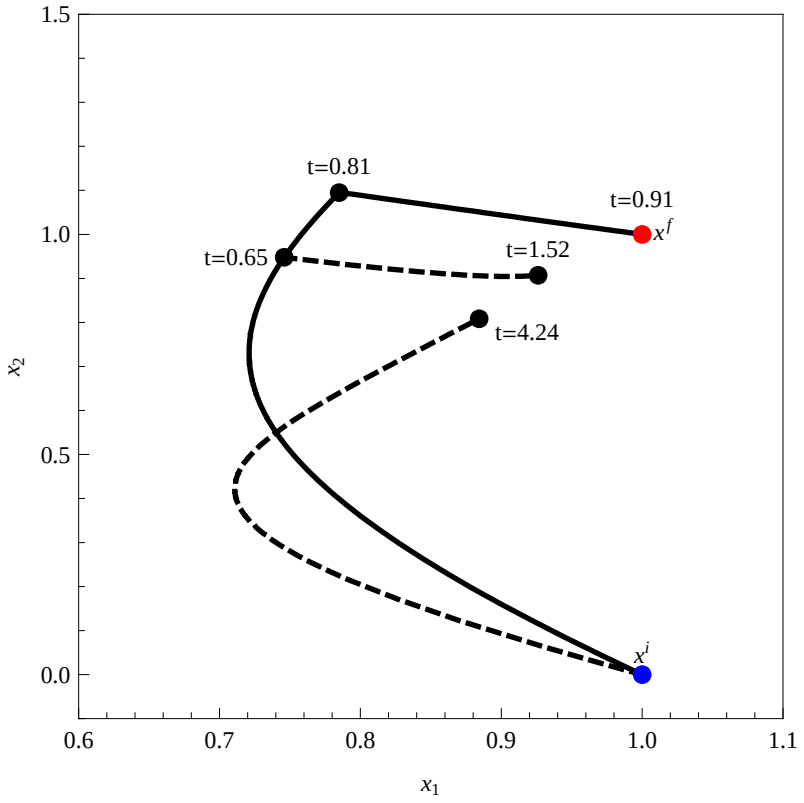

Figure 4.6: Comparison of the standard CPA addition protocol with a predicted optimal and suboptimal protocol where the optimal trajectory is followed for a period of time, and then the traditional approach is followed. End times are given, and the time advantage of even a suboptimal approach is still evident, and the suboptimal approach does not have some of the parameter dependent time sensitivity that the true optimal approach does.

outside of the cell. Because applications of the optimal control to biological systems requires the exposure of cells to varying extracellular fluid envirionments, the appropriateness of this assumption may be called into question. However, we shall see in Chapter 5 that this assumption may be valid in the case of single somatic cells in suspension.

Chapter 5

The impact of diffusion and extracellular velocity fields on cell, tissue, and organ mass transport

5.1 Introduction

The transmembrane flux models for cellular mass transport used in cryobiology are most often a two parameter [57] or a three parameter rate model [64] with the assumption that the only concentration gradient occurs across the cell membrane [2, 7, 62, 88, 109, 123] (see Figure 5.1). However, it has long been known that there exist unstirred and boundary layers around cells that act as a permeation impediment, decreasing the apparent membrane permeability of cells to water and solutes [11, 39]. This reduction is due to the reduction of the transmembrane gradient (Figure 5.1). Thus, models of cellular transport in the literature may be experiment specific and yield phenomenological parameter estimates. In other words, experimental conditions may determine the values of measured permeability.

Measurements of cellular permeability parameters, achieved by fitting ordinary differential equations (ODEs) to volumetric data, fall into one of two categories. In the first, cells are exposed to an abrupt change in extracellular media without subsequent

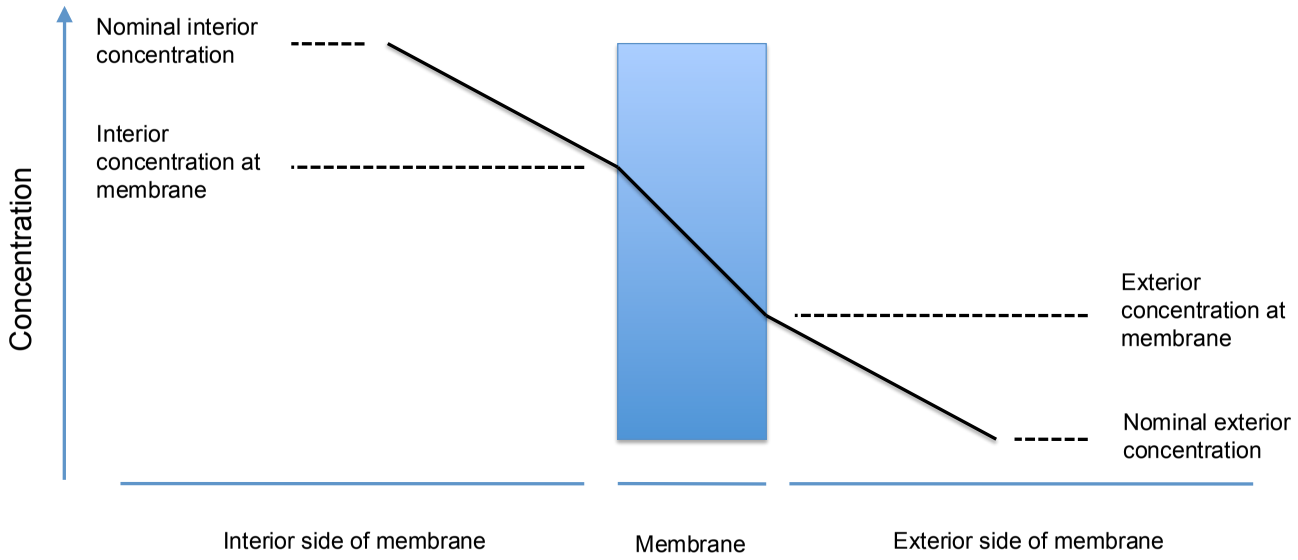

Figure 5.1: Schematic of concentration profiles near a membrane. Transmembrane mass transport is generated solely by the concentration difference at the membrane boundaries. In current cryobiological literature, the nominal concentration is assumed to equal the concentration at the membrane. In this chapter we investigate the nature of the gradient away from the boundary.

mixing [98]. In the second, cells are exposed to an abrupt change in extracellular media and the media is either continuously passed over the cells (e.g. in a diffusion chamber [88]) or cells are exposed to a turbulent environment while measurements are made (e.g. by a Coulter counter [12]). In both cases the resulting volume change is recorded and ODE models are fit to the data to determine permeability parameters (e.g. L_p and P_s from previous chapters). In the first case, the cells may have unstirred diffusion layers next to the membrane that are not disrupted by fluid flow around the cells. In the second case, however, cells may have reduced diffusion layers due to the fluid movement, but advective effects may alter the uniformity of the solute distribution around the cell or tissue. In either case, it is desirable to understand both stirred and unstirred conditions for each cell type because both conditions may exist during cryobiological procedures.

The interest in these phenomena was specifically generated by the analysis of Chapter 3 and Chapter 4 of this thesis. Specifically, in Chapter 4, we outlined a method to optimally introduce or remove CPAs from cells, but these new protocols require continual control of extracellular solute concentrations, a task requiring the perfusion of media over cells along with precise concentration control at the cell boundary, and one that may necessitate accounting for advective and diffusive effects. If one could show that the effects of convection-diffusion are unimportant at the typical single cell level, then the standard solute-solvent transport model and its associated optimal control is sufficient for the CPA addition and removal protocols outlined in Chapter 4. On the other hand, if these phenomena are important—perhaps in certain cases—the applicability of the optimization would be limited, and

new optimal controls would be required.

The behavior of solutes in water is well understood and can be modeled appropriately using the diffusion equation [35]. This model has been applied to membranes, both planar and cellular, and the resulting concentration profiles have been extensively discussed [11, 39]. Additionally, measurements of apparent unstirred layers around biological cells have been taken, revealing that even with the most vigorous stirring these layers persist [11, 121]. These models have only been applied to cells at equilibrium with the cell membrane modeled as a static object. Because the dynamics of fluid transport in cells requires that the cell change volume, we believe that the movement of the membrane within these unstirred layers may be an important effect. Additionally the multimolar gradients generated during CPA addition and removal protocols are much greater than those modeled previously. We are interested in investigating two related but different hypotheses: (1) diffusion significantly affects mass transport in static environments (e.g. with little or no extracellular fluid velocity); (2) convection significantly affects the concentration distribution around cells, tissues and organs in non-static environments.

5.1.1 Characteristic quantities of the system

Other authors in the cryobiological literature have noted that the important quantities when determining whether diffusion plays an important role are the diffusion length scale and the Péclet number [74, 100]. The diffusion length $L_D := \sqrt{4Dt_c}$ is a measure of the length scale at which diffusion acts. If the diffusivity D is small and the characteristic time scale t_c is large, the effect of diffusion can act at a longer distance than if diffusivity is large and the time scale is small. We are most interested in

the ratio of the characteristic length L of the system and this diffusion length, which is determined in the Péclet number: Pé $= 4L^2/L_D^2 = L^2/Dt_c$. If Pé $\gg 1$ gradients may exist. If Pé $\ll 1$ diffusion is dominant and gradients may not exist. The precise characteristic length scale is debatable—one could use the radius, diameter or some multiple of these values, but ultimately this length will approximate the diameter of the cell, tissue or organ. The characteristic time scale is determined by the system biophysics—the transmembrane mass transport occurs on the 10^0 to 10^2 second scales, depending on the surface area to water-volume ratio, relative water and solute permeabilities, and temperature. Interestingly, the surface area to volume ratio, and thus to a certain extent the characteristic time scale, increases linearly with radius, but the Péclet number has the square of length scale in the numerator. Thus for larger cells and tissues, it is natural that Pé > 1. In Table 5.1, we show Péclet numbers for several combinations of lengths and times. At typical single cell scales, the Péclet number is much smaller than unity, especially as time increases. This suggests that at the typical single cell scale, diffusion occurs faster than the cell can react, and there will be little to no diffusion induced gradient. This is an observation made previously [73, 72, 100]. On the other hand, on the oocyte scale where a characteristic time is on the order of 10 seconds, Pé is within an order of magnitude of unity, and the Péclet number is indeterminant, requiring numerical investigation.

In the convection diffusion case, we can rewrite the Péclet number as P $= LV/D$, where V is the characteristic fluid velocity. In this case the Péclet number is the unitless number that indicates whether convection or diffusion are the dominant terms in the convection diffusion equation. Again, if Pé $\ll 1$, then diffusion is the dominant

Table 5.1: Péclet numbers at characteristic time, fluid velocity, and length scales.

	Length Scale			
Time (s)	Typical Cell 10 μm	Oocyte 100 μm	Tissue 10^3 μm	Organ 10^5 μm
1	1.7×10^{-2}	1.7×10^{0}	1.7×10^{2}	1.7×10^{6}
10	1.7×10^{-3}	1.7×10^{-1}	1.7×10^{1}	1.7×10^{5}
100	1.7×10^{-4}	1.7×10^{-2}	1.7×10^{0}	1.7×10^{4}
Velocity (μm/s)				
1	1.7×10^{-3}	1.7×10^{-2}	0.17	17
10	1.7×10^{-2}	1.7×10^{-1}	1.7	170
10^3	1.7	17	170	1.7×10^{4}
10^6	1700	17000	1.7×10^{5}	1.7×10^{7}

term and particles equilibrate with their surroundings faster than they can be "pushed around" by the fluid movement. Alternatively, if Pé $\gg 1$, then advection is the dominating term, meaning that the fluid "pushes" the particles around faster than diffusion can distribute them. From Table 5.1, again at typical single cell scales, unless the characteristic velocity is enormous, one would expect diffusion to dominate, but at oocyte and larger scales advection may play a role in the concentration distribution around the cell, tissue, or organ.

One of the key decisions when choosing a fluid dynamics model is whether the flow under consideration is laminar or turbulent. This decision is helped by analysis of the Reynolds number, $Re := \rho VL/\eta$, where ρ is the mass density of the fluid and η is the dynamic viscosity of the fluid—in this case $\rho = 1000$ kg/m^2 and $\eta = 10^{-3}$ Pa·s since the fluid is water. Thus $Re = 10^6 VL$, where V and L are the fluid velocity and characteristic length with length units in meters, respectively. If the Reynolds number, Re is "small," we may use a laminar flow model. The definition of

Table 5.2: Reynolds numbers at characteristic fluid velocity and length scales.

	Length Scale			
Velocity (μm/s)	Typical Cell 10 μm	Oocyte 100 μm	Tissue 10^3 μm	Organ 10^5 μm
1	10^{-5}	10^{-4}	10^{-2}	10^{1}
10	10^{-4}	10^{-3}	10^{-1}	10^{2}
10^3	10^{-3}	10^{-2}	10^{0}	10^{3}
10^6	10^{-2}	10^{-1}	10^{1}	10^{4}

"small" depends on many conditions, but in most cases for $Re < 2000$, laminar flow is appropriate. From Table 5.2, we see that the Reynolds number is "small" at all cases but the organ size with meter per second fluid velocities. We will thus assume non-turbulent, laminar flow.

5.2 Model Construction

Our basic model is constructed by coupling a solute-solvent transmembrane flux model with a convection-diffusion model for the solute concentrations in the unstirred layer (cf. [11]). For simplicity and continuity from previous chapters, we choose the Jacobs [57] solute-solvent flux model (i.e. system (2.1) from Chapter 2). The model is defined on an open set $\Omega \in \mathbb{R}^3$, with three subregions, D_1, D_2 and D_3 (see Figure 5.2). Region D_1 represents the interior of the cell, D_2 its exterior, and the semipermeable cell membrane is represented by the boundary of D_1 (denoted ∂D_1). Furthermore, we will assume that the shape of D_1 is rotationally invariant or axially symmetric (for example, spherical or cylindrical), which is often the correct geometry for the first approximation of the shape of the cell types that will be investigated. The cell radius is

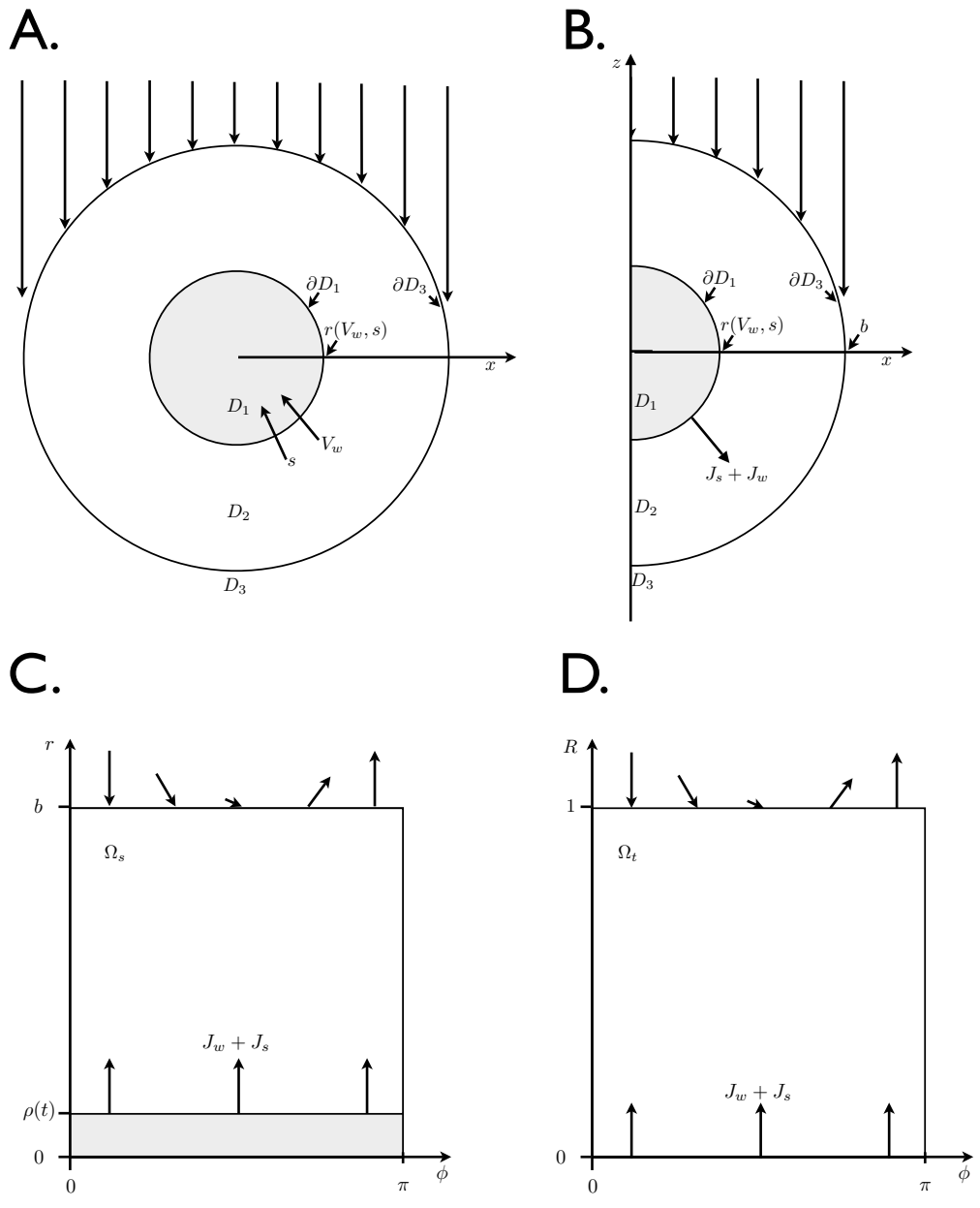

Figure 5.2: A. Diagram of the general system used in modeling. D_1 is the interior of the cell D_2 is the exterior of the cell. D_1 and D_3 are assumed to have perfect mixing (i.e. concentration is invariant with time). B. The system is assumed axially symmetric, and the region of interest is in an annulus around the cell of radius b. The flux $J_s + J_w$ is normal to the cell. C. We transform the space to spherical coordinates with a time dependent cell radius $\rho(t)$. D. Finally we transform the space to spherical like coordinates with a fixed domain.

directly proportional to the intracellular water and solute volumes. Finally, we define $D_3 \subseteq D_2$ to be the stirred extracellular region where we assume no concentration gradients exist.

The state variables are the water volume V_w and the number of moles of permeable solute s from previous chapters, the fluid velocity vector field u, the space and time dependent concentrations C and c of the intracellular and the extracellular permeating solute, respectively, and the concentrations K and k of the intracellular and extracellular non-permeating solute, respectively. Note that $k|_{\partial D_1}$ and $c|_{\partial D_1}$ correspond to M_1 and M_2, respectively, from Chapters 3 and 4. By modeling the transport phenomena associated with a semi-permeable membrane, C and V_w are determined by system (2.1). Additionally, because most cells can be appropriately approximated by a spherical model, it will be advantageous to assume a spherical region D_3. Finally, although we will present the most general model, we will simplify our model to that where the intracellular concentrations C and K are uniform within the cell. In the future we may apply the same theory to the interior of the cell, generating concentration gradients on both sides of the membrane, though applications to tissues and organs requires different models [52].

5.2.1 The basic model

We first present the solute solvent flux model.

Solute-solvent transmembrane flux

Transport models have the general form

$$\begin{aligned} \dot{V_w} &= f(V_w, \Phi|_{\partial D_1}, \lambda, T), \\ \dot{s} &= g(V_w, \Phi|_{\partial D_1}, \lambda, T), \end{aligned} \tag{5.1}$$

where S is the permeating solute volume,

$$\Phi(x,t) = (C(x,t)\ K(x,t)\ c(x,t)\ k(x,t))^T,$$

and λ is a vector of parameters.

We have chosen to work with the Jacobs two parameter model (see Chapter 2 and Appendix A-1), repeated here for convenience:

$$\begin{aligned} \dot{V}_w &= -L_p ART(c + k - C - K)\Big|_{\partial D_1}, \\ \dot{s} &= P_s A(c - C)\Big|_{\partial D_1}, \end{aligned} \tag{5.2}$$

where, as before, s denotes the number of moles of the intracellular permeating solute, A is the area of the cell membrane, R is the gas constant, T is the absolute temperature, L_p is the hydraulic conductivity, and P_s is the solute permeability. Because we assume $C(x,t) = C(t)$ for all $x \in D_1$, the intracellular permeating solute concentration C is measured in moles per water volume V_w; that is, $C = s/V_w$.

The volume V of the cell is given by the sum of the water and solute volumes $V = V_w + \overline{V_s}s + \text{constant}$, and we have the relation $V_w K = \text{constant}$. This system will have initial conditions $V_w(0) = V_{w_0}$ and $C(0) = C_0$, where V_{w_0} is the initial cell (water) volume and C_0 is the initial intracellular permeating solute concentration.

Extracellular fluid flow model

From our discussion of Reynolds numbers above along with the reasonable assumption that the fluid flow is irrotational, it is appropriate to use potential flow; that is, we will assume that the fluid velocity field is the gradient of a potential Ψ. In this case the continuity equation is the Laplace equation given by

$$\Delta\Psi = 0. \tag{5.3}$$

We can recover the fluid velocity by taking the gradient of the solution of (5.3) and using this velocity to solve for the pressure in Euler's steady state fluid equation. Thus, the fluid flow is completely determined by solving the Laplace equation. It remains to define the boundary conditions. In fact for analysis and numerics it is simpler to work solely with the fluid velocity vector u.

The solute volume flux J_s (volume/area/time) leaving the cell is given by the negative right hand side of the $\dot{s}$ term of system (5.2) divided by area A[1]:

$$J_s = \overline{V_s}\frac{\dot{s}^i}{A} = \overline{V_s}P_s(C-c)\Big|_{\partial D_1}, \tag{5.4}$$

where $\overline{V_s}$ is the molecular weight of the solute. The water volume flux J_w is equal to the negative right hand side of the $\dot{V}_w$ term of the Jacobs system divided by the area A:

$$J_w := L_p RT(c+k-C-K)\Big|_{\partial D_1},$$

thus the total fluid velocity vector on the cell boundary will be given by $J_w + J_s$. We define the fluid velocity into the region D_2 to be u_{top} and note that J_w and J_s by definition are in the direction of the normal (e.g. directly away from the cell). We will have space and transmembrane flux dependent Dirichlet conditions for the fluid velocity $u(x) = f(x, J_w, J_s, u_{\text{top}})$ along $x \in \partial D_3$, which we discuss in more detail below. Along ∂D_1 the fluid velocity is simply the sum $J_w + J_s$ in the direction normal to the membrane.

[1]Note that the classic Jacobs model is defined in one dimension, that is the concentration is assumed uniform in the cell and outside of the cell. Here we must consider that the concentrations will not be uniform outside of the cell (we assume for simplicity that the concentration is uniform inside the cell), we will address this later below.

Extracellular diffusion model

The convection-diffusion process for the intracellular and extracellular permeating solute concentration in the unstirred layers inside and outside of the cell is modeled by the mass transport equation and Fick's constitutive law. We let D_c and D_k be the diffusivity of the permeating and non-permeating solutes, respectively,

$$\begin{aligned} c_t &= \epsilon u \cdot \nabla c + D_c \Delta c, \\ k_t &= \epsilon u \cdot \nabla k + D_k \Delta k. \end{aligned} \tag{5.5}$$

System (5.5) is supplemented with initial and boundary conditions. The initial concentration distributions are $c(x,0) = c_0(x)$, and $k(x,0) = k_0(x)$ for $x \in D_2$. The concentrations at the outer boundary of the unstirred layer ∂D_3 are fixed by the concentrations of the bulk solution ($c_b(t)$ and $k_b(t)$); that is, we have the Dirichlet boundary conditions

$$c(x,t) = c_b(t), \qquad k(x,t) = k_b(t),$$

whenever $x \in \overline{D}_3$ and $t \geq 0$.

The concentration model boundary conditions at $x \in \partial D_1$ depend on the fluxes J_w and J_s. At a point with unit normal η, a fluid with concentration c and velocity v has convective solute flux of $c(v \cdot \eta)$, and a diffusive (osmotic) solute flux of $-D\frac{\partial c}{\partial \eta}$, where $\frac{\partial c}{\partial \eta}$ is the normal derivative of c in the direction η, which can be written as $-D(\nabla c \cdot \eta)$. The sum of these solute fluxes gives the total normal solute flux

$$\frac{\partial n}{\partial t} = -D(\nabla C \cdot \eta) + C(v \cdot \eta). \tag{5.6}$$

As discussed above, we note that J_w and J_s by definition are in the direction of the normal. Thus, since $J_s = \frac{\partial n}{\partial t}$, equation (5.6) reduces to

$$-D(\nabla C \cdot \eta) + C J_w = J_s. \tag{5.7}$$

If the solute is non-permeating, then $J_s = 0$. Thus, for the non-permeating solute,

$$-D(\nabla k(x,t)\cdot\eta) + k_0 P_w(c(x,t) - C(t) + k(x,t) - K(t)) = 0$$

for $x \in \partial D_1$, and for the permeating solute:

$$-D(\nabla c(x,t)\cdot\eta) + c_0 P_w(c(x,t) - C(t) + k(x,t) - K(t)) = P_s(c(x,t) - C(t))$$

for $x \in \partial D_1$.

5.2.2 Basic model after a change of coordinates

We define the original (x, y, z) coordinate domain Ω as the axisymmetric annulus around the cell extending from the cell boundary at $\rho(t) = \sqrt{x_r^2 + z_r^2}$, defining ∂D_1, to a predefined outer boundary $b = \sqrt{x_b^2 + z_b^2}$, defining ∂D_3. It is natural to work in spherical coordinates, so we define the domain $\Omega_s = \{(r, \phi) : \rho(t) \leq r \leq b \text{ and } 0 \leq \phi \leq \pi\}$, where $b \in (1, \infty)$, and $\phi \in (0, \pi)$ is the angle away from the z axis. We assume that the fluid enters D_2 parallel to the z-axis. Because we want to work in an unchanging domain, we wish to reparameterize this domain to become Ω_t such that $\Omega_t = \{R, \phi : 0 \leq R \leq 1, \text{ and } 0 \leq \phi \leq \pi\}$, i.e. we map $r = \rho(t)$ to 0 and $r = b$ to 1 (see Fig. 5.2).

Transform function and operators in a new coordinate system

We define two transformation functions and their inverses—$G(x,z)$ from Ω to Ω_s and $H(r,\phi)$ from Ω_s to Ω_t as follows:

$$\begin{aligned} G(x,z) &= \left(\sqrt{x^2+z^2}, \cos^{-1}\left(\frac{z}{\sqrt{x^2+z^2}}\right)\right), \\ G^{-1}(r,\phi) &= \big(r\sin\phi, r\cos\phi\big), \\ H(r,\phi) &= \big(\frac{r-\rho}{b-\rho}, \phi\big), \\ H^{-1}(R,\phi) &= \big((b-\rho)R+\rho, \phi\big). \end{aligned}$$

Next, define $L = H \circ G$ and $L^{-1} = G^{-1} \circ H^{-1}$. These functions are given by

$$L(x,z) = \begin{pmatrix} \frac{\sqrt{x^2+z^2}-\rho}{b-\rho} \\ \cos^{-1}\left(\frac{z}{\sqrt{x^2+z^2}}\right) \end{pmatrix},$$

and

$$L^{-1}(R,\phi) = \begin{pmatrix} (R(b-\rho)+\rho)\sin\phi \\ (R(b-\rho)+\rho)\cos\phi \end{pmatrix}.$$

Note that the principal part of a vector field in Ω, $f(x,z) := (f_1(x,z), f_2(x,z))$, can be translated into the principal part of a vector field Ω_t, $F(R,\phi) := (F_1(R,\phi), F_2(R,\phi))$, by applying the Jacobian of L or L^{-1} as follows:

$$\begin{aligned} F(r,\phi) &= J_L(L^{-1}(R,\phi))f(L^{-1}(R,\phi)) \\ &= J_{L^{-1}}(R,\phi)f(L^{-1}(R,\phi)). \end{aligned}$$

In order for the transformation to be invertible, the Jacobian determinant must be non-singular. We have

$$|J_L(L^{-1}(R,\phi))| = \frac{-1}{(R(b-\rho)+\rho)(b-\rho)}.$$

By assumption, $b \geq R \geq \rho > 0$ and $|J_L(L^{-1}(R,\phi))| \neq 0$. Now, since we have both choices, we may evaluate both to check our algebra. Define $q(R) := R(b-\rho)+\rho$, and note $q'(R) = b - \rho$. Then,

$$J_{L^{-1}} = \begin{pmatrix} q'(R)\sin\phi & q(R)\cos\phi \\ q'(R)\cos\phi & q(R)\sin\phi \end{pmatrix},$$

$$\left(J_{L^{-1}}\right)^{-1} = \begin{pmatrix} \frac{\sin\phi}{q'(R)} & \frac{\cos\phi}{q'(R)} \\ \frac{\cos\phi}{q(R)} & \frac{-\sin\phi}{q(R)} \end{pmatrix},$$

$$J_L(x,z) = \begin{pmatrix} \frac{x}{\sqrt{x^2+z^2}q'(R)} & \frac{z}{\sqrt{x^2+z^2}q'(R)} \\ \frac{z}{x^2+z^2} & -\frac{x}{x^2+z^2} \end{pmatrix},$$

$$J_L(L^{-1}(R,\phi)) = \begin{pmatrix} \frac{\sin\phi}{q'(R)} & \frac{\cos\phi}{q'(R)} \\ \frac{\cos\phi}{q(R)} & -\frac{\sin\phi}{q(R)} \end{pmatrix}.$$

By inspection, $J_L(L^{-1}(R,\phi)) = \left(J_{L^{-1}}\right)^{-1}$ and our algebra is correct. Finally, multiplying on the right by $f(L^{-1}(R,\phi)) = (f_1, f_2)$, we get

$$F(r,\phi) = \begin{pmatrix} \frac{f_2\cos\phi + f_1\sin\phi}{q'(R)} \\ \frac{f_1\cos\phi + f_2\sin\phi}{q(R)} \end{pmatrix}.$$

Gradient and Laplacian in new Domain

The gradient and Laplacian take a new form in the new coordinates. It turns out that the new basis is orthogonal and with knowledge of the Jacobian $J_{L^{-1}}$ we have a shortcut. In fact, in this case the metric tensor is diagonal and we can define positive scaling factors $(h_r(r,\phi), h_\phi(r,\phi))$ that describe the dependence of a unit vector on the position in space [6]:

$$\begin{pmatrix} h_r^2(r,\phi) \\ h_\phi^2(r,\phi) \end{pmatrix} I = \left(J_{L^{-1}}\right)^T J_{L^{-1}},$$

where I is the identity matrix. In our case, then

$$\begin{aligned}\begin{pmatrix} h_r(r,\phi)^2 \\ h_\phi(r,\phi)^2 \end{pmatrix} I &= \left(J_{L^{-1}}\right)^T J_{L^{-1}} \\ &= \begin{pmatrix} (b-\rho)^2 \\ (bR+\rho-R\rho)^2 \end{pmatrix} I \\ &= \begin{pmatrix} q'(R)^2 \\ q(R)^2 \end{pmatrix} I.\end{aligned}$$

The gradient in the new coordinates is $\nabla f = (h_r^{-1} f_r, h_\phi^{-1} f_\phi)$ or

$$\nabla f = \left((q'(R)^{-1}) f_R, q^{-1}(R) f_\phi\right),$$

and the divergence is

$$\mathrm{div} f = \left(\det J_{L^{-1}}\right)^{-1} \left(\frac{\partial}{\partial r}(h_\phi f_1) + \frac{\partial}{\partial \phi}(h_r f_2)\right).$$

In our case

$$\mathrm{div} f = \left(\frac{f_1 + f_{2_\phi}}{q(r)} + \frac{f_{1_r}}{q'(r)}\right).$$

Finally, the Laplacian can be found by taking the divergence of the gradient, and simplifies to

$$\begin{aligned}\Delta f &= \left(\det J_{L^{-1}}\right)^{-1} \left(\frac{\partial}{\partial r}\left(\frac{\left(\det J_{L^{-1}}\right)}{h_r^2}\frac{\partial f}{\partial r}\right) + \frac{\partial}{\partial \phi}\left(\frac{\left(\det J_{L^{-1}}\right)}{h_\phi^2}\frac{\partial f}{\partial \phi}\right)\right) \\ &= \frac{1}{q(r)^2} f_{\phi\phi}(r,\phi) + \frac{1}{q(r)q'(r)} f_R + \frac{1}{q'(r)^2} f_{RR}. \qquad (5.8)\end{aligned}$$

The fluid model in transformed coordinates

For fluid velocity equations, we are using potential flow with fluid velocity potential Ψ. The fluid velocity is given by the gradient, $\nabla\Psi = \left(u^r(r,\phi), u^\phi(r,\phi)\right)$. The continuity equation is $\Delta\Psi = 0$. Because the boundary conditions are all given in terms of fluid velocity, it is natural to simply work with fluid velocities. This has the added

advantage of eliminating the necessary numerical differentiation of the fluid potential as a source of error.

We start with the PDE defined in Ω_t, $\Delta\Psi = 0$.

$$\begin{aligned} 0 &= \Delta\Psi \\ &= \frac{1}{q}\Psi_{\phi\phi} + \frac{1}{qq'}\Psi_R + \frac{1}{q'^2}\Psi_{RR}, \end{aligned}$$

Clearing fractions to remove the R dependence of the first term, we get

$$\Psi_{\phi\phi} + \frac{q}{q'}\Psi_R + \frac{q^2}{q'^2}\Psi_{RR} = 0.$$

Taking the gradient, we get $\nabla\Delta\psi = 0 = (\Delta u^r, \Delta u^\phi) = (q'(\Delta\Psi)_R, q(\Delta\Psi)_\phi)$. Thus, we have

$$\begin{aligned} 0 &= \Delta u^r \\ &= q'(\Psi_{\phi\phi R} + \frac{1}{q'}q'\Psi_R + \frac{1}{q'}q\Psi_{RR} + \frac{1}{q'^2}2qq'\Psi_{RR} + \frac{q^2}{q'^2}\Psi_{RRR}) \\ &= q'u^r_{\phi\phi} + q'u^r + 3qu^r_R + \frac{q^2}{q'}u^r_{RR} \end{aligned}$$

and

$$\begin{aligned} 0 &= \Delta u^\phi \\ &= q(\Psi_{\phi\phi\phi} + \frac{q}{q'}\Psi_{r\phi} + \frac{q^2}{q'^2}\Psi_{r\phi}). \end{aligned}$$

Dividing through by q, we have

$$0 = u^\phi_{\phi\phi} + \frac{q}{q'}u^\phi_R + \frac{q^2}{q'^2}u^\phi_{RR}.$$

The fluid velocity vector along the $R = 0$ boundary is in Ω_s given by $(J_w(t) + J_s(t), 0)$, i.e. the radial component is ϕ-independent. To determine the principal part

of the fluid velocity vector field in Ω_t we have

$$\begin{aligned}[J_{H^{-1}}](J_w(t)+J_s(t),0) &= \begin{pmatrix} (b-\rho)^{-1} & 0 \\ 0 & 1 \end{pmatrix} \begin{pmatrix} J_w(t)+J_s(t) \\ 0 \end{pmatrix}, \\ &= \begin{pmatrix} \frac{J_w(t)+J_s(t)}{b-\rho} \\ 0 \end{pmatrix}.\end{aligned}$$

The fluid velocity vector in Ω due to the external fluid source along the boundary $R=1$ is given by $(0, u^z_{\text{top}}(t))$. Hence, the principal part of the fluid velocity vector field in Ω_t is given by

$$u(1,\phi) = \begin{pmatrix} \frac{u_z^{\text{top}}(t)\cos\phi}{b-\rho} \\ \frac{u_z^{\text{top}}(t)\sin\phi}{b} \end{pmatrix}. \tag{5.9}$$

Finally we rectify the mass balance across both the $R=0$ and $R=1$ boundaries. The total flux across the $R=0$ boundary is given by $\int_{R=0} J_w(t)+J_s(t)\,dS$. The total flux across the $R=1$ boundary due to the exterior flow into Ω_t is $\int_{R=1} u(1,\phi)\,dS$. The flow into the region must equal the flow out of the region, so

$$\int_{R=0} (J_w(t)+J_s(t))\cdot\eta(0,\phi)\,dS + \int_{R=1} u(1,\phi)\cdot\eta(1,\phi)\,dS = 0.$$

Let $A := \int_{R=0} dS$ and $B := \int_{R=1} dS$. Because $J_w(t)+J_s(t)$ is ϕ independent, we can rewrite the above equation as

$$\int_{R=1} \left(\frac{A}{B}(J_w(t)+J_s(t))\cdot\eta(0,\phi) + u(1,\phi)\cdot\eta(1,\phi) \right) dS = 0. \tag{5.10}$$

Since $\eta(0,\phi) = (b-\rho,0)^{\mathrm{T}}$ and $\eta(1,\phi) = (b-\rho,0)$, Eq. (5.10) holds only when

$$\begin{aligned} 0 &= \frac{A}{B}(J_w(t)+J_s(t))\cdot\eta(0,\phi) + u(1,\phi)\cdot\eta(1,\phi) \\ &= \frac{A}{B}(J_w(t)+J_s(t))\cdot\eta(0,\phi) + u(1,\phi)\cdot\eta(1,\phi). \end{aligned}$$

Therefore our $R=1$ boundary condition must be

$$u(1,\phi) = \begin{pmatrix} \frac{(u_z^{\text{top}}(t)\cos\phi)}{b-\rho} - \frac{A}{B}(b-\rho)(J_w(t)+J_s(t)) \\ \frac{u_z^{\text{top}}(t)\sin\phi}{b} \end{pmatrix}.$$

The concentration model in transformed coordinates

We are assuming that the concentrations c and k in Ω are modeled by $c_t = \epsilon u \cdot \nabla c + D\Delta c$ and $k_t = \epsilon u \cdot \nabla k + D\Delta k$, where u is the fluid velocity given by the above PDE, ϵ is a constant of proportionality, and D_c and D_k are the diffusion constants.

Using the conversions outlined above, our permeating solute advection-diffusion PDE in Ω_s is defined by

$$\begin{aligned} c_t &= \epsilon u \cdot \left(\frac{c_R}{q'(r)}, \frac{c_\phi}{q(r)} \right) + \frac{D}{q(r)^2} c_{\phi\phi}(r,\phi) + \frac{D}{q(r)q'(r)} c_R + \frac{D}{q'(r)^2} c_{RR} \\ &= \frac{\epsilon u^r c_R}{q'(r)} + \frac{\epsilon u^\phi c_\phi}{q(r)} + \frac{D}{q(r)^2} c_{\phi\phi}(r,\phi) + \frac{D}{q(r)q'(r)} c_R + \frac{D}{q'(r)^2} c_{RR} \\ &= \frac{\epsilon u^\phi}{q(r)} c_\phi + \left(\frac{\epsilon u^r}{q'(r)} + \frac{D}{q(r)q'(r)} \right) c_R + \frac{D}{q(r)^2} c_{\phi\phi} + \frac{D}{q'(r)^2} c_{RR}, \end{aligned}$$

and the nonpermeating solute advection-diffusion PDE is Ω_s is defined by

$$k_t = \frac{\epsilon u^\phi}{q(r)} k_\phi + \left(\frac{\epsilon u^r}{q'(r)} + \frac{D}{q(r)q'(r)} \right) k_R + \frac{D}{q(r)^2} k_{\phi\phi} + \frac{D}{q'(r)^2} k_{RR}.$$

Boundary conditions On the $R = 1$ boundary, we have assumed $c(1, \phi, t) = f(t)$, where f is some known function of time. On the $\phi = 0$ and $\phi = \pi$ boundaries, because of axial symmetry, we have $\frac{\partial c}{\partial \phi} = 0$. For $x \in \partial D_1 \in \Omega$, i.e. $R = 0$, $\phi \in (0, \pi)$ in Ω_s,

$$-D(\nabla C \cdot \eta) + C J_w = J_s.$$

5.2.3 Nondimensionalization of our model

Finally, it is advantageous to nondimensionalize the complete system.

Solute solvent transmembrane flux equations

First we look at the flux equations, J_w and J_s as they play a role in the boundary conditions for both the fluid and concentration PDEs. We have $J_w = -L_p RT(c + k -$

$C - n/w)$ and $J_s = \overline{V} P_s(c - C)$. Note the units $[J_s] = [J_w] = \frac{\mu \mathrm{m}}{\mathrm{min}}$. Let $L_p = \bar{L}_p L_p^*$, $A = \bar{A} A_{\mathrm{iso}}$, $T = \bar{T} T^*$, $P_s = \bar{P}_s L_p^* R T_0 K_{\mathrm{iso}}$, $J_w = \bar{J}_w u^*$, $J_s = \bar{J}_s u^*$ and all concentrations equal to their unitless value times K_{iso}. Then the water flux equation becomes

$$\begin{aligned} J_w &= -L_p RT(c + k - C - n/w), \\ \bar{J}_w u^* &= -\bar{L}_p L_p^* R \bar{T} T^* K_{\mathrm{iso}}(\bar{c} + \bar{k} - \bar{C} - a_1/\bar{W}), \\ \bar{J}_w &= -\frac{L_p^* R T^* K_{\mathrm{iso}}}{J_w^*} \bar{L}_p \bar{T}(\bar{c} + \bar{k} - \bar{C} - a_1/\bar{W}) \\ &= -a_2 \bar{L}_p \bar{T}(\bar{c} + \bar{k} - \bar{C} - a_1/\bar{W}), \end{aligned}$$

where $a_1 = \frac{n_n^i}{K_{\mathrm{iso}} W_{\mathrm{iso}}}$ and $a_2 = \frac{L_p^* R T^* K_{\mathrm{iso}}}{u^*}$. For the solute flux,

$$\begin{aligned} J_s &= \overline{V_s} P_s(c - C), \\ \bar{J}_s u^* &= \overline{V_s} \bar{P}_s L_p^* R T_0 K_{\mathrm{iso}}^2(\bar{c} - \bar{C}), \\ \bar{J}_s &= a_3 \bar{P}_s(\bar{c} - \bar{C}), \end{aligned}$$

where $a_3 = \frac{\overline{V_s} L_p^* R T_0 K_{\mathrm{iso}}^2}{u^*} = \overline{V_s} K_{\mathrm{iso}} a_2 := a_6 a_2$.

Cell volume and concentration

Next we examine the ODE governing interior concentration and water volume. From some manipulation of system (5.2), we obtain

$$\begin{aligned} \dot{V}_w &= -L_p ART(c + k - C - n/w)|_{\partial D_1}, \\ \dot{C} &= -\frac{P_s A}{V_w}(c - C) - \frac{C}{V_w} L_p ART(c + k - C - n/w)|_{\partial D_1}. \end{aligned}$$

Using the same reparametrizations as before, along with $V_w = \bar{V}_w V_{w_{\mathrm{iso}}}$, $A = \bar{A} A_{\mathrm{iso}}$, and letting $\frac{d\tau}{dt} = \frac{L_p A_{\mathrm{iso}} R T K_{\mathrm{iso}}}{w_{\mathrm{iso}}}$, we get

$$\bar{w}_\tau = \bar{L}_p \bar{A} \bar{T}(\bar{c} + \bar{k} - \bar{C} - \frac{a_1}{\bar{w}})|_{\partial D_1},$$

and

$$\bar{C}_\tau = \frac{\bar{P}_s \bar{A}}{\bar{W}}(\bar{c} - \bar{C}) - \frac{\bar{L}_p \bar{A} \bar{T}}{\bar{W}}(\bar{c} + \bar{k} - \bar{C} - \frac{a_1}{\bar{w}})|_{\partial D_1}.$$

Fluid velocity vector field

In Ω, we have $\Delta u = 0$ for both the x and z parts of the vector field. Thus we note that since $u = \bar{u}\, u^*$ and $x = \bar{x}\, r_{\text{iso}}$, we have that

$$\frac{\partial u}{\partial x} = \frac{\partial \bar{u}}{\partial \bar{x}} \frac{\partial \bar{x}}{\partial x} \frac{\partial u}{\partial \bar{u}} = \frac{\partial \bar{u}}{\partial \bar{x}} \frac{u^*}{r_{\text{iso}}},$$
$$\frac{\partial^2 u}{\partial x^2} = \frac{\partial}{\partial x} \frac{\partial \bar{u}}{\partial \bar{x}} \frac{u^*}{r_{\text{iso}}} = \frac{\partial^2 \bar{u}}{\partial \bar{x}^2} \frac{\partial \bar{x}}{\partial x} \frac{u^*}{r_{\text{iso}}} = \frac{\partial^2 \bar{u}}{\partial \bar{x}^2} \frac{u^*}{r_{\text{iso}}^2},$$

and similar formulas for the z-direction. Because the factors are the same for both the x and z terms, we can divide and retain the original equation without any modifications in our nondimensional space: $\Delta \bar{u} = 0$.

Define u to be the nondimensional fluid velocity in the ϕ direction, and v to be the nondimensional fluid velocity in the R direction:

$$\begin{aligned} 0 &= u_{\phi\phi} + \frac{q(r)}{q'(r)} u_r + \frac{q(r)^2}{q'(r)^2} u_{rr}, \\ 0 &= v_{\phi\phi} + v + \frac{q(r)}{q'(r)} v_r + \frac{q(r)^2}{q'(r)^2} v_{rr}. \end{aligned}$$

Fluid Boundary Conditions

We have the boundary conditions

$$\begin{array}{rclrcl} u(0,\phi) &=& 0, & v(0,\phi) &=& \frac{J_w(t)+J_s(t)}{b-\rho}, \\ u(1,\phi) &=& \frac{u_{\text{top}} \sin\phi}{b}, & v(1,\phi) &=& \frac{u_{\text{top}} \cos\phi}{b-\rho} - \frac{A}{B}(b-\rho)(J_w + J_s), \\ u(R,0) &=& 0, & v_\phi(R,0) &=& 0, \\ u(R,\pi) &=& 0, & v_\phi(R,\pi) &=& 0. \end{array}$$

Using $u = \bar{u}u^*$, $v = \bar{v}u^*$, and our aforemetioned $J_w = \bar{J}_w u^*$ and $J_s = \bar{J}_s u^*$, we get

$$\begin{array}{rclrcl} \bar{u}(0,\phi) &=& 0, & \bar{v}(0,\phi) &=& \frac{\bar{J}_w(t)+\bar{J}_s(t)}{b-\rho}, \\ \bar{u}(1,\phi) &=& \frac{u_{\text{top}}}{u^*} \frac{\sin\phi}{b}, & \bar{v}(1,\phi) &=& \frac{u_{\text{top}}}{u^*} \frac{\cos\phi}{b-\rho} - \frac{A}{B}(b-\rho)(\bar{J}_w + \bar{J}_s), \\ \bar{u}(R,0) &=& 0, & \bar{v}_\phi(R,0) &=& 0, \\ \bar{u}(R,\pi) &=& 0, & \bar{v}_\phi(R,\pi) &=& 0. \end{array}$$

Permeating and non-permeating solute concentration

Finally, we have the system $c_t = \epsilon u \cdot \nabla c + D\Delta c$ on Ω. The same approach will apply for both the permeating and non-permeating concentration equations, with the exception of different boundary conditions. Using a similar approach as above and noting that $c = \bar{c}K_{\text{iso}}$, we see that

$$\frac{\partial c}{\partial x} = \frac{K_{\text{iso}}}{r_{\text{iso}}}\frac{\partial \bar{c}}{\partial \bar{x}}, \quad \frac{\partial^2 c}{\partial x^2} = \frac{K_{\text{iso}}}{r_{\text{iso}}^2}\frac{\partial^2 \bar{c}}{\partial \bar{x}^2},$$
$$\frac{\partial c}{\partial z} = \frac{K_{\text{iso}}}{r_{\text{iso}}}\frac{\partial \bar{c}}{\partial \bar{z}}, \quad \frac{\partial^2 c}{\partial z^2} = \frac{K_{\text{iso}}}{r_{\text{iso}}^2}\frac{\partial^2 \bar{c}}{\partial \bar{z}^2}.$$

Then our PDE is $\bar{c}_s K_{\text{iso}}\alpha = \frac{\epsilon u_{\text{top}} K_{\text{iso}}}{r_{\text{iso}}}\bar{u}\cdot\bar{\nabla}\bar{c} + \frac{DK_{\text{iso}}}{r_{\text{iso}}^2}\bar{\Delta}\bar{c}$. Dividing and defining

$$\epsilon^* := \frac{\epsilon u_{\text{top}} W_{\text{iso}}}{r_{\text{iso}} L_p A_{\text{iso}} RTK_{\text{iso}}}$$

and

$$D^* := \frac{D u_{\text{top}} W_{\text{iso}}}{r_{\text{iso}}^2 L_p A_{\text{iso}} RTK_{\text{iso}}},$$

we get

$$\bar{c}_s = \epsilon^* \bar{u}\cdot\bar{\nabla}\bar{c} + D^*\bar{\Delta}\bar{c}$$

on Ω_s; and renaming everything without bars, we get

$$c_s = \epsilon^* u \cdot \nabla c + D^*\Delta c.$$

At this point we can proceed as before, and the reparametrized equations will be (again with no "barred" variables),

$$c_s = \frac{\epsilon^* u}{q(r)}c_\phi + \left(\frac{\epsilon^* v}{q'(r)} + \frac{D^*}{q(r)q'(r)}\right)c_r + \frac{D^*}{q(r)^2}c_{\phi\phi} + \frac{D^*}{q'(r)^2}c_{rr}.$$

Finally, for the nondimensional boundary conditions we have the Dirichlet condition at $R = 1$, $c(1, \phi, t) = f(t)$, where f is the time-dependent nondimensional external concentration, the Neumann condition at $\phi = 0$ and $\phi = \pi$, $c_\phi(r, 0, t) = c_\phi(r, \pi, t) = 0$, and the Robin type boundary condition at $R = 0$, $-D^{**}c_r + a_5 c J_w = J_s$, where $D^{**} = \frac{D}{r_{\text{iso}} K_{\text{iso}} L_p^* RT_0}$, $a_5 = \frac{u_{\text{top}}}{L_p^* RT_0 K_{\text{iso}}} = 1/a_2$.

It is interesting to note that except for a_1, all constants are either multiples or inverses of a_2. Thus, letting $a_6 = K_{\text{iso}}\overline{V}$, we have

$$a_1 = \frac{n_n^i}{K_{\text{iso}} W_{\text{iso}}}, \quad a_2 = L_p^* RT_0 K_{\text{iso}}/u_{\text{top}}, \quad a_3 = a_6 a_2, \quad a_4 = (a_6 a_2)^{-1}, \quad a_5 = a_2^{-1}.$$

5.2.4 Exact solutions of the fluid and concentration models

It turns out that we can solve the fluid model in general exactly in Ω_s. This proves extremely useful in both analysis and numerical simulations. We may also solve the concentration model in a special case. This allows accurate testing of the independent parts of the numerical scheme. The derivation of these solutions is given in Appendix A-5.

5.3 Numerical analysis

Although we are able to find an exact solution for the fluid model, a general exact solution of the concentration model is unlikely to exist. Therefore we must pursue a numerical scheme to approximate the solution of the PDE system in Ω. Because we have transformed the state space to a rectangle, the simplest and fastest numerical integration scheme is the finite difference method. Without this transformation much work must be done to use finite differences on curved and changing boundaries (see Appendix A-6). There are several different finite difference schemes for parabolic dif-

ferential equations, but we will use the second order implicit Crank-Nicolson method, which utilizes a centered difference method for spatial differentials, and a "trapezoidal" method for temporal differentials. This method has the advantage of being unconditionally stable, meaning that we do not have to worry about the relative spatial and temporal step sizes.

The numerical method uses the mean concentration around the cell and Euler integration to calculate the intracellular water volume V_w and concentration C. The original transmembrane flux model assumes uniform flux and concentration along the membrane. We either need to develop a different flux model, or assume that the flux is uniform along the membrane and is generated by the mean concentration along the boundary. The first would be fairly simple. For example the water flux at any given point along the membrane is $J_w = f(c, k, C, K)|_{R=0}$, for some function f. Then the total water volume flux is $\int_{R=0} J_w \, dS$. We can then either be more precise and suppose that the membrane is a locally moving object, or suppose that the membrane retains its spherical shape and moves as a function of total volume flux. We use the latter calculation and assume a mean concentration along the cell boundary. Because we assume the intracellular concentration is uniform, the local and mean concentration methods are, in fact, the same.

The numerical method depends on several key arbitrary and unknown parameters. The first and most important is b, the size of the domain where diffusion takes place. The parameter b should be some multiple of the cell radius, but it is unclear physically what this multiple should be. The second and much less influential parameter is the intramembrane diffusion constant. Here we simply choose the same diffusion constant

as through water, but this potentially needs refinement. The numerical method is given in Fig. 5.3. Note that the "bottom" ($R = 0$) points are calculated from the Robin boundary condition, and are a function of the other points. This technique is similar to the following example: If we have a Dirichlet condition, for points next to the boundary we may either build the known values into the difference scheme for these cases, or we may add extra (identity) equations for the points *on the boundary*. The downside to the latter method is that extra equations are added, though these equations do not significantly affect the solvability of the linear system of equations generated by the difference method, as they only contribute points along the main diagonal. For a Neumann boundary condition, one is generally not interested in the value of the point at the boundary, and thus builds the derivative into the centered difference method for points next to but not on the boundary. One could do this as well for the Robin boundary condition as well, using the Robin condition to solve for the concentration next to but not on the boundary, except that we are specifically interested in the value of the concentration at the boundary. In this case, we simply add the relationship as another set of equations that must be satisfied in order for the system to be valid. In particular for the points such that $R = 0$, we use a third order left hand numeric method: Define points $r_i = i\,dr + r_0$, where r_0 is a point on the boundary and dr is the step size between the r_i, and associate with each r_i a concentration c_i. Then with a Robin boundary equation $D^* c_r + a^* J_w c_0 = J_s$, we are interested in a high order accuracy left-hand finite difference approximation for c_r. We use

$$\frac{\partial c}{\partial r}(r_0) = \frac{1}{dr}\left(\frac{25}{12}c_0 - 4c_1 + 3c_2 - \frac{4}{3}c_3 + \frac{1}{4}c_4\right).$$

This equation was derived using the techniques developed in Appendix A-6. Thus the difference equation for points along the $R = 0$ boundary will be

$$D^* \frac{1}{dr} \left(\frac{25}{12} c_0 - 4c_1 + 3c_2 - \frac{4}{3} c_3 + \frac{1}{4} c_4 \right) + a^* J_w c_0 = J_s,$$

which we can solve for c_0.

5.4 Results

It is a challenge to quantify the results of our numerical code in a format that provides objective analysis. Instead we may by inspection compare results of various numerical experiments.

In Figs. 5.4, 5.5, and 5.6, we have plots of total cell volume using the perfect stirring model (thick dashed gray lines), and the newer model (solid line) outlined in this chapter with $u_{top} = 10\mu$m/min. The mean concentration of permeating solutes at the boundary is shown by the thin dashed line. In Figs. 5.4, 5.5, and 5.6 we set the relative size of the annulus around the parameter $\bar{b} = 2, 4, 10$, respectively. In each figure, we present three orders of magnitude for the relative permeability $\bar{P}_s$, and four orders of magnitude for the initial radius r_0 (where $r_0 = 10^j/2$, $j = 1, 2, 3, 4$, for typical "cell," "oocyte," "tissue," and "organ" sizes, respectively). Because u_{top} is fixed, we present two Péclet numbers for each initial radius size, recalling that we defined the characteristic length as the diameter, $2r_0$. The Péclet number Pé_1 is calculated using the diffusional distance method,

$$\text{Pé}_1 = 4(2r_0)^2/Dt_c = 16r_0^2/Dt_c,$$

where t_c is defined as the time for the cell to achieve its minimal volume under the perfect stirring regime. The Péclet number Pé_2 is calculated using the comparison of

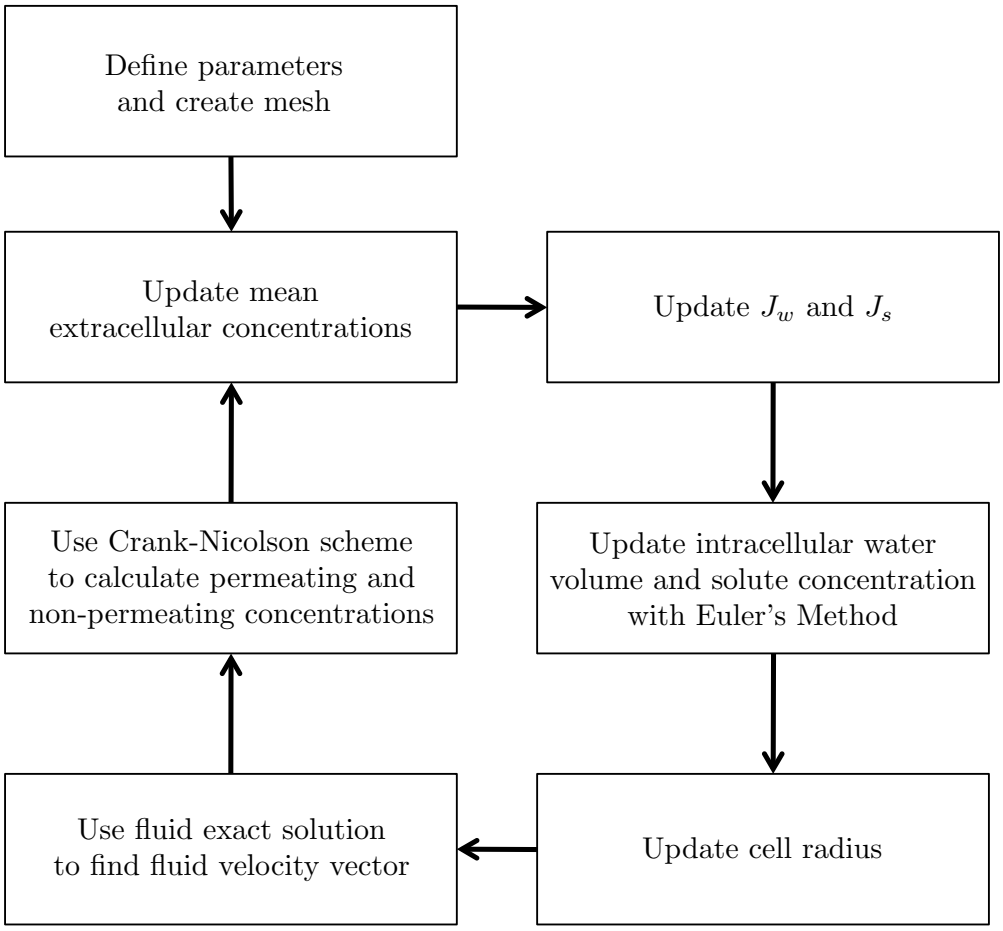

Figure 5.3: Flow chart of numerical method.

diffusion and fluid velocity,

$$\text{Pé}_2 = 2r_0u_0/D,$$

where we assign $u_0 = u_{top} = 10\mu\text{m/min}$.

From inspecting the volume response, it is clear that the analysis of Péclet numbers from Section 5.1.1 is reasonably accurate and that the most important parameter is the relative radius $\bar{b}$ of the annulus. In particular, we can see that the differences in almost all of the plots are due to the time it takes for the concentration around the cell to increase to its maximal, perfect mixing, concentration. Because this is a gradual increase, the cells at all time scales have time to equilibrate with their surroundings and the volume response is delayed and reduced. At smaller length and time scales, there is almost no effect of the concentration modeling other than the initial diffusion: the interaction between the extracellular concentration and extracellular flux is minimal.

On the other hand, as can be seen in particular at the organ scales, the efflux of water out of the tissue does seem to have an effect on the extracellular concentration profile. In particular, in Fig. 5.5, for $\bar{P}_s = 1.4$ at the organ scale there are three concentration phases present. During the first phase, the local concentration around the organ is not enough for the organ to produce a significant efflux of water into the surrounding area. During the second phase, however, this efflux seems to have slowed the effect of diffusion considerably. During the third phase, the influx back into the organ actually causes the advective increase of local concentration around the organ. A close-up view of phase three in one case is shown in Fig. 5.7, where the concentration of the bulk solution is given by the solid line, and the concentration at

Figure 5.4: Plots of total volume versus time at four length scales, corresponding to four sets of Péclet numbers, three unitless permeability coefficients, and with the unitless annulus radius $\bar{b} = 2$.

Figure 5.5: Plots of total volume versus time at four length scales, corresponding to four sets of Péclet numbers, three unitless permeability coefficients, and with the unitless annulus radius $\bar{b} = 4$.

Figure 5.6: Plots of total volume versus time at four length scales, corresponding to four sets of Péclet numbers, three unitless permeability coefficients, and with the unitless annulus radius $\bar{b} = 10$.

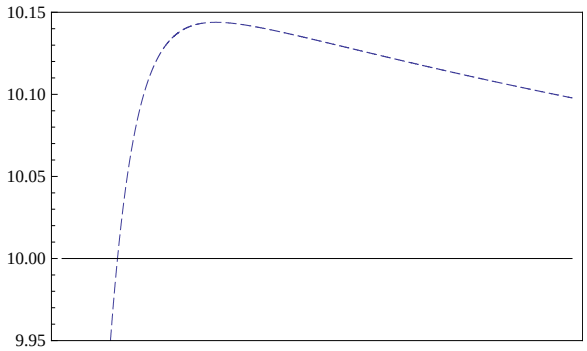

Figure 5.7: Close up view of membrane boundary concentration versus time (dashed line) for an organ sized radius. The influx of water advectively carries the solutes to the membrane boundary, and increases this concentration past the bulk concentration (solid line). This effect is present but is less pronounced at smaller radii.

the cell is given by the dashed line. The "overshoot" of concentration has the effect of speeding up the equilibration process. Interestingly, the first phase outlined above has the opposite effect, so the net effect is diminished over time.

In Fig. 5.8 we show the effects of changing the fluid velocity into the region on the volume response of a cell at the oocyte scale. At the radius characteristic of an oocyte, the volume response at fluid velocities of three orders of magnitude difference are very slight.

Plots of the extracellular concentration profiles are given in Fig. 5.9. Here the cell radius is set to the tissue scale, and $\bar{P}_s$ is set to 1.4. The figure shows concentration profiles both along the $R = 0$ boundary and in Ω_s at time $t = 0.5$. As the fluid velocity is increased, the concentration distribution is altered. These results raise the question of whether the cell will shrink with radial symmetry. If the membrane is allowed to be free in more than the radial dimension, then one might expect that in some of

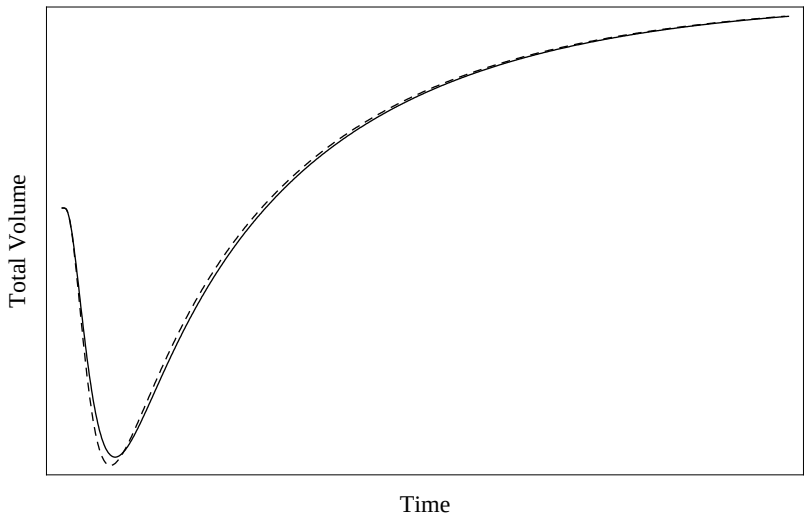

Figure 5.8: Plot of total volume in two cases under the full model and $r_0 = 50\,\mu$m. Simulations with $u_{top} = 1\,\mu$m/min (solid line) and $u_{top} = 1000\,\mu$m/min (dashed line) show that at the extremes of reasonable fluid velocity oocyte sized cell volume response is not affected.

the cases shown in Fig. 5.9 the membrane would not shrink spherically. This sort of aspherical shrinkage is sometimes encountered in laboratory observation of cells undergoing the typical volume fluxes modeled here, and the non uniform distribution of concentrations may play a role in this aspherical shrinking.

Additionally, the non-uniformity of the concentration distribution along the cell membrane also indicates that for larger tissues and organs, significant concentration gradients may exist along the membrane, causing stress. This membrane stress may cause cell, tissue or organ damage. Interestingly, the intuitive method one might employ to reduce these gradients would be to increase the fluid velocity. As seen in Fig. 5.9, this approach in fact has the negative effect of increasing the concentration gradient along the cell boundary.

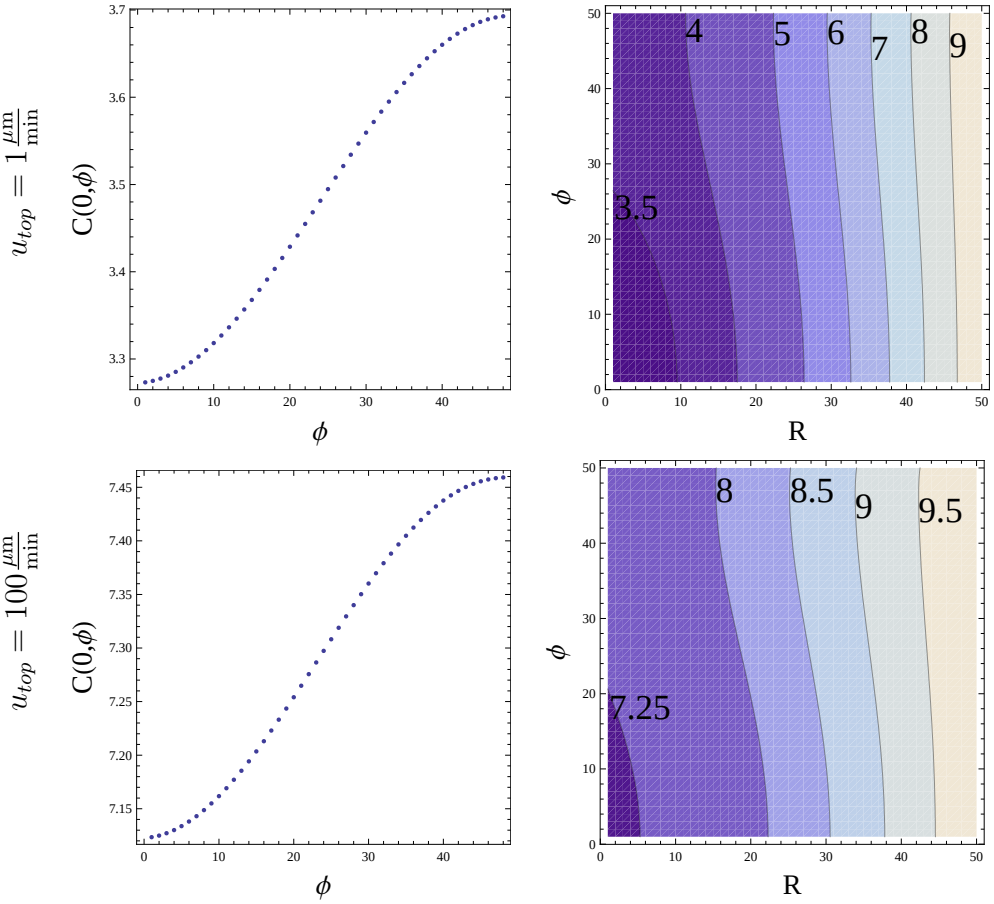

Figure 5.9: Plots of CPA concentration at two fluid velocities. In the left column, the plot is of the concentration profile at each node along the $R = 0$ boundary. The right column shows the concentration distribution in Ω_t. In each case there is approximately a 0.5 molal concentration difference between the top and bottom of the cell. This difference will generate a significantly different water flux profile at the top and bottom of the cell, causing stress along the membrane. (Recall that the "top" of the cell is at $\phi = 0$.)

5.5 Discussion and Conclusions

The results of the construction of this model were mixed, and the dependence on the unknown parameter $\bar{b}$ indicates that there are some physical questions that must be addressed before this model may be utilized uniformly. At the single somatic cell scale of approximately 10 μm diameter, clearly there is little benefit to accounting for the advection and diffusion effects at room temperature. Thus the optimal controls devised in Chapter 4 are not influenced by the fluid velocity field needed to achieve continuous control of concentrations M_1 and M_2. However, it is clear that as cell sizes increased to even single cells the of the oocyte scale, some effects, and most notably the reduction in total cell volume flux, are found independent of $\bar{b}$. Ultimately, it seems that the radius does not change enough to effect the concentration distribution. Though the advection due to the transmembrane flux does seem to alter the immediate concentration distribution around the cell, but this is on the order of at most 1%, and thus alone does not significantly influence the volume versus time response of cells. It would be very interesting to investigate these phenomena in a real biological system. To that aim a continuous perfusion chamber was developed to mimic the conditions assumed in the model. The design of this chamber is outlined in Appendix A-4.

The effects of advection due to higher fluid velocities become important at longer characteristic length scales. These effects may be important when devising CPA addition or removal protocols for tissues and organs. One might most effectively avoid the concentration gradients along the cell, tissue, or organ boundary by altering the fluid velocity field, either by stirring so that the fluid velocity field is random, or by

altering the direction of the velocity source so that no region of the cell, tissue, or organ is in the "lee" of the flow.

The relevance of the characteristic length scale is of special interest in the case of spermatozoa, a cell type that is challenging to freeze for many species. In the case of sperm, in the "width" dimension, perpendicular to the tail, the length scale is quite small–less than 3 μm diameter (see Fig. 5.10). On the other hand, for different species the length scale ranges from 50 to 150 μm. Because sperm orient themselves in the direction of the fluid velocity, there may be a chance that at some concentrations and fluid velocities, there is a concentration gradient along the tail, inducing membrane stress. In fact, when sperm are exposed to high concentrations of non-permeating solutes, we see tail looping effects that may be caused by concentration gradients. It is relatively straightforward to modify the code used in this chapter to aspherical, sperm-shaped, cells. It is beyond the scope of this chapter and thesis to analyze the effects of a swimming spermatozoa, but we note that in the high concentrations of sugars used in cryopreservation of spermatozoa, sperm are rendered temporarily immotile.

The utility of this model extends beyond the basic applications outlined in the preceding chapters. Most notably, at subzero temperatures, diffusion of solutes and water significantly affects the rate at which water can form ice [5], called constitutional supercooling [32]. Because the diffusion constant decreases exponentially with temperature, the Péclet number increases exponentially, indicating that significant gradients and advective effects may form at subzero temperatures.

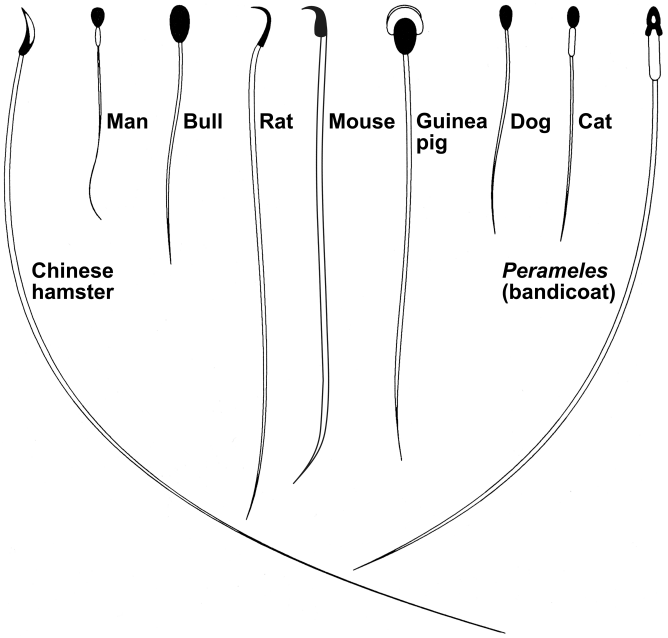

Figure 5.10: Morphological comparison of mammalian spermatozoa. Redrawn and modified from [61].

Appendices

A-1 Derivation of solute-solvent flux model

Here we present the derivation of the model used in this manuscript (and by others in the cryobiology literature [66, 63, 62], and also in general by Hernandez [55]). We begin by noting that there are a multitude of transmembrane flux models to choose from. Models exist that accurately describe the movement of water and solutes through individual transmembrane pores, but these models deal with mostly equilibrium or near-equilibrium flux, which is not relevant to the purposes of cryobiological modeling. In the cryobiological modeling regime, there tend to be two competing models, but Kleinhans [66] makes the Occam's razor argument that the simpler one defined by Jacobs [57] is sufficient for cryobiological applications:

$$\dot{V}_w = -L_p ART(\pi^e - \pi^i) \qquad \dot{s} = P_s A(M_s^e - M_s^i) \tag{11}$$

Where V_w is the intracellular water volume, s is the moles of intracellular permeating solute, L_p and P_s are the hydraulic conductivity (related to the water permeability) and solute permeability,A is the cell surface area, assumed constant, R is the gas constant, T is the temperature, $\pi^{e,i}$ are the extra- and intracellular osmotic pressures, respectively, and $M_s^{e,i}$ are the extra- and intracellular molalities of the permeating solute, respectively. Extracellular terms are assumed known, but to have a closed system, we must define π^i and M_s^i. Molality is moles per solvent volume, so $M_s^i = s/V_w$. Osmolality is a nonlinear function of molality or mole fraction [95], and much effort has been spent determining this relationship in the literature, and the cryobiological literature in particular. Some have taken a purely experimental approach, defining phase-diagrams that describe osmolality (in the form of freezing point depression) for combinations of cryoprotective agents and salts [47, 76, 114, 115], and others have

take a theoretical approach, either derived heuristically [65], or from thermodynamics [36].

Elliott *et. al* [36] show that osmotic pressure π is described naturally by the osmotic virial equation with a Gugenheim's Naïve Approximation mixing term:

$$\pi = p(\chi_{\text{np}}, \chi_2, \ldots, \chi_n) = \sum_i \chi_i + \sum_i \sum_j \frac{B_i + B_j}{2} \chi_i \chi_j, \tag{12}$$

where χ_j is the molality of solute j, and χ_{np} is the molality of the non-permeating solute. The intracellular molality of the jth solute, is given by the function

$$\chi_j = \frac{n_j}{V_w} = \frac{n_{iso}}{V_w^{iso}} \frac{x_j}{x_1} = \frac{m_{iso} V_w^{iso}}{V_w^{iso}} \frac{x_j}{x_1} = m_{iso} \frac{x_j}{x_1}.$$

Thus, with an assumed non-permeating osmolyte molality $m_{iso} x_{\text{np}}/x_1$ (i.e. $\dot{x}_{\text{np}} \equiv 0$),

$$\pi^i(\mathbf{x}) = p\left(m_{iso} \frac{x_{\text{np}}}{x_1}, m_{iso} \frac{x_2}{x_1}, \ldots, m_{iso} \frac{x_k}{x_1} \right).$$

Furthermore, with extracellular media concentrations $m_j^e(t)$ for $j = 2, \ldots, k$ and $m_{\text{np}}^e(t)$, forming the extracellular non-permeating osmolyte concentration, we have

$$\pi^e(t) = p(m_{\text{np}}^e(t), m_2^e(t), \ldots, m_k^e(t)).$$

The model proposed by Mazur and Keinhans [65] is not based on a thermodynamic theory, but it has a similar form when $B_j = 0$ and was accurate when compared to existing measured phase diagrams. For many solutes $B_i \ll 1$, and thus for the purposes of analysis we will use the assumption $B_i = 0$, allowing a significant simplification of our system and analytic solutions of our system of equations. This is an assumption often used in cryobiology [62, 66], though the error induced by this assumption increases dramatically at higher concentrations [36], and thus may be inappropriate

for some cryobiological applications. In the future, we may return to the case $B_j \neq 0$ and perform the optimization numerically. This assumption yields

$$\begin{aligned}\pi^i(\mathbf{x}) &= m_{iso}\left(\frac{x_{\text{np}}}{x_1} + \sum_{i=2}^{k}\frac{x_i}{x_1}\right), \\ &= \frac{m_{iso}}{x_1}\left(x_{\text{np}} + \sum_{i=2}^{k} x_i\right),\end{aligned}$$

and

$$\pi^e(t) = m^e_{\text{np}}(t) + \sum_{i=2}^{k} m^e_j(t).$$

Finally, in our dimensionless variables, we note that with our $B_j = 0$ assumption $m_{iso} = \pi_{iso}$ yielding

$$P^i(\mathbf{x}) = \frac{1}{x_1}\left(x_{\text{np}} + \sum_{i=2}^{k} x_i\right),$$

and

$$P^e(t) = M^e_{\text{np}}(t) + \sum_{i=2}^{k} M^e_j(t).$$

A-2 Pontryagin Maximum Principle

Recall from Section 3.3.3, using controls $M \in \mathbb{A}$ such that $M : \mathbb{R}^+ \to \text{CP}$, we wish to control the system $\dot{x} = f(x, M)$, with $x(0) = x^i$ and $x(\tau) = x^f$ such that the payoff functional $P(M) = -\int_0^\tau x_1(t)dt$ is maximized. Also recall that we defined the control theory Hamiltonian $H(x, p, M) := f(x, M)\cdot p + x_1$. In Section 3.3.3, we utilize a classic result in optimal control theory, the Pontryagin Maximum Principle [111], in which necessary conditions for optimality are defined. Suppose the constraint is defined by $g(x) \leq 0$, where $g : \mathbb{R}^n \to \mathbb{R}$. Then we define $c(x, M) := \nabla g(x) \cdot f(x, M)$ and note that if the constraint is active for $t \in (s_1, s_2)$, then $c(x(t), M(t)) = 0$.

Theorem 18 (Pontryagin Maximum Principle)**.** *If M^* maximizes the payoff functional P, and $x^* \in \operatorname{int} S$ is the corresponding state, then there exists a costate p^* such that*

$$H(x^*, p^*, M^*) = \max_{M \in \mathrm{CP}} H(x^*, p^*, M),$$

and $t \mapsto H(x^*(t), p^*(t), M^*(t)) = 0$. If for some $s \in [\tau_1, \tau_2]$ we have $g(x(s)) = 0$, M^* maximizes P, and $x^* \in \partial S$ is the corresponding state, then there exists a costate p^* and $\lambda^* : [\tau_1, \tau_2] \to \mathbb{R}$ such that

$$\dot{p}^* = -\nabla_x H(x^*, p^*, M^*) + \lambda^* \nabla_x (c(x^*, M))$$

and

$$H(x^*, p^*, M^*) = \max_{M \in \mathcal{A}} \{H(x^*, p^*, M) : c(x^*, M) = 0\}.$$

Moreover, $p(\tau_1^-) = p(\tau_1^+)$ and $p(\tau_2^-) = p(\tau_2^+) + \lambda^* \nabla_x c(x^*, M)$.

In Chapter 3 we have no constraints, but in Chapter 4, the constraint portion of the theorem is used.

A-3 Boltayanskii Sufficiency Theorem

This theorem, critical to Chapters 3 and 4, is from Chapter 4, Section 12, Paragraph 45 of *Mathematical Methods of Optimal Control*, V.G. Boltyanskii, 1971. We add subitems to make some statements more concrete.

We first introduce the concept of *regular synthesis* for the system $\dot{x} = f(x, u)$ for which the continuity of the derivatives $\partial f^i / \partial x^j$ and $\partial f^i / \partial u^k$

will not be assumed. Suppose that a piecewise smooth set N of dimension $\leq n-1$, piecewise smooth sets

$$P^0 \subset P^1 \subset \ldots \subset P^{n-1} \subset P^n = S,$$

and a function $v : S \to \mathcal{A}$ are given. We will say that the sets P^i and the function v realize a *regular synthesis* for $\dot{x} = f(x,u)$ in the region S if the following conditions are satisfied:

1. The set P^0 contains the point $a = x_1$ but does not have limiting points in the open set S. Each component of the set $P^i - (P^{i-1} \cup N)(i = 1, 2, \ldots, n)$ is a smooth $i-$dimensional manifold in S; these components will be called *i-dimensional cells*. The points of the set P^0 will be called zero-dimensional cells. The function $v(x)$ is continuous and continuously differentiable on each cell and can be extended as a continuously differentiable function into a neighborhood of the cell.

2. All cells are grouped into cells of the first and second kind. All $n-$dimensional cells are cells of the first kind, all zero-dimensional cells are cells of the second kind.

3. (a) If σ is an $i-$dimensional cell of the first kind, then each point of this cell has a unique trajectory of the equation

$$\dot{x} = f(x, v(x)) \tag{13}$$

passing through it.

(b) There exists an $(i-1)-$dimensional cell $\Pi(\sigma)$ such that each trajectory of the system (13) traversing the cell σ leaves this cell after a finite time, arrives at the cell $\Pi(\sigma)$ at a nonzero angle, and approaches the latter with a nonzero phase velocity.

(c) If σ is a one dimensional cell of the first kind, then it is a piece of a phase trajectory of (13) approaching a zero-dimensional cell $\Pi(\sigma)$ with a nonzero phase velocity.

(d) If σ is an $i-$dimensional cell of the second kind distinct from the point a, then there exists an $(i+1)-$dimensional cell $\Sigma(\sigma)$ of the first kind such that from any point of the cell σ there emanates a unique trajectory of (13) traversing the cell $\Sigma(\sigma)$; moreover, the function $v(x)$ is continuous and continuously differentiable on $\sigma \cup \Sigma(\sigma)$.

4. The above conditions make it possible to continue the trajectories of (13) from cell to cell: from the cell σ to the cell $\Pi(\sigma)$ if $\Pi(\sigma)$ is of the first kind, and from the cell σ to the cell $\Sigma(\Pi(\sigma))$ if $\Pi(\sigma)$ is of the second kind. It is required that each such trajectory traverse only a finite number of cells (that is, each such trajectory "pierces" only a finite number of cells of the second kind). Moreover, each such trajectory terminates at the point a. The above trajectories will be called "distinguished" trajectories. Thus, a single distinguished trajectory (leading to the point a) emanates from every point of the set $G-N$. It is also required that a (possibly non-unique) trajectory

of system (13) leading to the point a emanates from every point of the set N. These will also be called "distinguished" trajectories.

5. All distinguished trajectories satisfy the maximum principle (see Section 18).

6. The value of the transition time from the point x_0 to the point a, calculated along distinguished trajectories (terminating at the point a), is a continuous function of the initial point x_0. (In particular, if several distinguished trajectories emanate from the point $x_0 \in N$, then the value of the transition time is the same for these trajectories.)

Theorem 19. *If a regular synthesis is realized in G for $\dot{x} = f(x, u)$ (assuming the existence of continuous derivatives $\frac{\partial f^i}{\partial x^j}$ and $\frac{\partial f^i}{\partial u^k}$), then all distinguished trajectories are optimal (in G).*

A-4 Design of an apparatus to measure the effects of fluid velocity fields and diffusion on cell permeability

In order to estimate values of water and solute membrane permeability (L_p and P_s respectively) that account for the diffusion and advection in the extracellular environment, experiments must be conducted that allow for the measuremtent of cell volume as a function of time when exposed to various extracellular conditions. Our experimental apparatus can be described as follows (see figure 11). A 3 mm diameter cylindrical chamber is divided into upper and lower parts by a permeable membrane with 3-5 μm pores randomly distributed across the membrane. We assume that at the flow rates used, the membrane is perfectly permeable; it offers no resistance and adds

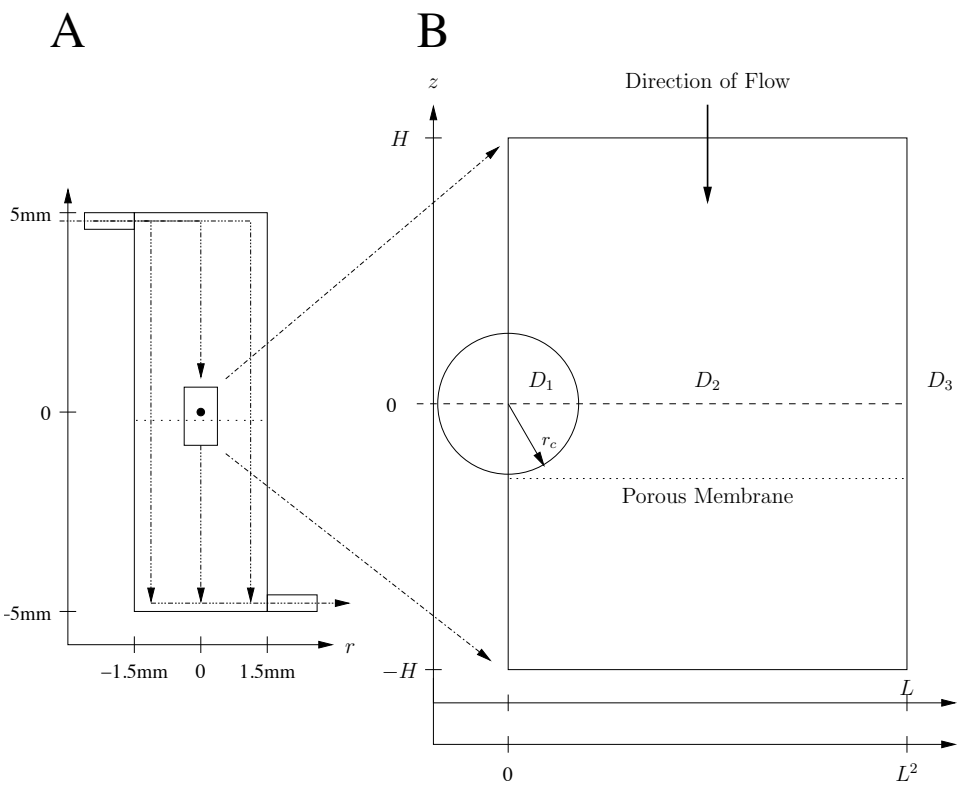

Figure 11: Diagram of the system and device schematic D_1 is the interior of the cell D_2 is the exterior of the cell and D_3 is the region assumed to have perfect mixing (i.e. concentration is invariant with time, i.e. concentration is equal to c_b). Cells are fixed at the permeable membrane boundary, and fluid flows from the top to the bottom of the chamber at a constant rate. The concentration of this fluid can be changed either in stepwise fashion, or continuously.

no turbulence to the media. The height of the cylinder is 10 mm total, with ports at the top and bottom for the addition and removal of cells and media, and the top and bottom of the cylinder are capped with glass coverslips. Fluid and cells are loaded into the apparatus from the top and both gravity and fluid motion carry the cells to the membrane where they are suspended. We assume that the fluid flow around the cells at the membrane is strictly perpendicular to the membrane, is axially symmetric around the cells, and has zero vorticity. Thus, with this apparatus we are able to control the extracellular environment by altering flow rates and fluid concentrations.

Consider the spherical region D_1 to represent a cell with (variable) radius r_c immersed in the experimental chamber where it is bathed with fluid containing permeable and nonpermeable solutes. In our apparatus (see Figure systemdiagram2), the fluid flow is from top to bottom. Because we assume the flow is axisymmetric with respect to a vertical axis passing through the center of our spherical cell, it is convenient to use cylindrical coordinates; for each cell, we set the origin at the cell center with $0 \leq r \leq L$ denoting the radius away from the center of the cell along the membrane axis, and $-H \leq z \leq H$, the height measured from the center of the cell. We let L and H denote bounds for the region where the fluids are axially symmetric with zero vorticity.

A-5 Exact solutions of fluid and concentration models

A-5.1 Solutions for the ϕ component of u.

We solve $v_{\phi\phi} + h(r)v_r + h(r)^2 v_{rr} = 0$ with boundary conditions $v(0,\phi) = 0$, $v(1,\phi) = \frac{1}{b}u_z^{\text{top}}(t)\sin\phi$, $v(r,0) = 0$, and $v(r,\pi) = 0$. We can solve by assuming $v(r,\phi) = F(\phi)R(r)$. This yields two ODEs: $F''(\phi)/F(\phi) = c$ and

$$h(r)R'(r)/R(r) + h(r)^2 R''(r)/R(r) = -c.$$

Because of the boundary conditions the equation $F''(\phi) - cF(\phi) = 0$ must have a solution of the form $F(\phi) = c_1 \cos\sqrt{-c}\,\phi + c_2 \sin\sqrt{-c}\,\phi$. If $F(0) = 0$, then we have $c_1 = 0$. Since $F(\pi) = 0$, $\sqrt{-c} = n$ for $n \in \mathbb{Z}$, and so $c = -n^2$, and $F_n(\phi) = c_2 \sin n\phi$.

Next we solve $h(r)R'(r) + h(r)^2 R''(r) + cR(r) = 0$. We note that $h(r) = r + \frac{\rho(t)}{b-\rho(t)}$, and that $h'(r) = 1$. If we assume that the solution is of the form $R(r) = h(r)^m$, we

get

$$h(r)^m(m(m-1)+m+c)=0,$$

thus $m^2-m+m-n^2=m^2-n^2=0$, and thus $m=\pm n$. Define $S_n(r)=h^n$ and $T_n(r)=h^{-n}(r)$. In this case the solution will be $v(r,\phi)=\sum_n a_nF_n(\phi)(b_nS_n(r)+c_nT_n(r))$, and we automatically satisfy the $v(r,0)=v(r,\pi)=0$ conditions. Since $v(0,\phi)=0$, we can solve for b_n in terms of c_n: we have $b_nS_n(0)+c_nT_n(0)=0$ thus $b_n=-c_nT_n(0)/S_n(0)$. Combining terms, we then have

$$v(r,\phi)=\sum_n a_nF_n(\phi)\Big(\frac{-T_n(0)S_n(r)}{S_n(0)}+T_n(r)\Big).$$

If we take only the $n=1$ term, we have

$$\begin{aligned}v(r,\phi)&=a_1F_1(\phi)\Big(\frac{-T_1(0)S_1(r)}{S_1(0)}+T_1(r)\Big)\\&=a_1\sin\phi\Big(-\frac{h^{-1}(0)h(r)}{h(0)}+h^{-1}(r)\Big).\end{aligned}$$

Finally, if we set

$$a_1=\frac{u_z^{\text{top}}(t)}{b}\frac{1}{-\frac{h^{-1}(0)h(1)}{h(0)}+h^{-1}(1)},$$

we can satisfy all boundary equations, and the complete solution is

$$v(r,\phi)=\frac{u_z^{\text{top}}(t)}{b}\frac{1}{-\frac{h^{-1}(0)h(1)}{h(0)}+h^{-1}(1)}\sin\phi\Big(-\frac{h^{-1}(0)h(r)}{h(0)}+h^{-1}(r)\Big).$$

A-5.2 Solutions for the r component of u

Let us solve $u_{\phi\phi}+u+h(r)u_r+h(r)^2u_{rr}=0$ with boundary conditions $u(0,\phi)=u_0(t)$, $u(1,\phi)=\frac{u_z^{\text{top}}(t)\cos\phi}{b-\rho(t)}-Au_0(t):=u_1(t)\cos\phi-Au_0(t)$, $u_\phi(r,\phi)=u_\phi(r,0)=0$. We will solve the system with three sets of boundary conditions and add the solutions to find

the complete solution. The first, $w_1(r,\phi)$ is chosen to satisfy

$$\begin{aligned} w_{1\phi\phi} + w_1 + h(r)w_{1r} + h(r)^2 w_{1rr} &= 0, \\ w_1(0,\phi) &= 0, \\ w_1(1,\phi) &= u_1(t)\cos\phi, \\ w_{1\phi}(r,0) &= w_{1\phi}(r,\pi) = 0. \end{aligned}$$

The second function $w_2(r,\phi)$, is the solution of the boundary value problem

$$\begin{aligned} w_{2\phi\phi} + w_2 + h(r)w_{2r} + h(r)^2 w_{2rr} &= 0, \\ w_2(0,\phi) &= 0, \\ w_2(1,\phi) &= Au_0(t), \\ w_{2\phi}(r,0) &= w_{2\phi}(r,\pi) = 0. \end{aligned}$$

And, the third function $w_3(r,\phi)$ solves

$$\begin{aligned} w_{3\phi\phi} + w_3 + h(r)w_{3r} + h(r)^2 w_{3rr} &= 0, \\ w_3(0,\phi) &= u_0(t), \\ w_3(1,\phi) &= 0, \\ w_{3\phi}(r,0) &= w_{3\phi}(r,\pi) = 0. \end{aligned}$$

Let us these in order by separation of variables. Assuming $w_1(r,\phi) = F(\phi)R(r)$, we get

$$\frac{F''(\phi)}{F(\phi)} + 1 + h(r)\frac{R'(r)}{R(r)} + h(r)^2\frac{R''(r)}{R(r)} = 0.$$

In order to keep track of the 1-term, we separate this into two ODE's as follows:

$$\frac{F''}{F} + 1 = c,$$
$$h(r)\frac{R'(r)}{R(r)} + h(r)^2\frac{R''(r)}{R(r)} = -c.$$

For reasons that will become clear, we solve first with $c = 0$. This gives us two simple ODEs $F''+F = 0$ which has solution $F(\phi) = c_1\cos\phi+c_2\sin\phi$, and $h(r)^2R''+h(r)R' = 0$ which has a solution $R(r) = c_3 + c_4\ln h(r)$. In view of the boundary conditions, we see that $F'(0) = F'(\pi) = 0$, which means $c_2 = 0$. Thus collecting and combining terms we have the solution $w_1(r,\phi) = a_1\cos\phi(c_3 + c_4\ln h(r))$. Since $w_1(0,\phi) = 0$, we must have $c_3 = -c_4\ln h(0)$. To satisfy $w_1(1,\phi) = u_1(t)\cos\phi$, we set $a_1 = \frac{u_1(t)}{\ln h(1)-\ln h(0)}$. Then the solution is

$$w_1(r,\phi) = \frac{u_1(t)}{\ln h(1) - \ln h(0)}\cos\phi(\ln h(r) - \ln h(0)).$$

For the $w_2(r,\phi)$ case, we solve the system again. This time setting $c = 1$ yields the solution $F(\phi) = c_1 + c_2\phi$. The boundary conditions $F'(0) = 0$ and $F'(\pi) = 0$ mean $c_2 = 0$, thus $F(\phi) = c_1$. Next, we solve $h(r)^2R''(r) + h(r)R'(r) + R = 0$. Approaching this as before, we find the indicial equation is $m^2 + 1 = 0$, meaning $m = i$, yielding the solution $R(r) = c_3\cos(\ln h(r)) + c_4\sin(\ln h(r))$. As before we now combine to get $w_2(r,\phi) = a_1\cos(\ln h(r)) + a_2\sin(\ln h(r))$. Since $w_0(0,\phi) = 0$, $a_1 = -a_2\tan(\ln(h(0)))$. Thus $w_2(r,\phi) = a_2(-\tan(\ln(h(0)))\cos(\ln h(r)) + \sin(\ln h(r)))$. Finally, since $w_2(1,\phi) = -Au_0(t)$, we can solve for $a_2 = -(-\tan(\ln(h(0)))\cos(\ln h(1))+\sin(\ln h(1)))^{-1}Au_0(t)$, and upon substitution,

$$\begin{aligned} w_2(r,\phi) &= -\frac{Au_0(t)(-\tan(\ln(h(0)))\cos(\ln h(r)) + \sin(\ln h(r)))}{(-\tan(\ln(h(0)))\cos(\ln h(1)) + \sin(\ln h(1))} \\ &= \frac{Au_0(t)(-\tan(\ln(h(0)))\cos(\ln h(r)) + \sin(\ln h(r)))}{(\tan(\ln(h(0)))\cos(\ln h(1)) - \sin(\ln h(1))}. \end{aligned}$$

Finally, for the $w_3(r,\phi)$ case, we note that the solution will be very similar to the w_2 case, with slightly different boundary conditions. We have as above, $w_3(r,\phi) = a_1\cos(\ln h(r)) + a_2\sin(\ln h(r))$, but here $w_3(1,\phi) = 0$ implies $a_1 = -a_2\tan(\ln(h(1))$. Next, $w_3(0,\phi) = u_0(t)$ implies $a_2 = u_0(t)/(-\tan(\ln(h(1)))\cos(\ln(h(0)))+\sin(\ln(h(0))))$. Combining and collecting, we get

$$w_3(r,\phi) = \frac{u_0(t)\big(-\tan(\ln(h(1)\cos(\ln(h(r))) + \sin(\ln(h(r)))\big)}{-\tan(\ln(h(1)))\cos(\ln(h(0))) + \sin(\ln(h(0)))}. \tag{14}$$

The complete solution is

$$\begin{aligned} u(r,\phi) &= w_1(r,\phi) + w_2(r,\phi) + w_3(r,\phi) \\ &= \frac{u_1(t)}{\ln h(1) - \ln h(0)}\cos\phi(\ln h(r) - \ln h(0)) \\ &\quad + \frac{Au_0(t)(-\tan(\ln(h(0)))\cos(\ln h(r)) + \sin(\ln h(r)))}{(\tan(\ln(h(0)))\cos(\ln h(1)) - \sin(\ln h(1))} \\ &\quad + \frac{u_0(t)\big(-\tan(\ln(h(1)\cos(\ln(h(r))) + \sin(\ln(h(r)))\big)}{-\tan(\ln(h(1)))\cos(\ln(h(0))) + \sin(\ln(h(0)))}. \end{aligned}$$

A-5.3 An exact solution of the concentration model in a special case.

Finally, for testing of numerics, it is advantageous to have a non-trivial exact solution of the concentration model. We have the system

$$c_t = \frac{\epsilon u^\phi}{q(r)}c_\phi + \left(\frac{\epsilon u^r}{q'(r)} + \frac{D}{q(r)q'(r)}\right)c_R + \frac{D}{q(r)^2}c_{\phi\phi}(r,\phi) + \frac{D}{q'(r)^2}c_{RR}.$$

Let us assume that $u = 0$, $D = 1$, $b = 1$, and $\rho = 0$ to obtain the PDE

$$c_t = \frac{1}{R}c_R + \frac{1}{R^2}c_{\phi\phi} + c_{RR}.$$

If we assume $c_{\phi\phi} = 0$, we can solve via separation of variables. Letting $c(r,t) = T(t)R(r)$, we find that we have two ODEs: $T'/T = -\lambda$ and $rR'' + R' + r\lambda R = 0$.

Solving these ODEs with $\lambda = 1$, we get $c(r,t) = J_0(r)e^{-t}$ as a solution, where $J_0(r)$ is the Bessel J function. Multiplying by an affine function of ϕ, we have the solution

$$c(r,\phi,t) = (k_1 + k_2\phi)J_0(r)e^{-t}.$$

A-6 Numerical analysis of a curved boundary condition: a general approach to Dirichlet and Neumann conditions and uneven grid spacing

When deriving difference equations for numerical integration, if the grid is evenly spaced, regular, and boundaries are aligned with the grid (e.g. rectangular on a rectangular grid), standard difference equations are available that allow solutions to many linear differential equations. When boundaries are not aligned with the grid, if grid spacing is inconsistent, if differential equations involve mixed or higher order derivatives, or if a higher order of accuracy is desired, a different method for determining appropriate difference equations is required. The techniques used in this section do take advantage of modern computer algebra systems to develop completely generalized finite difference schemes, but are most assuredly not new, as finite difference schemes have existed for a very long time.

Let $\mathbf{u}$ be a vector in a function space $C^n(\mathbb{R}^2, \mathbb{R})$ of u and its spatial derivatives (e.g. $\{u, u_x, u_y, u_{xx}, u_{xy}, u_{yy}, \ldots\}$). Define L as a linear functional that acts on $\mathbf{u}$. Then any linear non-evolution type differential equation can be written as $L\mathbf{u} = a$, where a is some function. Note that for evolution type PDEs, the same process can be used along with a time differencing scheme (e.g. forward Euler, Crank-Nicolsen, etc.).

Suppose we wish to find a difference equation for $L(u) = 0$ at the point (w, z). In order to do this, we must define a "halo" of points around (w, z). In a standard

centered differencing scheme with second order non-mixed derivatives, this "halo" will be the two points dx away from (w, z) in the x direction, and the two points dy away from (w, z) in the y direction. In our scheme, it is enough to have $(n + 1)$ points including (w, z) where n is the number of differentials in the differential equation(e.g. $u_x + u_{xx} + u_{yy}$ gives $n = 4$ because there are two derivatives in the x direction and two in the y direction. Note, it is possible to use more points to find higher order methods. Let $\mathbf{c} = (c_1, \ldots, c_{(n+1)!})$ be the vector of Taylor expansions of u at each point around $u(w, z)$, (including the point (w, z). The goal of any differencing scheme is to find $n!$ linear equations of these c_i that can be solved simultaneously. Typically, for $i \neq 1$, the c_i are either known as Dirichlet boundary conditions, or solved for as part of a larger system of equations. Note that each c_i can be written as a function of the vector $\mathbf{u}$. Because of this we can combine all equations into an $(n + 1)! \times (n + 1)!$ system of equations with $(n + 1)!$ unknowns:

$$A\mathbf{u} = \mathbf{c} \tag{15}$$

Where A is a matrix of the Taylor coefficients. If we solve this linear system, we have found a linear combination of the surrounding points of (w, z) that describe each element of $\mathbf{u}$. If $\det A$ is non-zero, then the solution to our differential equation at (w, z) is

$$LA^{-1}\mathbf{c}(w, z) = 0. \tag{16}$$

The difficulty is in finding A^{-1}, but for reasonably small (i.e. $n < 10$), this is quite possible with the aid of a computer algebra package such as Mathematica.

A-6.1 A simple example: Laplace's Equation

Let us look at a simple example: *Find a difference formula for u at (w, z) that solves $u_{xx} + u_{yy} = 0$ in terms of $u(w \pm dx, z \pm dy)$.* Let $\{c_1, c_2, c_3, c_4, c_5\} = \{u(x, y), u(x, y + dy), u(x + dx, y), u(x, y - dy), u(x - dx, y)\}$. Classically we could either derive or simply look up the second order (e.g. $\mathcal{O}(dx^2)$) centered difference formulas:

$$u_{xx} = \frac{c_5 - 2c_1 + c_3}{dx^2}$$
$$u_{yy} = \frac{c_4 - 2c_1 + c_2}{dy^2}.$$

To solve for $u(x, y)$, we substitute our difference formulas into the differential equation, yielding

$$\frac{c_5 - 2c_1 + c_3}{dx^2} + \frac{c_4 - 2c_1 + c_2}{dy^2} = 0, \tag{17}$$

and solve for the coefficients of each u term:

$$c_1\big(- 2\big(dx^{-2} + dy^{-2}\big)\big) + c_5 dx^{-2} + c_3 dx^{-2} + c_4 dy^{-2} + c_2 dy^{-2} = 0$$

Using our generalized method we define $\mathbf{c} = \{c_1, c_2, c_3, c_4, c_5\}$, and define $\mathbf{u} = \{u, u_x, u_{xx}, u_y, u_{yy}\}$. Performing Taylor expansions around $u(x, y)$ on $\mathbf{c}$ yields the matrix equation $A\mathbf{u} = \mathbf{c}$, i.e.

$$\begin{bmatrix} 1 & 0 & 0 & 0 & 0 \\ 1 & 0 & 0 & dy & \frac{dy^2}{2} \\ 1 & dx & \frac{dx^2}{2} & 0 & 0 \\ 1 & 0 & 0 & -dy & \frac{dy^2}{2} \\ 1 & -dx & \frac{dx^2}{2} & 0 & 0 \end{bmatrix} \begin{pmatrix} u(x, y) \\ u_x(x, y) \\ u_{xx}(x, y) \\ u_y(x, y) \\ u_{yy}(x, y) \end{pmatrix} = \begin{pmatrix} c_1 \\ c_2 \\ c_3 \\ c_4 \\ c_5 \end{pmatrix} \tag{18}$$

As long as A is nonsingular, A^{-1} can be calculated and we can solve for $\mathbf{u}$. Doing so

in this case yields

$$
\begin{aligned}
u(x,y) &= c_1, \\
u_x(x,y) &= \frac{c_3 - c_5}{2dx}, \\
u_{xx}(x,y) &= \frac{c_3 - 2c_1 + c_5}{dx^2}, \\
u_y(x,y) &= \frac{c_2 - c_4}{2dy}, \\
u_{yy}(x,y) &= \frac{c_2 - 2c_1 + c_5}{dy^2}.
\end{aligned}
$$

Substituting this back into the differential equation yields the same result as the classic method, with the added benefit that we've already calculated the difference equations for u_x and u_y. The downside of this technique is that because we've only expanded our Taylor series to $\mathcal{O}(dx^3)$, dividing by the requisite dx^2, yields a $\mathcal{O}(dx)$ method. Standard techniques take advantage of the symmetry of points in the "halo" to realize that the method derived is in fact $\mathcal{O}(dx^2)$. Therefore, any technique derived in this fashion will be of order at least 1 and may be higher if symmetries are involved, but without post-hoc analysis, this is unknown.

A-6.2 A more complicated example: Laplace's Equation on a non uniform grid

The real power of this method is when the grid spacing is non-uniform. Suppose we have the same equations with the same $\mathbf{u}$. Let $\mathbf{c}$ be any 6 points (including $c_1 = u(x,y)$) near (x,y). Then there is a set of values $\{a_i, b_i\}_{i=2}^{6}$ denoting the respective distances in the x and y directions such that the Taylor expansion matrix equation

$A\mathbf{u} = \mathbf{c}$ is

$$\begin{bmatrix} 1 & 0 & 0 & 0 & 0 & 0 \\ 1 & a_2 & \frac{a_2^2}{2} & b_2 & \frac{b_2^2}{2} & a_2 b_2 \\ 1 & a_3 & \frac{a_3^2}{2} & b_3 & \frac{b_3^2}{2} & a_3 b_3 \\ 1 & a_4 & \frac{a_4^2}{2} & b_4 & \frac{b_4^2}{2} & a_4 b_4 \\ 1 & a_5 & \frac{a_5^2}{2} & b_5 & \frac{b_5^2}{2} & a_5 b_5 \\ 1 & a_6 & \frac{a_6^2}{2} & b_6 & \frac{b_6^2}{2} & a_6 b_6 \end{bmatrix} \begin{pmatrix} u(x,y) \\ u_x(x,y) \\ u_{xx}(x,y) \\ u_y(x,y) \\ u_{yy}(x,y) \\ u_{xy} \end{pmatrix} = \begin{pmatrix} c_1 \\ c_2 \\ c_3 \\ c_4 \\ c_5 \\ c_6. \end{pmatrix} \tag{19}$$

If A is non-singular, we can solve for $\mathbf{x}$ linearly in terms of $\mathbf{c}$, do the appropriate substitutions into our PDE and we have now found an at least first order non-uniform difference equation for $u(x, y)$. It is worth noting that writing down a general difference formula for the above equation is impractical because the solution to the above equation in its entirety and generality is many pages of expressions. In practical cases, A will be entirely numerically expressed. This will allow significant improvements in the speed of calculation and expression of the result. For a more concrete example, we let $\{a_i, b_i\}_{i=2}^6$ be equal to random numbers between 0 and 1.

$$\begin{bmatrix} 1 & 0 & 0 & 0 & 0 & 0 \\ 1 & 0.0276 & 0.0008 & 0.6985 & 0.4879 & 0.01935 \\ 1 & 0.6143 & 0.3774 & 0.5764 & 0.3322 & 0.3541 \\ 1 & 0.5137 & 0.2639 & 0.7241 & 0.5244 & 0.3720 \\ 1 & 0.2585 & 0.0668 & 0.05711 & 0.0032 & 0.0147 \\ 1 & 0.1014 & 0.01029 & 0.4337 & 0.1881 & 0.0440 \end{bmatrix} \begin{pmatrix} u(x,y) \\ u_x(x,y) \\ u_{xx}(x,y) \\ u_y(x,y) \\ u_{yy}(x,y) \\ u_{xy}(x,y) \end{pmatrix} = \begin{pmatrix} c_1 \\ c_2 \\ c_3 \\ c_4 \\ c_5 \\ c_6. \end{pmatrix} \tag{20}$$

$$u(x,y) = c_1$$

$$u_r(x,y) = -4.5818c_1 - 0.7368c_2 - 2.5097c_3 + 2.1926c_4 + 5.4995c_5 + 0.1363c_6$$

$$u_{rr}(x,y) = 3.8250c_1 + 4.749c_2 + 9.1990c_3 - 8.1726c_4 - 3.8834c_5 - 5.7175c_6$$

$$u_z(x,y) = -2.2160c_1 - 0.9652c_2 + 1.5632c_3 - 2.0024c_4 - 1.7335c_5 + 5.3541c_6$$

$$u_{zz}(x,y) = 1.2386c_1 + 3.6905c_2 - 1.9784c_3 + 2.5251c_4 + 2.3659c_5 - 7.8417c_6$$

$$u_{rz}(x,y) = 3.4933c_1 - 5.6750c_2 - 3.3142c_3 + 5.7964c_4 - 4.7999c_5 + 4.4995c_6$$

A-6.3 An example with Neumann boundary conditions

When Neumann conditions are encountered in a case where derivative directions are not orthogonal to the standard grid, or where grid spacing is non-uniform, or where nonstandard derivatives are known (e.g. u_{xy}) the above techniques are quite useful. Let us consider the case where the Neumann condition at the boundary is $au_x + bu_y = \alpha$, where a, b, and α are constants (e.g. on a circle with radius r where the boundary condition is that the normal derivative is equal to α, $a = \frac{x}{r}$ and $b = \frac{y}{r}$). This equation fits into our structure above by replacing one of the above equations, say c_n for c_6. Note that in this case, we actually solve for the value u on the boundary itself.

The general form will then be

$$\begin{bmatrix} 1 & 0 & 0 & 0 & 0 & 0 \\ 1 & a_2 & \frac{a_2^2}{2} & b_2 & \frac{b_2^2}{2} & a_2 b_2 \\ 1 & a_3 & \frac{a_3^2}{2} & b_3 & \frac{b_3^2}{2} & a_3 b_3 \\ 1 & a_4 & \frac{a_4^2}{2} & b_4 & \frac{b_4^2}{2} & a_4 b_4 \\ 1 & a_5 & \frac{a_5^2}{2} & b_5 & \frac{b_5^2}{2} & a_5 b_5 \\ 0 & a & 0 & b & 0 & 0 \end{bmatrix} \begin{pmatrix} u(x,y) \\ u_x(x,y) \\ u_{xx}(x,y) \\ u_y(x,y) \\ u_{yy}(x,y) \\ u_{xy}(x,y) \end{pmatrix} = \begin{pmatrix} c_1 \\ c_2 \\ c_3 \\ c_4 \\ c_5 \\ c_n \end{pmatrix},$$

which we can solve in a similar fashion to the other equations.

Bibliography

[1] Y. Agca, J. Gilmore, M. Byers, E. J. Woods, J. Liu, and J. K. Critser. Osmotic characteristics of mouse spermatozoa in the presence of extenders and sugars. *Biol Reprod*, 67(5):1493–501, Nov 2002.

[2] Y. Agca, J. Liu, E. Critser, and J. Critser. Fundamental cryobiology of rat immature and mature oocytes: hydraulic conductivity in the presence of me(2)so, me(2)so permeability, and their activation energies. *J Exp Zool*, 286(5):523–33, Apr 2000.

[3] Y. Agca, J. Liu, S. Mullen, J. Johnson-Ward, K. Gould, A. Chan, and J. Critser. Chimpanzee (*Pan troglodytes*) spermatozoa osmotic tolerance and cryoprotectant permeability characteristics. *J Androl*, 26(4):470–7, Jan 2005.

[4] E. Amorim, J. Graham, M. Meyers, and B. Spizziri. Delivering cholestanol or desmosterol to bull sperm membranes improves cryosurvival. *Reproduction*, 2008.

[5] D. M. Anderson and M. G. Worster. Weakly nonlinear analysis of convection in mushy layers during the solidification of binary alloys. *Journal of Fluid Mechanics*, 302:307–331, 1995.

[6] G. Arfken and H. Weber. *Mathematical methods for physicists, 6th ed.* Elsevier Academic Press, Burlington, MA, 2005.

[7] W. Armitage and B. Juss. Osmotic response of mammalian cells: Effects of permeating cryoprotectants on nonsolvent volume. *Journal of Cellular Physiology*, Jan 1996.

[8] F. Arnaud, C. Hunt, and D. Pegg. Some effects of propane-1,2-diol on human platelets. *Cryobiology*, 27(2):119–29, Apr 1990.

[9] F. G. Arnaud and D. E. Pegg. Cryopreservation of human platelets with 1.4m glycerol at -196 degrees c. *Thromb Res*, 53(6):585–94, Mar 1989.

[10] F. G. Arnaud and D. E. Pegg. Cryopreservation of human platelets with propane-1,2-diol. *Cryobiology*, 27(2):130–6, Apr 1990.

[11] P. Barry and J. Diamond. Effects of unstirred layers on membrane phenomena. *Physiol Rev*, 64(3):763–872, Jul 1984.

[12] C. K. Benson, J. Benson, and J. Critser. An improved cryopreservation method for a mouse embryonic stem cell line. *Cryobiology*, 56:120–130, 2008.

[13] J. Benson, C. Chicone, and J. Critser. Exact solutions of a two parameter flux model and cryobiological applications. *Cryobiology*, May 2005.

[14] J. Benson, M. Haidekker, C. Benson, and J. Critser. Mercury free operation of the coulter counter multisizer ii sampling stand. *Cryobiology*, 51(3):344–7, Dec 2005.

[15] J. D. Benson, E. J. Woods, E. J. Walters, and J. K. Critser. The cryobiology of spermatozoa. *Submitted to* Human Reproduction Update, *Submitted*.

[16] J. C. Bischof, C. M. Ryan, R. G. Tompkins, M. L. Yarmush, and M. Toner. Ice formation in isolated human hepatocytes and human liver tissue. *ASAIO J*, 43(4):271–8, Jan 1997.

[17] J. M. Blanco, J. A. Long, G. Gee, A. M. Donoghue, and D. E. Wildt. Osmotic tolerance of avian spermatozoa: influence of time, temperature, cryoprotectant and membrane ion pump function on sperm viability. *Cryobiology*, 56(1):8–14, Feb 2008.

[18] V. G. Boltyanskii. Sufficient conditions for optimality and the justification of the dynamic programming method. *SIAM J. Control*, 4:326–361, 1966.

[19] P. Boutron and A. Kaufmann. Stability of the amorphous state in the system water–1,2-propanediol. *Cryobiology*, 16(6):557–68, Dec 1979.

[20] P. Boutron and A. Kaufmann. Stability of the amorphous state in the system water-glycerol-ethylene glycol. *Cryobiology*, 16(1):83–9, Feb 1979.

[21] P. Boutron, A. Kaufmann, and N. V. Dang. Maximum in the stability of the amorphous state in the system water–glycerol–ethanol. *Cryobiology*, 16(4):372–89, Aug 1979. Journal Article United states.

[22] W. E. Boyce and R. C. DiPrima. *Elementary differential equations and boundary value problems*. Wiley, New York, 5th edition, 1992.

[23] C. O. Bwanga. Cryopreservation of boar semen. i: A literature review. *Acta Vet Scand*, 32(4):431–53, Jan 1991.

[24] A. Chaveiro, J. Liu, S. Mullen, H. Woelders, and J. Critser. Determination of bull sperm membrane permeability to water and cryoprotectants using a concentration-dependent self-quenching fluorophore. *Cryobiology*, 48(1):72–80, Feb 2004.

[25] H. Chen, J. Purtteman, S. Heimfeld, A. Folch, and D. Gao. Development of a microfluidic device for determination of cell osmotic behavior and membrane transport properties. *Cryobiology*, 55(3):200–209, Dec 2007.

[26] C. C. Chicone. *Ordinary differential equations with applications*. Texts in applied mathematics ; 34. Springer, New York, 1999.

[27] S. Chuenkhum and Z. Cui. The parameter conversion from the kedem-katchalsky model into the two-parameter model. *CryoLetters*, Jan 2006.

[28] S. Chuenkhum and Z. Cui. The parameter conversion from the kedem-katchalsky model into the two-parameter model. *Cryo Letters*, 27(3):185–99, Jan 2006.

[29] F. Cocks and W. Brower. Phase diagram relationships in cryobiology. *Cryobiology*, 11(4):340–58, Aug 1974.

[30] J. Collins and G. Graves. The economic consequences of multiple gestation pregnancy in assisted conception cycles. *Hum Fertil (Camb)*, 3(4):275–283, 2000.

[31] J. K. Critser, A. R. Huse-Benda, D. V. Aaker, B. W. Arneson, and G. D. Ball. Cryopreservation of human spermatozoa. iii. the effect of cryoprotectants on motility. *Fertil Steril*, 50(2):314–20, Aug 1988.

[32] P. Debenedetti. Supercooled and glassy water. *Journal of Physics Condensed Matter*, 15(45):1669–1726, 2003.

[33] R. Devireddy, D. Raha, and J. Bischof. Measurement of water transport during freezing in cell suspensions using a differential scanning calorimeter. *Cryobiology*, 36(2):124–55, Mar 1998.

[34] J. Du, J. Tao, F. Kleinhans, P. Mazur, and J. Critser. Water volume and osmotic behaviour of mouse spermatozoa determined by electron paramagnetic resonance. *J Reprod Fertil*, Jan 1994.

[35] A. Einstein, R. Fürth, and A. D. Cowper. *Investigations on the theory of the Brownian movement*. Dover, Jan 1956.

[36] J. A. W. Elliott, R. C. Prickett, H. Y. Elmoazzen, K. R. Porter, and L. E. McGann. A multisolute osmotic virial equation for solutions of interest in biology. *Journal of Physical Chemistry B*, 111(7):1775–1785, Jan 2007.

[37] H. Y. Elmoazzen, J. A. W. Elliott, and L. E. McGann. Osmotic transport across cell membranes in nondilute solutions: a new nondilute solute transport equation. *Biophys J*, 96(7):2559–71, Apr 2009.

[38] G. Fahy, B. Wowk, J. Wu, and S. Paynter. Improved vitrification solutions based on the predictability of vitrification solution toxicity. *Cryobiology*, 48(1):22–35, Feb 2004.

[39] A. Finklestein. *Water movement through lipid bilayers, pores, and plasma membranes: Theory and reality*, volume 4. John Wiley and Sons, New York, 1987.

[40] A. S. for Reproductive Medicine. Patient's fact sheet: Cancer and fertility preservation. Technical report, 2003.

[41] A. S. for Reproductive Medicine. Patient's fact sheet: Challenges of parenting multiples. Technical report, 2003.

[42] B. Fuller. Cryoprotectants: the essential antifreezes to protect life in the frozen state. *Cryo Letters*, 25(6):375–88, Nov 2004.

[43] D. Y. Gao, E. Ashworth, P. F. Watson, F. W. Kleinhans, P. Mazur, and J. K. Critser. Hyperosmotic tolerance of human spermatozoa: separate effects of glycerol, sodium chloride, and sucrose on spermolysis. *Biol Reprod*, 49(1):112–23, Jul 1993.

[44] D. Y. Gao and J. K. Critser. Cell-type-specific methods and devices for the low temperature preservation of the cells of an animal species, 2000.

[45] D. Y. Gao, J. Liu, C. Liu, L. E. McGann, P. F. Watson, F. W. Kleinhans, P. Mazur, E. S. Critser, and J. K. Critser. Prevention of osmotic injury to human spermatozoa during addition and removal of glycerol. *Hum Reprod*, 10(5):1109–22, May 1995.

[46] L. Garceau, J. Henderson, L. J. Davis, S. Petrou, L. R. Henderson, E. McVeigh, D. H. Barlow, and L. L. Davidson. Economic implications of assisted reproductive techniques: a systematic review. *Hum Reprod*, 17(12):3090–109, 2002.

[47] F. Gayle, F. H. Cocks, and M. L. Shepard. The h20-nacl-sucrose phase diagram and applications in cryobiology. *Journal of Applied Chemistry and Biotechnology*, 27:599–607, Feb 1977.

[48] J. Gilmore, J. Du, J. Tao, A. Peter, and J. Critser. Osmotic properties of boar spermatozoa and their relevance to cryopreservation. *J Reprod Fertil*, 107(1):87–95, May 1996.

[49] J. Gilmore, J. Liu, D. Gao, and J. Critser. Determination of optimal cryoprotectants and procedures for their addition and removal from human spermatozoa. *Human Reproduction*, Jan 1997.

[50] J. Gilmore, J. Liu, A. Peter, and J. Critser. Determination of plasma membrane characteristics of boar spermatozoa and their relevance to cryopreservation. *Biol Reprod*, 58(1):28–36, Jan 1998.

[51] H. Guthrie, J. Liu, and J. Critser. Osmotic tolerance limits and effects of cryoprotectants on motility of bovine spermatozoa. *Biol Reprod*, 67(6):1811–6, Dec 2002.

[52] X. Han, L. Ma, J. Benson, A. Brown, and J. K. Critser. Measurement of the apparent diffusivity of ethylene glycol in mouse ovaries through rapid mri and theoretical investigation of cryoprotectant perfusion procedures. *Cryobiology*, 58(3):298–302, Jun 2009.

[53] P. Henrici. *Applied and computational complex analysis*, volume 1. Wiley, New York, 1974.

[54] J. Hernandez. Stability properties of elementary dynamic models of membrane transport. *Bulletin of Mathematical Biology*, 65(1):175–197, Jan 2003.

[55] J. A. Hernández. A general model for the dynamics of the cell volume. *Bulletin of Mathematical Biology*, 69(5):1631–1648, Jun 2007.

[56] C. J. Hunt, S. E. Armitage, and D. E. Pegg. Cryopreservation of umbilical cord blood: 2. tolerance of cd34(+) cells to multimolar dimethyl sulphoxide and the effect of cooling rate on recovery after freezing and thawing. *Cryobiology*, 46(1):76–87, 2003.

[57] M. Jacobs. The simultaneous measurement of cell permeability to water and to dissolved substances. *Journal of Cellular and Comparative Physiology*, 2:427–444, 1932.

[58] F. Jahnel. Über die widerstandsfähigkeit von menschlichen spermatozoen gegennumber starker k: lte. *Journal of Molecular Medicine*, 17(37):88–89, Jan 1938.

[59] J. Karlsson, E. Cravalho, and M. Toner. Intracellular ice formation: Causes and consequences. *Cryo Letters*, 14:323–336, 1993.

[60] J. O. Karlsson and M. Toner. Long-term storage of tissues by cryopreservation: critical issues. *Biomaterials*, 17(3):243–56, Feb 1996.

[61] A. M. Karow and J. K. Critser. *Reproductive tissue banking : scientific principles*. Academic Press, San Diego, 1997.

[62] I. Katkov. A two-parameter model of cell membrane permeability for multisolute systems. *Cryobiology*, 40(1):64–83, Feb 2000.

[63] I. Katkov. The point of maximum cell water volume excursion in case of presence of an impermeable solute. *Cryobiology*, 44(3):193–203, 2002.

[64] O. Kedem and A. Katchalsky. Thermodynamic analysis of the permeability of biological membranes to non-electrolytes. *Biochim Biophys Acta*, 27(2):229–46, 1958.

[65] F. Kleinhans and P. Mazur. Comparison of actual vs. synthesized ternary phase diagrams for solutes of cryobiological interest. *Cryobiology*, 54(2):212–222, Apr 2007.

[66] F. W. Kleinhans. Membrane permeability modeling: Kedem-katchalsky vs a two-parameter formalism. *Cryobiology*, 37(4):271–89, 1998.

[67] L. L. Kuleshova and A. Lopata. Vitrification can be more favorable than slow cooling. *Fertil Steril*, 78(3):449–54, 2002.

[68] M. Lane, W. Schoolcraft, and D. Gardner. Vitrification of mouse and human blastocysts using a novel cryoloop container-less technique. *Fertil Steril*, 72(6):1073–8, Dec 1999.

[69] H. E. Layton. Mathematical models of the mammalian urine concentrating mechanism. In H. E. Layton and A. M. Weinstein, editors, *Membrane transport and renal physiology, the IMA volumes in mathematics and its applications*, volume 129, pages 232–272. Springer, New York, 2002.

[70] U. Ledzewicz and H. Schättler. Optimal controls for a model with pharmacokinetics maximizing bone marrow in cancer chemotherapy. *Mathematical Biosciences*, 206(2):320–42, Apr 2007.

[71] E. Lee and L. Markus. *Foundations of Optimal Control Theory*. The SIAM Series in Applied Mathematics. John Wiley and Sons, New York, 1968.

[72] R. Levin and T. Miller. An optimum method for the introduction or removal of permeable cryoprotectants: isolated cells. *Cryobiology*, 18(1):32–48, Jan 1981.

[73] R. L. Levin. A generalized method for the minimization of cellular osmotic stresses and strains during the introduction and removal of permeable cryoprotectants. *Journal of biomechanical engineering*, 104(2):81–6, May 1982.

[74] S. Levin, R. Levin, A. Solomon, A. Pandiscio, and D. Kirkwood. Improved stop-flow apparatus to measure permeability of human red cells and ghosts. *J Biochem Biophys Methods*, 3(5):255–72, Nov 1980.

[75] J. Liu, J. Christian, and J. Critser. Canine rbc osmotic tolerance and membrane permeability. *Cryobiology*, 44(3):258–68, Jun 2002.

[76] J. Liu, D. Gao, L. He, L. Moey, K. Hua, and Z. Liu. The phase diagram for the ternary system propylene glycol-sodium chloride-water and their application to platelet cryopreservation. *Zhongguo Shi Yan Xue Ye Xue Za Zhi*, 11(1):92–5, Feb 2003.

[77] J. Liu, E. Woods, Y. Agca, E. Critser, and J. Critser. Cryobiology of rat embryos ii: A theoretical model for the development of interrupted slow freezing procedures. *Biol Reprod*, 63(5):1303–12, Nov 2000. 0006-3363 Journal Article.

[78] Z. Liu. Personal communication, 2004.

[79] J. Lovelock. The haemolysis of human red blood-cells by freezing and thawing. *Biochim Biophys Acta*, 10(3):414–26, Mar 1953. 0006-3002 Journal Article.

[80] J. Lovelock. The mechanism of the protective action of glycerol against haemolysis by freezing and thawing. *Biochim Biophys Acta*, 11(1):28–36, May 1953.

[81] B. Luyet and E. Hodapp. Revival of frog's spermatozoa vitrified in liquid air. *Proceedings of the Society for Experimental Biology and Medicine*, 39:433–434, Apr 1938.

[82] B. Luyet and G. Rapatz. A review of basic researches on the cryopreservation of red blood cells. *Cryobiology*, 6(5):425–82, 1970.

[83] B. J. Luyet and M. P. Gehenio. *Life and death at low temperatures*. Biodynamica, Normandy, Mo.,, 1940.

[84] M. Marcus and H. Minc. *A survey of matrix theory and matrix inequalities*. Dover Publications Inc., New York, 1992. Reprint of the 1969 edition.

[85] P. Mazur. Kinetics of water loss from cells at subzero temperatures and the likelihood of intracellular freezing. *J Gen Physiol*, 47:347–69, Nov 1963.

[86] P. Mazur, S. Leibo, and E. Chu. A two-factor hypothesis of freezing injury. evidence from chinese hamster tissue-culture cells. *Exp Cell Res*, 71(2):345–55, 1972.

[87] P. Mazur and R. Miller. Permeability of the human erythrocyte to glycerol in 1 and 2 m solutions at 0 or 20 degrees c. *Cryobiology*, 13(5):507–22, Oct 1976.

[88] J. McGrath. Coupled transport of water and cryoprotective agents across the murine oocyte plasma membrane. *Ninth National Heat Transfer Conference*, 1992.

[89] H. Meryman. Mechanics of freezing in living cells and tissues. *Science*, 124(3221):515–21, Sep 1956.

[90] H. Meryman. Modified model for the mechanism of freezing injury in erythrocytes. *Nature*, 218(139):333–6, Apr 1968.

[91] H. T. Meryman. Modified model for the mechanism of freezing injury in erythrocytes. *Nature*, 218(139):333–6, 1968.

[92] H. T. Meryman and M. S. Douglas. Isotonicity in the presence of penetrating cryoprotectants. *Cryobiology*, l9(5):565–9, Oct 1982.

[93] S. A. Meyers. Spermatozoal response to osmotic stress. *Animal Reproduction Science*, 89(1-4):57–64, Oct 2005.

[94] R. R. Mohler. *Bilinear Control Processes with Applications to Engineering, Ecology, and Medicine*. Mathematics in Science and Engineering. Academic Press, New York, 1973.

[95] W. J. Moore. *Physical chemistry.* Prentice-Hall chemistry series. Prentice-Hall, Englewood Cliffs, N.J.„ 3d edition, 1962.

[96] G. Morris, E. Acton, and S. Avery. A novel approach to sperm cryopreservation. *Hum Reprod*, 14(4):1013–21, Apr 1999.

[97] K. Muldrew, J. P. Acker, J. A. Elliott, and L. E. McGann. The water to ice transition: Implications for living cells. In B. Fuller, N. Lane, and E. Benson, editors, *Life in the Frozen State.* CRC Press, New York, 2004.

[98] S. F. Mullen, M. Li, Y. Li, Z. J. Chen, and J. K. Critser. Human oocyte vitrification: the permeability of metaphase ii oocytes to water and ethylene glycol and the appliance toward vitrification. *Fertil Steril*, 89(6):1812–25, 2008.

[99] L. O'Neil, S. J. Paynter, B. J. Fuller, R. W. Shaw, and A. L. DeVries. Vitrification of mature mouse oocytes in a 6 m me2so solution supplemented with antifreeze glycoproteins: the effect of temperature. *Cryobiology*, 37(1):59–66, 1998.

[100] T. Papanek. *The water permeability of the human erythrocyte in the temperature range +25° C to -10° C.* PhD thesis, Massachusetts Institute of Technology, 1978. by Thomas H. Papanek. ill. ; 28 cm. Vita.

[101] A. Parkes. Preservation of spermatozoa at low temperatures. *British Medical Journal*, 2(4415):212–213, Jan 1945.

[102] S. J. Paynter, L. O'Neil, B. J. Fuller, and R. W. Shaw. Membrane permeability of human oocytes in the presence of the cryoprotectant propane-1,2-diol. *Fertility and Sterility*, 75(3):532–8, Mar 2001.

[103] D. E. Pegg. The history and principles of cryopreservation. *Semin Reprod Med*, 20(1):5–13, 2002.

[104] D. E. Pegg. The role of vitrification techniques of cryopreservation in reproductive medicine. *Human fertility (Cambridge, England)*, 8(4):231–9, Dec 2005.

[105] D. E. Pegg. Principles of cryopreservation. *Methods Mol Biol*, 368:39–57, Jan 2007.

[106] D. E. Pegg and M. P. Diaper. On the mechanism of injury to slowly frozen erythrocytes. *Biophys J*, 54(3):471–88, Sep 1988.

[107] D. E. Pegg, B. Rubinsky, M. P. Diaper, and C. Y. Lee. Analysis of the introduction and removal of glycerol in rabbit kidneys using a krogh cylinder model. *Cryobiology*, 23(2):150–60, Apr 1986.

[108] R. Pfaff, J. Liu, D. Gao, A. Peter, T. Li, and J. Critser. Water and dmso membrane permeability characteristics of in-vivo- and in-vitro-derived and cultured murine oocytes and embryos. *Mol Hum Reprod*, 4(1):51–9, Jan 1998. 1360-9947 Journal Article.

[109] M. Phelps, J. Liu, J. Benson, C. Willoughby, J. Gilmore, and J. Critser. Effects of percoll separation, cryoprotective agents, and temperature on plasma mem-

brane permeability characteristics of murine spermatozoa and their relevance to cryopreservation. *Biol Reprod*, 61(4):1031–1041, Jan 1999.

[110] C. Polge, A. Smith, and A. Parkes. Revival of spermatozoa after vitrification and dehydration. *Nature (London)*, 164:666, 1949.

[111] L. S. Pontryagin, V. G. Boltyanskii, R. V. Gamkrelidze, and E. F. Mishchenko. *The mathematical theory of optimal processes*. Interscience Publishers, Inc, New York, 1962.

[112] M. Ramezani, M. R. Valojerdi, and K. Parivar. Effect of three vitrification methods on development of two-cell mouse embryos. *Cryo Letters*, 26(2):85–92, Jan 2005.

[113] C. Shaffner, E. Henderson, and C. Card. Viability of spermatozoa of the chicken under various environmental conditions. *Poultry Science*, 20:259–265, 1941.

[114] E. Shalaev and F. Franks. Equilibrium phase-diagram of the water-sucrose-nacl system. *Thermochimica Acta*, 255:49–61, May 1995.

[115] M. Shepard, C. Goldston, and F. Cocks. The h2o-nacl-glycerol phase diagram and its application in cryobiology. *Cryobiology*, 13(1):9–23, Feb 1976.

[116] J. K. Sherman. Low temperature research on spermatozoa and eggs. *Cryobiology*, 1(2):103–29, Jan 1964.

[117] L. Shettles. The respiration of human spermatozoa and their response to various gases and low temperatures. *American Journal of Physiology*, Jan 1939.

[118] W. Si, J. Benson, H. Men, and J. Critser. Osmotic tolerance limits and effects of cryoprotectants on the motility, plasma membrane integrity and acrosomal integrity of rat sperm. *Cryobiology*, 53(3):336–48, Dec 2006.

[119] A. K. Solomon. Water channels across the red blood cell and other biological membranes. *Methods Enzymol*, 173:192–222, 1989.

[120] N. Songsasen, I. Yu, S. Murton, D. L. Paccamonti, B. E. Eilts, R. A. Godke, and S. P. Leibo. Osmotic sensitivity of canine spermatozoa. *Cryobiology*, 44(1):79–90, Feb 2002.

[121] W. D. Stein and W. R. Lieb. *Transport and diffusion across cell membranes*. Academic Press, Orlando, 1986.

[122] J. M. Tarbell. Mass transport in arteries and the localization of atherosclerosis. *Annual Review of Biomedical Engineering*, 5:79–118, 2003.

[123] T. Terwilliger and A. Solomon. Osmotic water permeability of human red cells. *J Gen Physiol*, 77(5):549–70, May 1981.

[124] M. Toner, E. Cravalho, and M. Karel. Cellular response of mouse oocytes to freezing stress: prediction of intracellular ice formation. *J Biomech Eng*, 115(2):169–74, May 1993.

[125] E. J. Walters, J. D. Benson, E. J. Woods, and J. K. Critser. The history of sperm cryopreservation. In A. A. Pacey and M. J. Tomlinson, editors, *Sperm Banking: Theory and Practice*, page 128. Cambridge University Press, Cambridge, 2009.

[126] E. M. Walters, H. Men, Y. Agca, S. F. Mullen, E. S. Critser, and J. K. Critser. Osmotic tolerance of mouse spermatozoa from various genetic backgrounds: acrosome integrity, membrane integrity, and maintenance of motility. *Cryobiology*, 50(2):193–205, Apr 2005.

[127] C. X. Wang, L. Wang, and C. R. Thomas. Modelling the mechanical properties of single suspension-cultured tomato cells. *Annals of Botany*, 93(4):443–453, 2004.

[128] C. E. Willoughby, P. Mazur, A. T. Peter, and J. K. Critser. Osmotic tolerance limits and properties of murine spermatozoa. *Biol Reprod*, 55(3):715–27, Sep 1996.

[129] H. Woelders and A. Chaveiro. Theoretical prediction of 'optimal' freezing programmes. *Cryobiology*, 49(3):258–71, Dec 2004.

[130] E. Woods, J. Benson, Y. Agca, and J. Critser. Fundamental cryobiology of reproductive cells and tissues. *Cryobiology*, 48(2):146–56, Apr 2004.

[131] E. Woods, M. Byers, J. Liu, and J. Critser. Effects of seeding on murine spermatozoa cryopreservation. *Cryobiology*, 41:324–393, 2000.

[132] E. J. Woods, J. Liu, C. W. Derrow, F. O. Smith, D. A. Williams, and J. K. Critser. Osmometric and permeability characteristics of human placental/umbilical cord blood cd34+ cells and their application to cryopreservation. *J Hematother Stem Cell Res*, 9(2):161–73, 2000.

[133] E. J. Woods, J. Liu, M. A. Zieger, J. R. Lakey, and J. K. Critser. Water and cryoprotectant permeability characteristics of isolated human and canine pancreatic islets. *Cell Transplantation*, 8(5):549–59, 1999.

[134] M. Wusteman, D. Pegg, M. Robinson, L. Wang, and P. Fitch. Vitrification media: toxicity, permeability, and dielectric properties. *Cryobiology*, 44(1):24–37, Feb 2002.

[135] S. Yavin and A. Arav. Measurement of essential physical properties of vitrification solutions. *Theriogenology*, 67(1):81–9, Jan 2007.

[136] S. Z. Zhang and G. M. Chen. Analytical solution for the extremums of cell water volume and cell volume using a two-parameter model. *Cryobiology*, 44(3):204–9, 2002.

VITA

James Benson is the youngest of four siblings, and was born in Indianapolis at the intersection of the "MTV," "X" and "Y" generations. James grew up deeply interested in everything. In fact, in another life, or with slightly different winds of fortune, it would not be a great surprise if James ended up in a field other than mathematics such as music, law, or journalism.

Music has played an enormous role in James's life. Piano lessons began at age 6, and in earnest at age 12. Classical piano was appealing, but required too much time for a boy who was interested in everything. On the other hand, at 14, James was introduced to jazz piano, along with the freedom to create music without much rehearsal.

James was introduced to one of his future Ph. D. advisors also at the age of 14 while assisting his brother, Chuck, in data analysis. Chuck Benson did his Ph. D. under John Critser on the Cryobiology of Hamster Pancreatic Islets. Because of James's initial foray into data analysis and some wet-lab work, he was asked back as a summer student the following several summers. This led to an early indoctrination into the details and challenges of fundamental and reproductive cryobiology.

After high school, James attended Purdue University, ostensibly to obtain a degree in Bio-Engineering, then a reasonably new field there. For administrative reasons, this degree was supplanted by traditional Electrical Engineering, of which James became disinterested. The decision to pursue Mathematics was made during the beginning of his third year at Purdue, when he became disenchanted with the prospects as an

engineer, and saw that mastery of the mathematical machinery behind engineering was the key to the applied sciences. To keep a grounding in the humanities, James concurrently pursued a bachelor's degree in English. As of this writing, he is 6 credit hours shy of completing this B.A. He has promised his parents that this degree will be completed.

This interest and passion for knowledge in a vast array of fields along with his involvement in the truly interdisciplinary field, Cryobiology, played a role in his academic philosophy that the departmentalization of the University has slowed the growth of development. This philosophy seems to be in the early stages of recognition by universities and granting institutions around the country as inter- and multidisciplinary groups are being formed, often to tackle problems in the life sciences.

James met his wife, Corinna, through this interdisciplinary pursuit: Corinna is a veterinarian and came to the University of Missouri for a fellowship in Comparative medicine. Through a series of events, Corinna ended up working with John Critser as her Ph. D. advisor as well, and James her main research collaborator. They have a two-and-a-half year old son, Jonathan William, and another child is due in December.

James has accepted a two year National Research Council Postdoctoral Research Assistantship at the National Institute for Standards and Technology (NIST) in Gaithersburg, MD and will begin in September.